Constraints on emplacement and timing of the Steen River impact structure, Alberta, Canada

by

Ebberly Ann MacLagan

A thesis submitted in partial fulfillment of the requirements for the degree of

Master of Science

Department of Earth and Atmospheric Sciences
University of Alberta

ABSTRACT

The Steen River impact structure (SRIS) is a buried, complex crater located in NW Alberta, Canada. It was discovered in the mid 1900's and was initially thought to be an endogenic igneous intrusion. With the growth of impact studies on Earth and other planets, the SRIS was recognized as such in the 1960's. Since then, numerous exploratory wells have been drilled in and around the structure to assess its economic potential. While many of these wells are proprietary, three cores collected in 2000 are available for research and have been the focus of the most recent SRIS studies. A ubiquitous product of impact events is impact breccia, which may contain clasts of target material and melt. At the well-studied Ries impact structure in Germany, this breccia is classified as suevite. The impact breccia observed at the SRIS is similar to the Ries suevite; however, the term "suevite" has been applied to many impact structures and its formation mechanism is still debated. In previous studies, three cores from the SRIS (ST001, ST002, and ST003) were logged by hand and characterized in detail using thin sections; however, a representative, yet detailed, mineralogical overview of the core was lacking. In this thesis, hyperspectral imaging was used to quickly scan the three cores and make detailed mineralogical maps of each. Results highlight hydrothermal and ammoniated minerals in the SRIS impact breccia, and aid in refining the emplacement model for the suevite-like breccia. The only published age of the crater is poorly constrained and conflicts with the stratigraphy overlying the crater. To better constrain the SRIS age, zircons were extracted from the core samples and characterized using secondary ion mass spectrometry. Zircons are commonly used for U-Pb geochronology because they can withstand most geological disturbances and may incorporate radiogenic isotopes into their crystal structure. By analyzing both granite- and melt-derived zircons, this study aimed to constrain the age of the SRIS impact event and compare it to the known age of the Proterozoic basement rocks.

PREFACE

This thesis was led and written by myself, Ebberly MacLagan. My supervisors, Dr. Christopher Herd and Dr. Erin Walton, were involved with the development and progress of each of the two main projects.

Chapter 2, on the hyperspectral imaging of drill core, is being edited for submission in GSA Bulletin. In this project, E. MacLagan scanned the core with the assistance of Jilu Feng and Benoit Rivard. Data processing and mapping was carried out by E. MacLagan. Drs. Erin Walton, Christopher Herd, and Benoit Rivard assisted with data interpretation and conception of the final model.

Chapter 3, on geochronology of zircons, was primarily coordinated by E. MacLagan. Dr. Daniel Layton-Matthews at Queen's University operated the SelFrag instrument, Dr. Andy DuFrane and Serhiy Buryak did the heavy liquids separation. E. MacLagan performed the initial SEM imaging, along with the sieving and magnetic separation. Dr. Richard Stern assisted with additional SEM analyses, including all cathodoluminescence imaging, as well as grain selection. Both Dr. Stern and Robert Dokken assisted with mount preparation and polishing. Bill Davis at the Geological Survey of Canada ran the SIMS analyses.

ACKNOWLEDGEMENTS

There are many people who have been involved with this thesis project and I am grateful to each and every one. Most importantly, I wish to express my sincere gratitude to my supervisors, Chris and Erin, for your patience and support through my undergraduate project, and now with this MSc thesis. When you handed me the first piece of Steen breccia, it was the most baffling rock I had ever seen, but because of that, I have a whole new perspective and appreciation for the science and I am truly grateful for it. Go Steen!

I also would like to extend a big thank you to Richard Stern for the hours spent down in CCIM trying to figure out the zircon story; I couldn't have done this venture without your help and knowledge. Thank you for sticking with the project, even when we thought it might not work out. An additional thank you goes to Benoit Rivard – your remote sensing class alone got me well on the way to understanding spectroscopy, and thanks for helping me tease out the spectra and teaching me how to use ENVI. Another thank you goes to Mike Dence for sitting down with me and helping me model the emplacement of Steen; your patience and comments on my impact melt project were invaluable. Thank you also to Larry Heaman for being a part of my defence committee, and for your insights on the geochronology of Steen River.

I also extend my utmost thanks to those who helped with instrumentation and analyses: Thank you to Andy DuFrane and Serhiy Buryak for helping with the zircon separation process; thanks to Dan Layton-Matthews at Queen's for running my samples on SelFrag, especially during such a tough time; thank you to Robert Dokken for helping with mounting the zircons and patiently showing me how to hand-pick the grains; thanks to Jilu Feng for scanning all 199 boxes of core with me, and for answering all my ENVI questions; thank you to Rob Natyshen at MCRF for arranging transport and facilitating the loading/unloading of all the core, that was a huge help; thanks to Mark Labbe for teaching me how to use various pieces of equipment and tools, both for

TABLE OF CONTENTS

LIST OF TABLES

LIST OF FIGURES

CHAPTER 1:
INTRODUCTION

1.1 INTRODUCTION TO IMPACT EVENTS

Since the formation of our solar system and the accretion of the first rocky bodies, hypervelocity impacts have been, and continue to be, a prevalent force in shaping the planets and other rocky or icy bodies. A hypervelocity impact occurs when two solid masses collide with velocities greater than 5 km/s, resulting in the production of a shock wave that propagates through both masses at supersonic speeds. On Earth, a hypervelocity impact generally occurs at a velocity >11 km/s, at which the projectile can pass through the atmosphere without decelerating (French, 1998). The sudden contact between the two objects generates extremely high temperatures and pressures and results in a unique type of metamorphism known as "shock metamorphism". Metamorphism is the solid-state transformation and deformation of rocks when exposed to high temperatures and pressures; this process typically occurs over long time-scales (millions of years) in convergent plate margins or during burial to great depths in the Earth's crust. In contrast, shock metamorphism is nearly instantaneous and results in the transformation of rocks due to shock compression (Bischoff and Stöffler, 1992). It produces high temperature polymorphs of minerals, such as coesite from quartz, and may result in melting the target material.

Impact cratering has affected nearly all aspects of Earth's systems, including the atmosphere, geosphere, and biosphere, and has been prevalent throughout most of our solar system's history (Osinski, 2006). Indeed, one of the biggest known, and likely most important impact events in Earth's history, was the moon-forming impact around 4.5 Ga (Cameron and Ward, 1976). The "standard model" of moon formation is that a Mars-sized planetesimal, called Theia, hit the Earth at an oblique angle, and the debris that was ejected into space eventually amalgamated to form the body of the moon, with the majority of the moon comprised of Theia's remains (e.g. Asphaug, 2014). Although the basis of this model is generally accepted in the scientific community, the topic is still under debate and modification. Isotopic evidence suggests that there is significant compositional disparity between the Moon and Earth (e.g. Wang and Jacobsen, 2016; Kruijer and Kleine, 2017), yet many isotopic ratios are similar on these two bodies (e.g. Young et al., 2016; Mougel et al., 2018) implying that the impact event induced considerable mixing of material from both bodies.

Another important impact event, recognized by a peak in the number of craters on the Moon around 3.9 billion years ago, has been classified as The Late Heavy Bombardment (LHB) (Wetherill, 1975). The LHB may have been caused by planetary migration, particularly Saturn and Jupiter (Gomes et al., 2005), that disrupted the orbits of smaller bodies in the main asteroid belt and caused them to collide with planets in the inner solar system, resulting in an anomalously high impact cratering rate.

Craters can provide information on the surface ages of other planets – highly-cratered regions have been exposed for a longer period and therefore have experienced more cratering than younger areas with fewer impacts. On planets without tectonic activity or erosion, impact structures may create slopes and outcrops that otherwise would not exist. As such, crater walls can be studied with remote sensing and/or rovers to examine the planetary subsurface. On Earth, a sampling bias exists in the known crater record due to subduction and erosion of oceanic crust and difficulty in exploring the ocean floor. As a result, nearly all known craters on Earth are located on continental crust (Fig. 1.1). These structures may host economically-viable mineral, oil, and/or gas deposits, either directly associated with the impact event, or post-dating the impact but trapped in the unique structural conditions of the crater (Reimold et al., 2005).
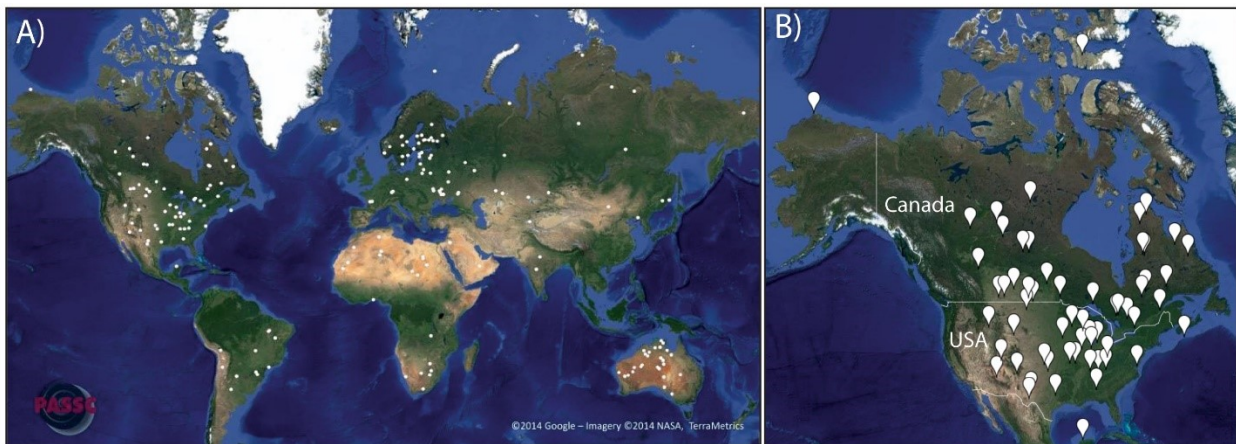
Figure 1. 1. Locations of impact structures on Earth. A) Global map of impact locations. B) Map of impact structures in North America; white pins show locations of confirmed impact structures. From the Earth Impact Database (Spray, 2018).

1.1.1 CRATER MORPHOLOGIES

Impact events have been studied for decades; research on Earth impacts escalated after the proposal that Meteor Crater (a.k.a. Barringer Crater), Arizona, was formed by a meteorite impact

(Barringer, 1905). The structures resulting from hypervelocity impact events on Earth can be divided into two groups, simple craters and complex craters, based on the lack or presence of a central uplift, respectively (Dence, 1973). Simple craters are bowl shaped with a raised rim surrounding the main crater cavity. On Earth, simple craters have a diameter (D) <4 km in crystalline targets, while complex craters are >4 km. Complex structures contain a central uplift, and generally contain radial faults and/or terraces due to post-impact collapse (Dence, 1973). In sedimentary targets, the transition from simple to complex occurs at 1-2 km diameter (Grieve et al., 1981). Even larger complex craters (D>25 km) may be classified as peak-ring structures (e.g. Chicxulub; Morgan et al., 2000) if they contain a raised ring inside the crater instead of a central uplift. The largest classification of a complex crater is a multi-ring basin, which has multiple raised rings between the center and outermost rim (Grieve et al., 1981). Multi-ring basins are not observed on Earth due to erosion, but the largest craters, Sudbury and Vredefort, may have contained multiple rings at one time (Deutsch et al., 1995; Therriault et al., 1997). Large, multi-ring craters are more commonly observed on the Moon and other planetary bodies.

The structural definitions of simple vs complex craters are the same on other rocky bodies; however, due to differences in target material integrity / composition and gravitational forces, the transition diameter varies. For example, on Mars the transition from simple to complex craters occurs between approximately 6 and 11 km diameter (Robbins and Hynek, 2012). For the moon, a body with significantly lower surface gravity, this transition occurs around D=19 km (Pike, 1980). One well-known example of a simple crater on Earth is the Barringer or Meteor Crater in Arizona, USA. Its ~1.2 km diameter, simple bowl shape, and raised rim are characteristic of a simple crater structure. Complex craters can be much larger and are characterized by a central uplift feature and faulting around the crater rim. Some of the largest well-known complex craters are the Sudbury impact structure in Ontario, Canada; the Vredefort dome in South Africa; and the Chicxulub structure in Mexico. The latter is associated with a global iridium anomaly and a massive extinction event around 65 Ma that ended the reign of non-avian dinosaurs (e.g. Brusatte et al., 2015; and references therein).

1.1.2 STAGES OF EMPLACEMENT

The emplacement mechanism of impact structures is well defined and can be summarized in three main stages (i.e. French, 1998; and references therein). An impact event begins with the

contact and compression stage, during which the impactor strikes the target and causes a shockwave to propagate down and out into the target material. A rarefaction wave travels in the opposite direction, back through the impactor, reflects off the outermost side, and rebounds to follow the shockwave into the target. This results in melting and vaporization of the impactor, marking the end of the first stage. In the second stage, the shock and rarefaction waves propagate through the target material and result in ejection of material at the free surface – the contact between target rocks and empty space above. This stage is known as the excavation stage, and together with stage one, they last a fraction of a second (Fig. 1.2A). The third and final main stage consists of crater modification. In complex craters, the central uplift rebounds and material slumps off the sides of the raised peak, resulting in extensive mixing. Due to pressure release after the shockwave passes, the sides of the crater also slump inwards, resulting in a smaller depth to diameter ratio than in simple craters. This effect is less pronounced on bodies with lower gravity, such as the Moon, where craters with the same diameter as on Earth will be deeper due to less gravitational influence on slumping and infilling (Pike, 1980).

Once material has settled and movement has ceased, the modification stage may be complete; however, this stage may also last hundreds to thousands of years after the impact event, depending on the size of the crater and its geographic location. Residual heat from the impact event can generate hydrothermal systems (Kirsimäe and Osinski, 2012), which will further modify and alter the original mineralogy. At the Chicxulub structure, slow cooling due to prolonged release of volatiles from sedimentary rocks may have lasted up to 20,000 years after impact (Deutsch and Langenhorst, 2007). Tectonism can also extensively modify the impact structure, as observed at the Sudbury structure (Spray et al., 2004).

1.1.3 CHARACTERISTICS OF IMPACT STRUCTURES

The pressures induced by hypervelocity impacts range from near-crustal pressures (~0 GPa), to around 80 GPa (Fig. 1.2B); this range has been divided into a series of stages depending on the shock effects observed in minerals (Singleton et al., 2011; Stöffler, 1971). The low shock stages (0-2) in the classification of Singleton et al. (2011), an updated and more detailed version of the scheme from Stöffler (1971), are characterized by fracturing and deformation of the minerals present. Intermediate stages (3-4) in this classification include the formation of high-pressure polymorphs and planar deformation features (PDFs). PDFs are straight, closely-spaced,

amorphous lamellae with specific crystallographic orientations (Stöffler and Grieve, 2007; Ferrière and Osinski, 2013) that can form in quartz and feldspar grains as a result of shock metamorphism and indicate pressures from ~5-35 GPa (Stöffler and Langenhorst, 1994). However, it has recently been noted that PDFs may form from lightning strikes as well (Melosh, 2017), so they are not singularly indicative of an impact event. Shock stages 5-6 are characterized by the appearance of partial melting and diaplectic glass, formed though intense pressure and shearing. Diaplectic glass does not form through melting, as volcanic glass does, but is a solid-state transformation to an amorphous structure (Ferrière and Osinski, 2013). The final stages (7-8) consist of complete melting or even vaporization of the rocks (Singleton et al., 2011).
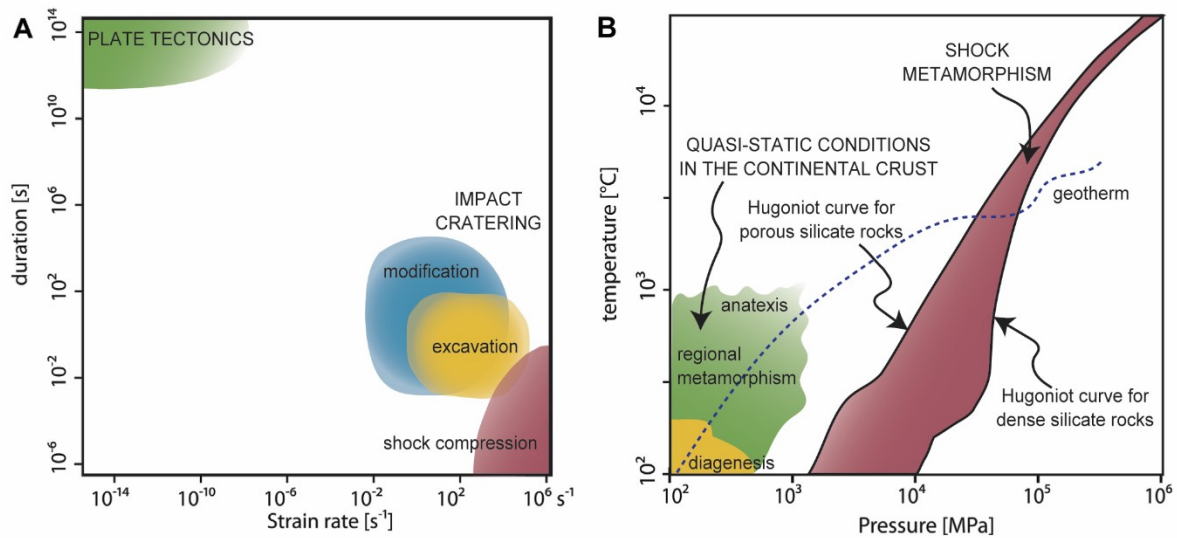
Figure 1. 2. Typical pressure and temperature regimes for crustal and hypervelocity environments. A) Duration and strain rates for typical tectonic and shock metamorphic environments. B) A temperature-pressure diagram comparing P-T conditions of crustal metamorphism with shock metamorphism. Modified from Kenkmann et al. (2014).

To confirm that a structure is caused by a hypervelocity impact, it must be differentiated from traditional volcanogenic, or endogenic igneous processes. The extremely high temperatures and pressures caused by hypervelocity impacts are distinct from traditional metamorphism (Fig. 1.2; Kenkmann et al., 2014). Some of the microscopic features described above are unique to shock-metamorphic environments. Combined with the presence of high-pressure polymorphs, microscale deformation, and melting or glass, these features can aid in confirming an impact structure. Shatter cones are the only macroscopic feature that is definitively impact induced. These conical, radiating features form at pressures >10 GPa and, in some cases, may be used to locate the origin of the shock waves (French, 1998; and references therein).

1.1.4 THE STEEN RIVER IMPACT STRUCTURE

Within Canada, there are more than 30 confirmed impact structures (Fig. 1.1), and at least three are in the province of Alberta. The largest of these, and the most well studied to date, is the Steen River impact structure (SRIS). The SRIS is located in northwestern Alberta (59º 31' N, 117º 38' W), around 700 km NW of the capital city, Edmonton. It is named after the nearby hamlet of Steen River which is 30 km NE of the structure (Molak et al., 2001). This part of Alberta is situated in the Western Canada Sedimentary Basin (WCSB), which is known for its oil and gas plays; indeed, the Steen River area is proximal to the Zama oil field, discovered in 1966 in the Keg River Formation (Meijer Drees, 1994). The Keg River Formation itself underlies the SRIS (Fig. 1.3).

1.1.4.1 DISCOVERY AND DRILLING

The SRIS was discovered shortly before the Zama field, during an iron prospecting project by Imperial Oil Enterprises Ltd. (Underhill, 1964). Noisy seismic data, shallow basement rocks, and the presence of a "volcanic unit" in well IOE Steen River 12-19 led to the interpretation of an unusual igneous intrusion in the area. Carrigy and Short (1968) performed a detailed petrographical study of the rocks from well 12-19 and found that mineral features in the SRIS resembled those in rocks affected by a nuclear explosion. These shock effects, combined with additional well data that penetrated steeply dipping Devonian strata – in an area where they are otherwise horizontal – led to its classification as an impact structure (Carrigy and Short, 1968). However, this interpretation still invoked an impact-triggered intrusive volcanic event to explain the so-called pitchstone and high temperatures observed in the base of the wells. In 1972, Stephen Winzer carried out an intensive study of the shock features (PDFs, glasses, maskelynite) in the SRIS minerals and concluded that the structure must have been formed by an impact event (Winzer, 1972). This was followed by many more prospects in the area, searching for economic mineral deposits as well as hydrocarbons (Robertson, 1997; McCleary, 1997; Wilson et al., 1989; Germundson and Fischer, 1978; Brown, 1994; Bird Geophysical, 1999).

In late 2000, New Claymore Resources initiated a drilling program at the SRIS based on the previous work done at the structure and the presence of kimberlites 300 km SSE of the SRIS (Okulitch, 2006). The resulting three cores, ST001, ST002, and ST003, are housed at the Mineral Core Research Facility (MCRF) in Edmonton, Alberta, and have been used in a series of detailed studies on the SRIS. In total, these three cores contain >1 km of continuous rock and each penetrate

part of the SRIS; ST003 penetrates ~11 m into the central uplift and contains ~167 m of impact breccia, while cores ST001 and ST002 are in the annular trough and contain ~115 and ~30 m of impact breccia, respectively (Fig. 1.3).

1.1.4.2 PREVIOUS STUDIES

Walton et al. (2016) analyzed high pressure minerals (e.g. garnets) associated with shock veins in SRIS core ST003, which penetrated the side of the central uplift. These assemblages constrain the shock pressures experienced by these rocks (~14-20 GPa); additional work on the response of biotite supports these constraints (Walton et al., 2018). Walton et al. (2017) studied the lower half of core ST003 (>242 m depth). Based on texture and mineralogy (clinopyroxene, sanidine, Ti-magnetite, and titanite), the breccia matrix was interpreted to have formed by recrystallization from an originally clastic matrix deposited at high temperatures (>800ºC). Recent studies focused on the composition of SRIS impact melt, present as clasts within the breccia. The melt is derived from various target material mixtures, including granite, shale, and carbonate, that experienced high temperatures and pressures during the impact (MacLagan et al., 2018; Walton et al., 2018). Both qualitative descriptions and quantitative data were used to divide the breccia into three main units (MacLagan et al., 2018). The uppermost units (<242 m depth), A and B, have a tan-coloured groundmass, sedimentary lithic clasts, and pale impact melt. Unit C (>242 m) contains green groundmass minerals, granitic lithic clasts, and dark-coloured impact melt (Fig. 1.4). These distinct units roughly correlate with the original stratigraphic relations of the target material – sedimentary units overlying granitic basement.

Minimal mixing and homogenization, as well as differential cooling rates with depth, may preserve large-scale layering in the SRIS impact breccia. Decomposed zircons in impact melt (Walton et al., 2017) indicate temperatures greater than ~1690ºC (Kaiser et al., 2008). Andradite and clinopyroxene forming from limestone clasts are evidence for carbonate decomposition in Unit C (Walton et al., 2017). In this lower unit of the impact breccia, limestone clasts are scarce, while clinopyroxene and garnet are prevalent. The melt-rich Unit C (>242 m) would have cooled slower relative to the upper breccia units (A and B) due to deeper burial. Additionally, impact melting of granitic rocks occurs at ~60 GPa and ~1500ºC (Stöffler and Grieve, 2007); compositional evidence of complete melting of granite has also been observed in Unit C (MacLagan et al., 2018). This

7

provides some insight into the high temperatures and pressures experienced by clasts and minerals throughout the breccia.
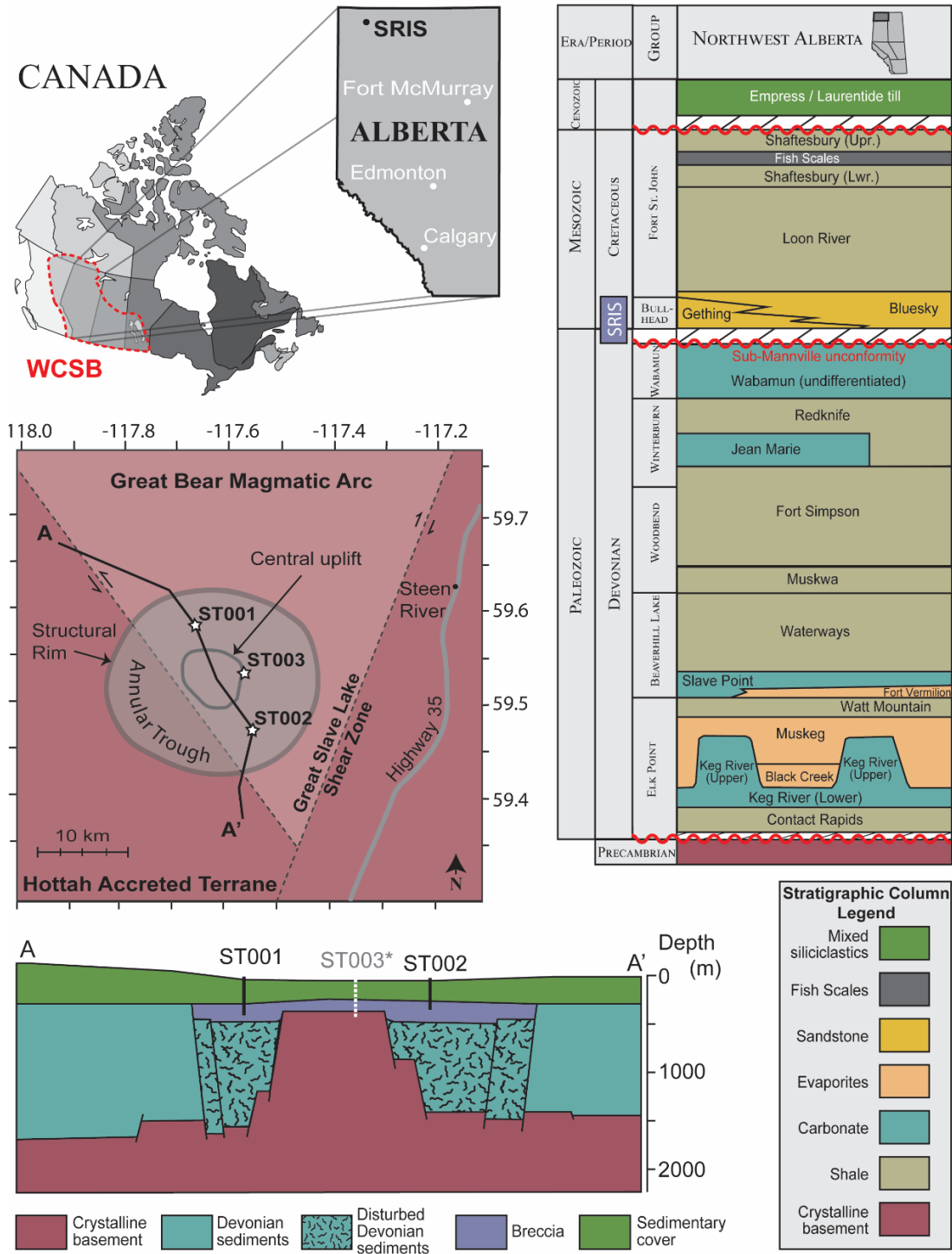
Figure 1. 3. Location and cross-section of the SRIS along with a stratigraphic column from NW Alberta. *Core ST003 is located behind the plane of cross-section A-A'; see plan view for exact location. WCSB=Western Canadian Sedimentary Basin. Modified from Molak et al. (2001) and MacLagan et al. (2018).

1.2 OUTLINE OF OBJECTIVES

Previous studies of the SRIS, outlined above, focused on core ST003 because it has the thickest sequence of impact breccia and penetrates ~11 m into the side of the central uplift. The compositions of individual clasts and mineral grains have been well described as a result; however, a detailed overview of ST003 and the two additional cores – ST001 and ST002 – is lacking. In addition, the age of the structure is poorly constrained, and the only published age is 91±7 Ma (Carrigy and Short, 1968), although this conflicts with overlying stratigraphy having been dated to ~108 Ma (Hathway et al., 2013). There were two main objectives for this thesis research. One tested the viability of hyperspectral imaging on drill core from an impact structure, assessed its potential for detailed mineralogical classification of an entire impactite sequence, and developed a model for SRIS impact breccia formation. The second aimed to constrain an age for the SRIS through U-Pb isotopic compositions of zircon grains from the structure.

1.2.1 CHAPTER 2 – HYPERSPECTRAL SCANNING

A common and well-known use of hyperspectral imaging is remote sensing, both on Earth and other planets. Hyperspectral scanning enables quick processing of large surficial areas, as well as detailed mineralogical identification and mapping (e.g. van der Meer et al., 2012). A similar application exists for imaging outcrop, hand samples, and drill core (Greenberger et al., 2015). The core is scanned with a spectrometer that measures the interaction of light with the sample surface. Reflectance spectroscopy depends on the ability of atoms in a mineral to absorb and emit specific wavelengths of light. Two processes define these capabilities: 1) electronic processes, whereby the types and characteristics of ions in the structure control the absorption abilities, and 2) vibrational processes, which are controlled by the atoms present in the mineral and how they are bound to one another (Hunt, 1977). The combination of these processes results in varied absorption and emission of different wavelengths of light from a particular material. Consequentially, the collected spectra contain distinguishing peaks and/or troughs, which can then aid in identifying the material in question – in this case, the mineralogy.

This study tests the viability of hyperspectral scanning to study drill core from an impact structure (Fig. 1.4). Impact breccias contain complex textures and minerals that are uncommon, or even absent, in traditional terrestrial environments, which offers a challenge in whole-scale

analysis of such units. Hyperspectral imaging was used to construct detailed mineralogical maps of the three drill cores that penetrate the crater-fill impact breccias (ST001, ST002, and ST003) at the SRIS. Three wavelength regions, from visible-near infrared to thermal infrared, provide a representative view of the impact breccia. The resulting maps were used to refine the emplacement mechanism of "suevite-like" impact breccia.
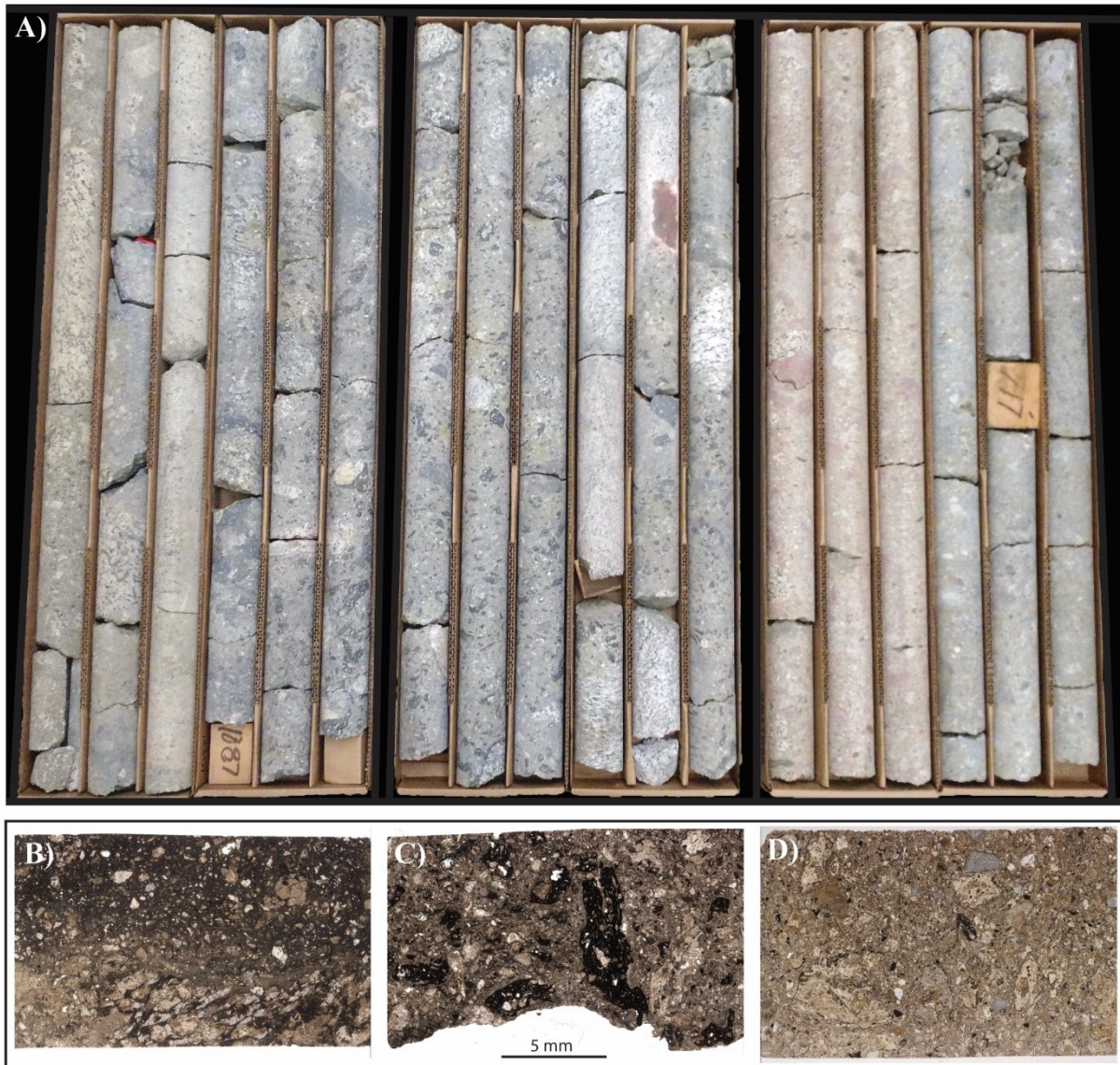
Figure 1. 4. Representative samples of core and corresponding thin sections from ST003. A) Six representative boxes of SRIS impact breccia. Box depths from left to right: 367-369 m, 329-331 m, 298-300 m, 272-274 m, 229-231 m, 217-219 m. B) Thin section from 1197' (364.8 m) depth showing gneiss (bottom) and agglomerated melt (top). C) Thin section from 950.5' (289.7 m) containing predominantly dark-coloured melt clasts. D) Thin section from 722' (220.1 m) with clasts of carbonate and light-coloured melt. All thin sections are in plane-polarized light and scale bar applies to B-D.

Suevite is defined as a polymict breccia containing clasts of cogenetic impact melt (Stöffler and Grieve, 2007; Stöffler et al., 2018), and its name is derived from the type locality at the Ries structure in Germany. Suevite-like breccia is found in many other terrestrial craters; this includes, but is not limited to: the Haughton crater in the Canadian Arctic (Osinski et al., 2005), the Chicxulub crater in Mexico (Hecht et al., 2004), the Brent crater in Ontario, Canada (Grieve, 1978), the Lappajärvi crater in Finland (Kukkonen et al., 1992), the Bosumtwi structure in Ghana (Boamah and Koeberl, 2006), the Roter Kamm structure in Namibia (Reimold et al., 1997), and the Popigai crater in Siberia (Bottomley et al., 1997). However, the formation mechanism is still debated within the impact community (Osinski et al., 2016). Our results highlight the large-scale layering observed in the three SRIS cores and the importance of volatiles in the formation of the suevite-like impact breccia at this crater. The maps also characterize an extensive suite of hydrothermal minerals, most notably, ammoniated feldspar and clay minerals, which provide insight into the post-impact hydrothermal system at the SRIS. Ammoniated minerals are detected relatively easily using short-wave infrared (SWIR) wavelengths, when they cannot be detected by other traditional techniques (e.g. EPMA).

1.2.2 CHAPTER 3 – GEOCHRONOLOGY

The only published age for the SRIS is a whole-rock K-Ar age of 95±7 Ma (Carrigy and Short, 1968), corrected with the updated decay constants of Steiger and Jager (1977) to be 91±7 Ma. However, the upper Loon River formation sits more than 100 m above the SRIS crater-fill material, and it has been dated using U-Pb, $^{40}Ar/^{39}Ar$, and foraminifera to be ~108 Ma. In addition, the Fish Scale Unit, dated at 101 Ma, is a distinct unit present in the Shaftesbury Formation, which is also logged as overlying the SRIS impact breccia. These overlying stratigraphic relationships imply that the SRIS must be at least 108 Ma in age. Further stratigraphic support may lie in the Bullhead Group, which consists of the Gething and Cadomin Formations. This Group is logged by McCleary (1997) to be present in the vicinity of the SRIS; however, the formation is not specified in that work. Neither the Gething, nor the Cadomin Formation have been logged in the units overlying the SRIS. The Cadomin, a well-known conglomerate unit present in the WCSB, has been dated as forming sometime between ~145 and ~113 Ma (Wrote and Leckie, 1999), and the Gething formed sometime in the Hauterivian to Early Albian (~133-108 Ma). If the Bullhead indeed extends as far into the Interior Plain as the location of the SRIS, then the absence of this

Formation provides a maximum age for the SRIS; if not, then the underlying Devonian sediments may offer the best constraint on the maximum age.

Currently, there are only 21 statistically viable ages (Jourdan et al., 2012) from among all 190 craters on Earth (Spray, 2018). Only four of these were based on Uranium-Lead (U-Pb) geochronology and all four used thermal ionization mass spectrometry (TIMS) on newly-crystallized zircons, or neoblasts (Jourdan et al., 2012). Recrystallized and granular zircons have been described in the SRIS (Walton et al., 2017; this study); however, neoblasts have not been observed. By using the fine resolution of secondary ion mass spectrometry (SIMS), this project aimed to date recrystallized zones of zircons from the SRIS with U-Pb geochronology.

The two main radiometric isotopes of uranium, ^{238}U and ^{235}U, decay into ^{206}Pb and ^{207}Pb, respectively. The half-lives of these minerals are billions of years (^{238}U: $T_{1/2}$=4.5 Ga; ^{235}U: $T_{1/2}$=0.7 Ga), so they are useful in dating ancient rocks (Ma) if we can measure the U and Pb abundances. This study used high voltage electrical shocks to liberate individual zircon grains from SRIS core samples. Zircon, a robust mineral commonly used for U-Pb radiometric dating, was extracted from granitic and quenched melt material with the aim of constraining an age for each. Not only can zircon survive the shock conditions of the impact environment (e.g. Timms et al., 2017), but when it crystallizes, zircon may incorporate U into the crystal structure; whereas the daughter product, Pb, is incompatible. If zircon experiences the right conditions for recrystallization during an impact, then it may undergo Pb-loss and resetting, which can record the timing of the impact event.

The geochemical data collected as part of this study allowed the SRIS zircons to be grouped into four main types. Together, these groups provide potential constraints on the timing of the impact event that formed the SRIS. One of the groups also corresponds to the known age of the Proterozoic, crystalline basement, and acts as an anchor for ages of the other zircon groups.

CHAPTER 2:
HYPERSPECTRAL IMAGING OF DRILL CORE

2.1 INTRODUCTION

Hypervelocity impacts occur when two planetary bodies collide at near-cosmic velocities (>11 km/s). Propagating shock waves cause impact metamorphism of target materials and result in the formation of a crater. The resulting impactites may be divided into shocked rocks, impact melt rocks, and impact breccias (Stöffler and Grieve, 2007). Polymict breccias containing clasts of impact melt within a particulate matrix are classified as "suevite" (Stöffler and Grieve, 2007). Although suevite *sensu stricto* is limited to the type locality at the Ries crater, Germany, this term has been loosely applied to any impact melt-bearing breccia and has been documented from small craters like Brent (D=3.8 km; Grieve et al., 1977) to larger structures such as Chicxulub (D≅200 km; Claeys et al., 2003). This breccia type typically forms a volumetrically significant portion of proximal impactites and is observed in a range of spatial contexts with respect to the crater structure; however, the formation mechanism is debated. Ries suevite has been proposed to form by fallback from an ejecta plume (Stöffler, 1977; von Engelhardt and Graup, 1984), as ground-hugging impact melt flows (Osinski, 2004), or as secondary explosions generated by the interaction of hot fluids with impact melt (Stöffler et al., 2013; Artemieva et al., 2013). There are likely multiple modes of generation for impact melt-bearing breccias, leaving this topic an active area of research.

Following impactite emplacement, fluid interaction with shock-heated rocks and elevated geothermal gradients in the central uplift may induce a hydrothermal system (Naumov, 2005), which can dissolve, transport, and precipitate new minerals. These yield information on the temperature, timing, heat and fluid sources involved. These systems may also create microbiological niches on Earth and potentially habitable environments on other planets (Cockell and Lee, 2002). Most impact events capable of producing complex craters can generate a hydrothermal system (Osinski et al., 2013), yet hydrothermal mineralization at only a handful of impact structures has been characterized in detail.

2.1.1 THE STEEN RIVER IMPACT STRUCTURE

The Steen River impact structure (SRIS) is located in NW Alberta, Canada (59º 31' N, 117º 38' W) in the oil- and gas-bearing Western Canadian Sedimentary Basin (WCSB) (Fig. 1.3). The structure lacks surface expression due to burial beneath ~200 m of Cretaceous shale and sandstone. Geophysical and drill-core studies delineate an average diameter of 22 km, a central uplift, annular trough, and radial faults (Molak et al., 2001). Target rocks comprised ~1.2 km of Devonian shales, carbonates, and evaporites overlying granitic Precambrian basement (Alberta Geological Survey, 2015). The widely cited age of the structure is 91±7 Ma (Carrigy and Short, 1968); although this contradicts with overlying stratigraphy and is discussed further in Chapter 3. Kimberlite pipes in the SRIS vicinity led to renewed drilling in 2000 which produced >1 km of total core from three wells, ST001, ST002, and ST003. These provide continuous samples of the crater-fill impactites (Figs. 1.3 & 1.4).

2.1.2 STUDY OVERVIEW

Hyperspectral scanning has been used to characterize drill core since the 1990's (Kruse, 1996); however, this method has been underutilized by the terrestrial impact community. Here, hyperspectral imaging was used to create detailed mineralogical maps of impact breccia in drill cores ST001, ST002, and ST003 (Figs. 2.1 & A.2). Previous studies characterized the breccia groundmass between 242–381 m (Walton et al., 2017), and impact melt clasts (MacLagan et al., 2018) in ST003. These earlier works provide compositional and textural information from specific core depths that enhance interpretation of larger-scale hyperspectral mineralogical maps. The results reveal, for the first time, a post-impact hydrothermal system at this mid-size complex crater and have implications for the role of volatiles in suevite-like breccia formation at the SRIS; this may extend to other structures with sedimentary target rocks, accounting for ~70% of the Earth's current impact structure inventory.
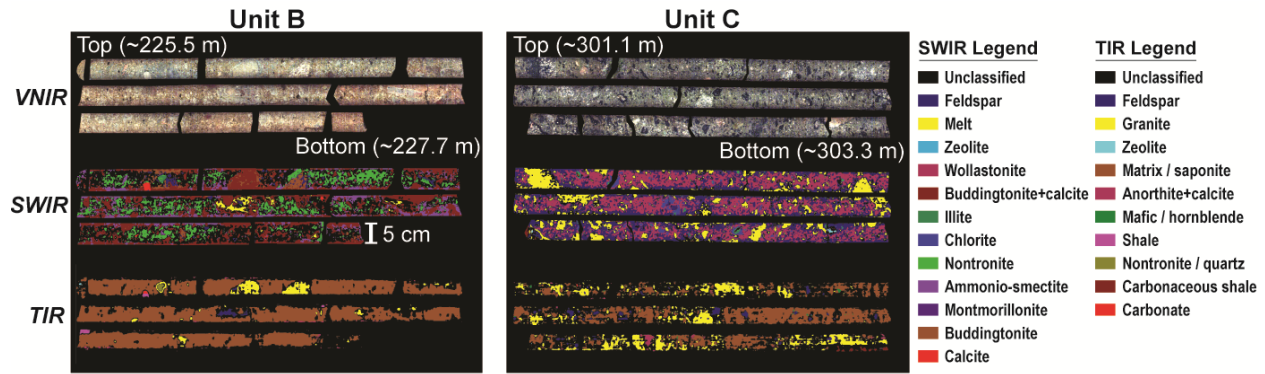
Figure 2. 1. A subset of Figures A.1 and A.2 comparing Units B and C from ST003 using all studied wavelength regions (VNIR, SWIR, and TIR). VNIR channels used are R:702.13, G:548.67, and B:470.34 nm. See color legend for SWIR and TIR endmember mineral labels.

2.2 METHODS

Two automated SisuRock imaging spectrometers were used to scan SRIS core at the University of Alberta, Canada. Visible-near infrared (VNIR) and shortwave infrared (SWIR) reflectance spectra (400–2500 nm) were collected at resolutions of ~0.2 and ~0.5 mm/pixel, respectively. Thermal infrared (TIR) reflectance (8–12 µm) was measured with a lower resolution of ~0.8 mm/pixel. Original radiance data, containing 98 VNIR, 256 SWIR, and 120 TIR bands, were normalized to the radiance of a 99% Spectralon™ white panel (VNIR & SWIR) or an anodized aluminum plate (TIR) to obtain reflectance.

Each of the nine raw spectral data sets – VNIR, SWIR, and TIR data from ST001, ST002, and ST003 – included impact breccia with a few meters of overlying shale. In total, ~167 m of ST001, ~55 m of ST002, and ~181 m of ST003 (~200 core boxes in total), were scanned over ~11 hours. The Environment for Visualizing Images (ENVI) software (Harris Geospatial Solutions) was used to process data. VNIR images offer an original visual representation of the cores (Fig. A.1). An automated endmember extraction collected 70–100 spectra from each set, which were grouped and averaged for both SWIR and TIR datasets, separately. The spectral angle mapper (SAM) algorithm compared our spectra to ENVI mineral spectral libraries compiled by the U. S. Geological Survey (USGS) (Clark et al., 2007), the NASA Jet Propulsion Laboratory (JPL), and the Johns Hopkins University (JHU) (Baldridge et al., 2009) for mineral classification. Individual core maps were made with 13 SWIR and 11 TIR endmembers (Fig. A.2). Areas of core ST003 encompassed by each of the SWIR endmembers were sampled for X-ray diffraction (XRD)

analysis to refine the spectral mineral identification. For details on the analytical methods and full spectral maps, see the Appendix.

2.3 RESULTS

Fine grain size and low scan resolution (see above), cause pixels from the breccia groundmass to contain multiple minerals. High-resolution scanning electron imaging of the groundmass, the fraction supporting larger lithic and impact melt clasts, identified Ca-pyroxene, feldspar, titanomagnetite, garnet, and titanite <100 µm in size (Walton et al., 2017). As the highest resolution of SWIR scans is ~0.5 mm/pixel, these spectra are a spectral average of all groundmass minerals. Specifically, the SWIR "feldspar" endmember represents a mixture of feldspar, clinopyroxene, and derived alteration products (clays). Grains or clasts larger than the scan resolution (≥5 mm) will map as a pure endmember.

2.3.1 SWIR SPECTRA

SWIR reflectance (~1000–2500 nm) is ideal for characterizing alteration minerals, such as iron-bearing and clay minerals, as summarized in Hunt (1977). Quartz and feldspar lack spectral expression in this wavelength region. In this study, illite and muscovite, and clinochlore and epidote cannot easily be separated; however, major element abundances (Walton et al., 2017) and our XRD results indicate that all four minerals are present. The 13 mapped SWIR endmembers include calcite, buddingtonite (an ammonium-feldspar), ammonio-smectite, analcime, nontronite, a buddingtonite + calcite mixture, gypsum, montmorillonite, illite and/or muscovite, epidote and/or clinochlore, feldspar, wollastonite, and granite-derived impact melt (Fig. 2.2).

2.3.2 TIR SPECTRA

TIR endmembers have distinct, low amplitude peaks (Fig. 2.3). Feldspars, clay minerals, pyroxenes, and amphiboles have broad reflectance features at similar wavelengths (~8–10 µm), making their differentiation difficult with the coarse spectral resolution of our TIR imaging system. Classification of most TIR endmembers was refined using VNIR and SWIR data. These endmembers include gypsum and/or barite, analcime, carbonate (marble), nontronite and/or quartz, alkali feldspar, shale, calcareous shale, biotite and/or saponite, hornblende, alkali granite, and an anorthite + calcite mixture (Fig. 2.3).

2.4 DISCUSSION

2.4.1 MINERALOGICAL LAYERING IN HYPERSPECTRAL MAPS

The hyperspectral maps (Fig. A.2) delineate three distinct breccia Units (A–C), corresponding to those described by MacLagan et al. (2018). Overlying shale classifies as a mixture of clays and calcite in the SWIR. TIR data shows calcareous shale in all three cores, with additional siltstone in ST003 attributed to variations in the amount of carbonate throughout the stratigraphy. The shale contacts uppermost impact breccia Unit A, which is grey in color, and highly friable with minimal identified impact melt phases (Fig. A.1). In the SWIR map, Unit A contains ammonio-smectite, montmorillonite, and minor zeolite. In all three TIR maps, Unit A spectra have low reflectance due to the crumbly nature of the material, but are predominantly zeolite, with some limestone and lithic shale clasts (Fig. A.2).

Unit A rapidly transitions to underlying Unit B, the latter characterized by a tan- or red-colored groundmass, pale impact melt clasts, and lithic sedimentary clasts (Figs. 2.1 & A.1). SWIR-identified minerals are nontronite, NH_4-smectite, buddingtonite, calcite, gypsum, feldspar, and minor zeolite. In TIR, Unit B is predominantly saponite with lesser feldspar and areas of the core mapped as a granite-like composition (quartz + feldspar). The low spatial resolution of TIR maps (see above) causes difficulties in spectral distinction between fine-grained groundmass and granite lithic clasts, which appear abundant in Unit B. Rather, VNIR and SWIR data show the lithic clast population is dominated by limestone and shale (Figs. A.1 & A.2).

Where Unit B transitions to Unit C, the groundmass color becomes distinctly green (Figs. 2.1 & A.1). Dark-colored impact melt clasts and granite lithic clasts become prevalent. This transition is poorly defined in the TIR map (Fig. A.2), where Unit B saponite and feldspar continue to dominate the groundmass; however, it is demarcated by the appearance of a granitic composition and Ca-rich phases throughout Unit C. In the TIR, these areas of Unit C map as carbonaceous shale or a mixture of calcite + anorthite (Fig. A.2).
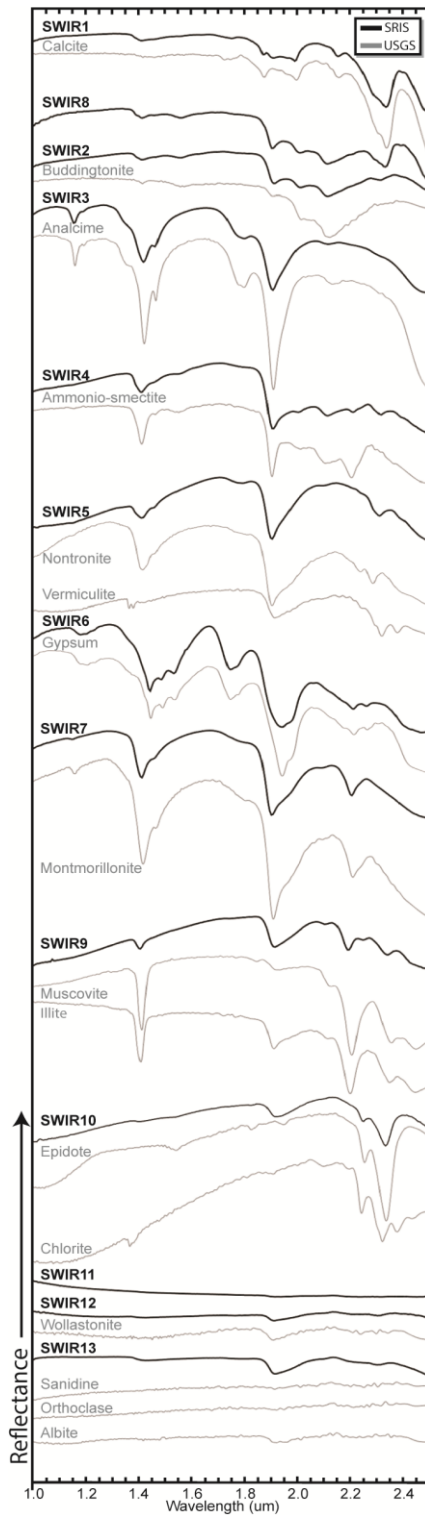
Figure 2. 2. Our SWIR endmember spectra compared to USGS spectral library match(es) (Clark et al., 2007).
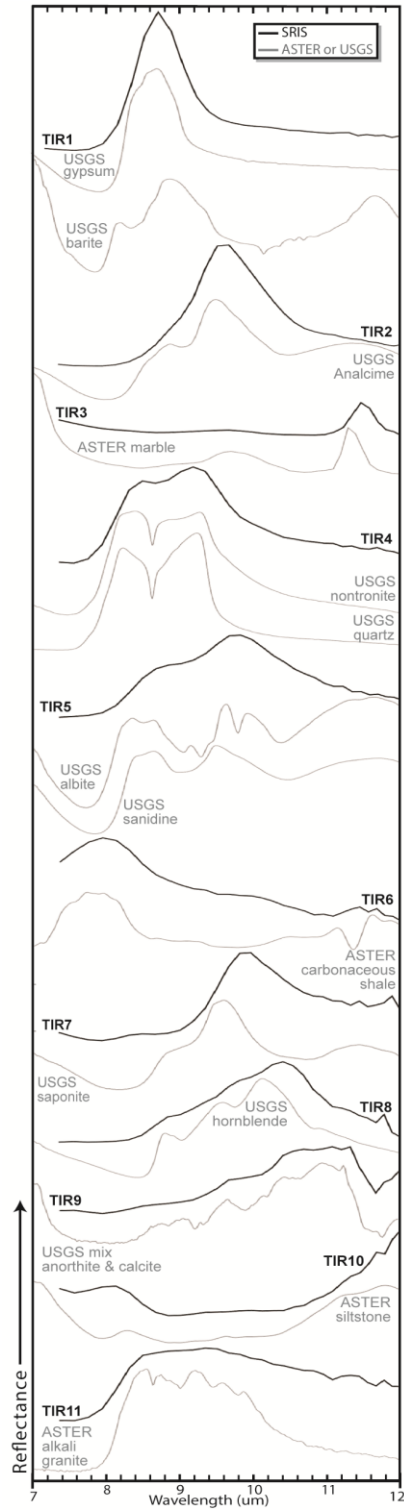
Figure 2. 3. Our TIR endmembers compared to USGS (Clark et al., 2007) or ASTER (Baldridge et al., 2009) spectral library match(es).

18

In the SWIR, the same groundmass areas map as the pyroxenoid "wollastonite" with feldspar and minor clay minerals. However, all the Ca-phases are likely Ca-pyroxene (diopside) based on XRD results (Table A.1) and Raman spectra (Walton et al., 2017). Both TIR and SWIR maps highlight clasts of granite, granite-derived impact melt, and sparse limestone.

Where Unit B transitions to Unit C, the groundmass color becomes distinctly green (Figs. 2.1 & A.1). Dark-colored impact melt clasts and granite lithic clasts become prevalent. This transition is poorly defined in the TIR map (Fig. A.2), where Unit B saponite and feldspar continue to dominate the groundmass; however, it is demarcated by the appearance of a granitic composition and Ca-rich phases throughout Unit C. In the TIR, these areas of Unit C map as carbonaceous shale or a mixture of calcite + anorthite (Fig. A.2). In the SWIR, the same groundmass areas map as the pyroxenoid "wollastonite" with feldspar and minor clay minerals. However, all the Ca-phases are likely Ca-pyroxene (diopside) based on XRD results (Table A.1) and Raman spectra (Walton et al., 2017). Both TIR and SWIR maps highlight clasts of granite, granite-derived impact melt, and sparse limestone.

Granitic basement is encountered at 370 m depth in ST003 (Figs. A.1 & A.2). The prevalent impact melt pixels of Unit C terminate abruptly and are underlain by feldspar, illite, chlorite, and minor wollastonite. The basement, like Unit C, is classified as granite and feldspar so the transition is not obvious in TIR. The ratio of granitic material to feldspar increases slightly below 370 m depth, but is only distinguishable when compared with the distinct transition in the SWIR map.

2.4.2 FORMATION OF SUEVITE-LIKE BRECCIAS AT STEEN RIVER

The thick, exceptionally well-preserved sequence of impact melt-bearing breccias at the SRIS, akin to Ries suevite, is one of relatively few such examples. Hyperspectral mapping reveals large-scale mineralogical layering within the continuous breccia; uppermost Units A and B are derived predominantly from sedimentary target materials, and lower Unit C from crystalline basement rocks. The breccia sequence therefore shows little evidence of disturbance after deposition, riding passively on the top of the parautochthon during late-stage movements (e.g. central uplift formation; Fig. 1.3). Previous studies of SRIS impact melt clasts show that major element compositions can be modeled by suitable target rock mixtures including carbonate- (Walton et al., 2018), granite-, and shale-derived melt (MacLagan et al., 2018). This compositional variation strongly contrasts with large sheets of igneous-textured impact melt, observed in craters

formed entirely within crystalline rocks (e.g., Mistastin structure; Grieve, 1975), which generally show minimal compositional variation (e.g., Dence, 1971; Grieve, 1975). The wide range of SRIS impact melt clast compositions requires early segregation by another agent, namely volatiles from phyllosilicates or carbonates. At craters formed in sedimentary rocks, like the SRIS, volatiles may be active from the initiation of shock melting. Therefore, the impact melt at no point merged into large bodies, as required by the fuel-coolant interaction hypothesis (Stöffler et al., 2013), and this model cannot be applied to the SRIS. Rather, our results highlight the inherent role of volatiles in forming impact-melt-bearing polymict breccias.

2.4.3 POST-IMPACT HYDROTHERMAL MINERALIZATION

Hydrothermal alteration in terrestrial volcanogenic settings is often characterized by assemblages of carbonate, oxide, and clay minerals, the distinct SWIR features of which can be used to identify formation environments (van der Meer et al., 2012). Maps of the SRIS impact breccias contain similar minerals – nontronite, montmorillonite, illite, epidote, zeolites, chlorite, gypsum, barite, and calcite – indicating pervasive alteration. The distribution of these minerals is consistent across the three studied cores, with a slightly higher abundance of clay minerals (illite, montmorillonite, nontronite) in ST001 and ST002. This suggests that heat driving the hydrothermal system was largely homogeneous across the crater and derived from the breccia, with subsidiary heat provided from the central uplift.

Structurally-bound ammonium (NH_4^+) is easily identified using near-infrared spectroscopy (e.g. Berg et al., 2016) and quantified using differential thermal analysis (e.g. Bishop et al., 2002). In contrast, standard core analysis techniques, such as X-ray fluorescence, are unable to identify NH_4^+ phases. Although observed in volcanogenic hydrothermal settings (Baugh et al., 1998; Krohn et al., 1993), ammonium-associated buddingtonite and montmorillonite have not been described from impact-associated systems. In hydrocarbon-producing areas from the United States, fixed NH_4^+ in clay minerals is associated with crude oil (Williams et al., 1989). Therefore, nitrogen in the SRIS may have an organic origin attributed to oil and gas producing units in the WCSB. Buddingtonite and ammonio-smectite are most abundant in the upper breccia units, suggesting that nitrogen may be sourced from the overlying shale, or atmospheric N was microbially fixed and incorporated before significant post-impact burial occurred. Due to similar ionic size, NH_4^+ can substitute for K^+ in clays and feldspars (Krohn et al., 1993); granite-derived feldspar at the SRIS

20

was likely ammoniated in this way. As nitrogen is essential for biological processes, hyperspectral detection of NH_4^+ has implications for studying impact-associated habitable environments on early Earth and, potentially, on other planets.

2.4.4 THE CASE OF THE MISSING DOLOMITE

Although dolomite can be detected hyperspectrally, and was present in the target rocks, spectral matches were not found in our data. Instead, calcite is the dominant carbonate mineral in our spectra. The apparent absence of dolomite in the SRIS breccias may be attributed to post-impact dissociation of dolomite, $CaMg(CO_3)_{2(s)} \rightarrow CaO_{(s)} + MgO_{(s)} + 2CO_{2(g)}$, requiring temperatures >775ºC (Otsuka, 1986). Dolomite dissociation is expected at the SRIS based on previous temperature estimates for deposition of Unit C (≥800 ºC; Walton et al., 2017). Calcium and magnesium oxides released during this reaction may combine with silica, accounting for the abundance of Ca-, Mg-rich pyroxene in the core, as detected in our SWIR maps.

2.4.5 FURTHER APPLICATIONS OF HYPERSPECTRAL CORE SCANNING

Of the 190 confirmed terrestrial impact structures, roughly half have been drilled (Spray, 2018). Our results showcase an efficient and cost-effective method for characterizing the mineralogy of drill core. Hyperspectral imaging provides a map from which sampling can be conducted, rather than relying on visual assessment or systematic sampling. This method could be utilized for existing and new cores collected on Earth and other planetary bodies, supported by additional analyses (e.g. XRD, SEM, EMPA) to provide tighter textural and compositional constraints.

CHAPTER 3:
GEOCHRONOLOGY OF ZIRCONS

3.1 INTRODUCTION

Of the ~190 confirmed impact structures on Earth (Spray, 2018), only a small percentage have a precise age (Jourdan et al., 2012). Common dating methods for terrestrial rocks include radiometric U-Th-Pb, K-Ar, Rb-Sr, Sm-Nd, Lu-Hf, or ^{14}C dating (using organic matter within the rocks); however, the unique environments of impact events may render these methods less effective due to the extreme shock effects experienced by the rocks. In addition, impact structures often display intense alteration of minerals through post-impact hydrothermal activity (Osinski et al., 2013), and this process may affect the radiometric systems. On the other hand, if impact-induced hydrothermal activity is relatively short-lived, the timing of hydrothermal mineralization may aid in constraining an age for the structure (e.g., Alwmark et al., 2017). Constraining the age of impact events allows for improved correlation with surrounding stratigraphy, to the paleoecology of the region, and to the impact record as a whole.

The Steen River impact structure (SRIS) is a buried, complex crater located in NW Alberta, Canada, that formed in mixed target rocks – Devonian shales, carbonates, and evaporites overlying metamorphosed igneous rocks of the Canadian Shield (Fig. 1.3). The basement rocks include the Great Bear Magmatic Arc (1875-1840 Ma), and the Hottah Terrane (1902-1914 Ma; Hildebrand et al., 1987), which are both truncated by the Great Slave Lake Shear Zone (Fig. 1.3). The Great Bear now underlies most of the structure and the entire central uplift. The Proterozoic basement was unconformably overlain by Devonian sedimentation beginning around 400 Ma. Subsequent deposition throughout the Paleozoic was removed by erosion, resulting in an unconformable contact between Devonian units and Cretaceous sandstones and shales (Alberta Geological Survey, 2015). The thickness of post-impact shales, sandstones, and glacial till totals ~200 m. The shales of the Bluesky immediately overlie the SRIS crater-fill material and are intercalated with lenses of breccia up to 2 m above the contact. The Bluesky is overlain by the shales of the Loon River and Shaftesbury Formations; all three Formations are part of the St. John's Group. Currently, a single published K-Ar whole rock age of 91±7 Ma (pyroclastic sample) exists for the structure (Carrigy and Short, 1968); however, this contradicts the age of older overlying units. The SRIS therefore remains a target for additional geochronology to constrain the timing of its formation.

3.1.1 ZIRCON IN IMPACT STRUCTURES

In 2009, 174 impact structures were confirmed on Earth, 11 of which had robust ages (Jourdan et al., 2009). As of 2012, eighty-five of the total 179 confirmed impact structures had reported ages, and the number that were statistically viable had increased to 21 (Jourdan et al., 2012). Of these 21 viable ages, 4 were measured using U-Pb geochronology: Manicouagan (Hodych and Dunning, 1992), Morokweng (Hart et al., 1997), Sudbury (Krogh et al., 1982; Kenny et al., 2017), and Vredefort (Moser, 1997; Gibson et al., 1997; Kenny et al., 2017; Cavosie et al., 2015; Moser et al., 2011; Kamo et al., 1996). Other craters that have been dated using U-Pb in zircons, with variable success, include the Acraman structure, Australia (Schmieder et al., 2015), the Gardnos structure, Norway (Kalleson et al., 2009), the Haughton structure, Canada (Scharer and Deutsch, 1990), the Araguainha structure, Brazil (Tohver et al., 2012), and the Siljan structure, Sweden (Aberg and Bollmark, 1985).

Studies of zircon grains from impact structures show that a variety of shock-induced deformation microstructures and phase transformations can be expected. Deformation microstructures may include planar fractures (PFs) and/or planar deformation features (PDFs) – narrow (<2 µm), parallel, closely-spaced sets of amorphous lamellae (e.g. Wittmann et al., 2006; Ferrière and Osinski, 2013). Zircon may transition to the high-pressure polymorph, reidite, at pressures >20-30 GPa, which is often associated with the formation of planar microstructures in the host zircon (e.g. Gucsik, 2007; Reddy et al., 2015; Erickson et al., 2017; Timms et al., 2017; Wittmann et al., 2006; Glass and Liu, 2001).

Due to the high pressures and temperatures of shock metamorphism (Fig. 1.2), zircon may also decompose or recrystallize. At temperatures >1100ºC, and P>50 GPa, zircon could begin to recrystallize, and at T>1673ºC, P>52 GPa, can dissociate into zirconia (baddeleyite, ZrO_2) and a silica phase (Cavosie at al., 2016, Timms et al., 2017; Kaiser et al., 2008; Wittmann et al., 2006; El Goresy, 1965). Recrystallization of zircon may be identified through the "smoothing" of igneous zoning, or the production of granular textures, consisting of recrystallized granules of zircon in an amorphous matrix (Cavosie et al., 2015; Wittmann et al., 2006). Conversely, the presence of baddeleyite and an amorphous Si- or Zr-oxide are indicative of decomposition (Wittmann et al., 2006; Timms et al., 2017; El Goresy, 1965). Recrystallized zircon granules and newly-formed baddeleyite may be ideal candidates for dating impact structures, because the zircon

U-Pb system can be reset by the impact (e.g. Timms et al., 2017). The closure temperature for Pb diffusion in zircons is generally >900ºC (Cherniak and Watson, 2000) However, very few impact structures have been dated using this method, due to issues associated with their small grain sizes and the potential for Pb-loss (Jourdan et al., 2012; Kenny et al., 2017).

3.1.2 STUDY OVERVIEW

The SRIS contains a unit of impact breccia, ~150 m thick, that overlies the central uplift and disturbed Devonian units (Fig. 1.3). The breccia is polymict, bearing shocked mineral and lithic fragments, as well as clasts of quenched impact melt. These are embedded in a fine-grained groundmass which may be clastic or composed of new minerals (feldspar, clinopyroxene, titanite, sanidine, garnet, and titanomagnetite) formed by solid-state grain growth (Walton et al., 2017; MacLagan et al., 2018). Much of the groundmass and clasts have been replaced by hydrothermal alteration minerals (clay-, oxide-, and carbonate-assemblages), as described in Chapter 2. Hydrothermally-deposited minerals are common in impactites, due to the residual post-impact heat that may drive fluid circulation (Osinski et al., 2013).

This study analyzed isolated zircon grains, collected from both impact melt clasts and lithic granite clasts in impact breccias, to constrain an age for the SRIS. Samples from the basement material in the central uplift (~1.8 Ga) act as a basis for comparison with those derived from impact melt clasts. Scanning electron microscope (SEM) imaging has shown that zircons from impact melt contain decomposition and recrystallization textures (Walton et al., 2017; this study); these textures are known to provide constraints on the ages of impact melts and corresponding structures (e.g. Moser et al., 2011). Constraining the age of the SRIS will enable better correlation to the surrounding stratigraphy of the WCSB, and aid in linking the structure to mineral deposits and the paleoecology of the area.

3.2 METHODS

Current studies of the SRIS focus on samples from three continuous diamond drill cores, ST001, ST002, and ST003. Thin sections from each core were scanned on a Nikon scanner in plane-polarized and cross-polarized light. The resulting images were used to guide SEM studies in locating zircon grains and recording their microstructures. Zircons in 16 thin sections from ST003 (Fig. 3.1) and 1 thin section from ST001 were imaged to ascertain the textures present in

these grains, and to assess their potential for U-Pb geochronology. The SEM parameters were set at an extra-high tension (EHT) of 20 kV, an I-probe current of 200 pA, and a store resolution of 1024x768 pixels. SEM images were acquired in back-scattered electron (BSE) imaging mode. In addition to zircon, thorite ([Th,U]SiO$_4$) was discovered, which displayed similar grey-scale to zircon (Fig. 3.1).

Further imaging was carried out using cathodoluminescence (CL) on an SEM at the University of Alberta's Canadian Centre for Isotopic Microanalysis (CCIM) to examine the textural differences between granite-hosted and impact-melt-hosted zircons. To separate zircon grains from the core samples, a SelFrag instrument at Queen's Facility for Isotopic Research (QFIR) in Ontario, Canada, was used to fragment five whole-rock samples from ST003. This method allows for separation of minerals along grain boundaries with minimal damage to the grains themselves. These samples were selected from representative parts in the core that contain cm-sized portions of impact melt or relatively unaltered granite. Two granite samples from 378.4 m (235.38 g) and 344.1 m (102.85 g) depth and three melt clast samples from 368.8 m (89.26 g), 360.0 m (159.72 g), and 291.4 m (89.26 g) depth were fragmented (Fig. A.3), each in 3.1 L of water. The samples were pulsed for 300 pulses at a frequency of 5.0 Hz and a 155.2 kV potential. The instrument and sample vessel were cleaned between each sample, followed by a marble rock blank of Grenville age that contains no zircon or heavy mineral concentrates. The suspended load was decanted from the sample vessel and then settled, while the coarse particles could be collected from the bottom of the vessel. The samples were stored in reverse osmosis water before being dried overnight at 60ºC in pre-weighed glass petri dishes (Fig. 3.2A).

Once dry, the samples were hand-sieved to remove grains >250 μm, and a powerful hand magnet was used to separate the most magnetic fraction. The remaining material was processed using a Frantz magnetic separator under no current, followed by 0.2A, 0.4A, and 0.6A currents (Fig. 3.2B). After each increment, the samples were collected in separate vials. The non-magnetic fraction (Fig. 3.2C) underwent heavy liquids separation in 3.32 g/cm^3 Methylene Iodide (MeI). The sample was stirred into the MeI and then allowed to settle for 15-20 minutes. The MeI was drained off to collect the heavy material, including the zircons. This fraction was rinsed with acetone under vacuum to clean off any remaining MeI, and the heavy separates were stored in ethanol.
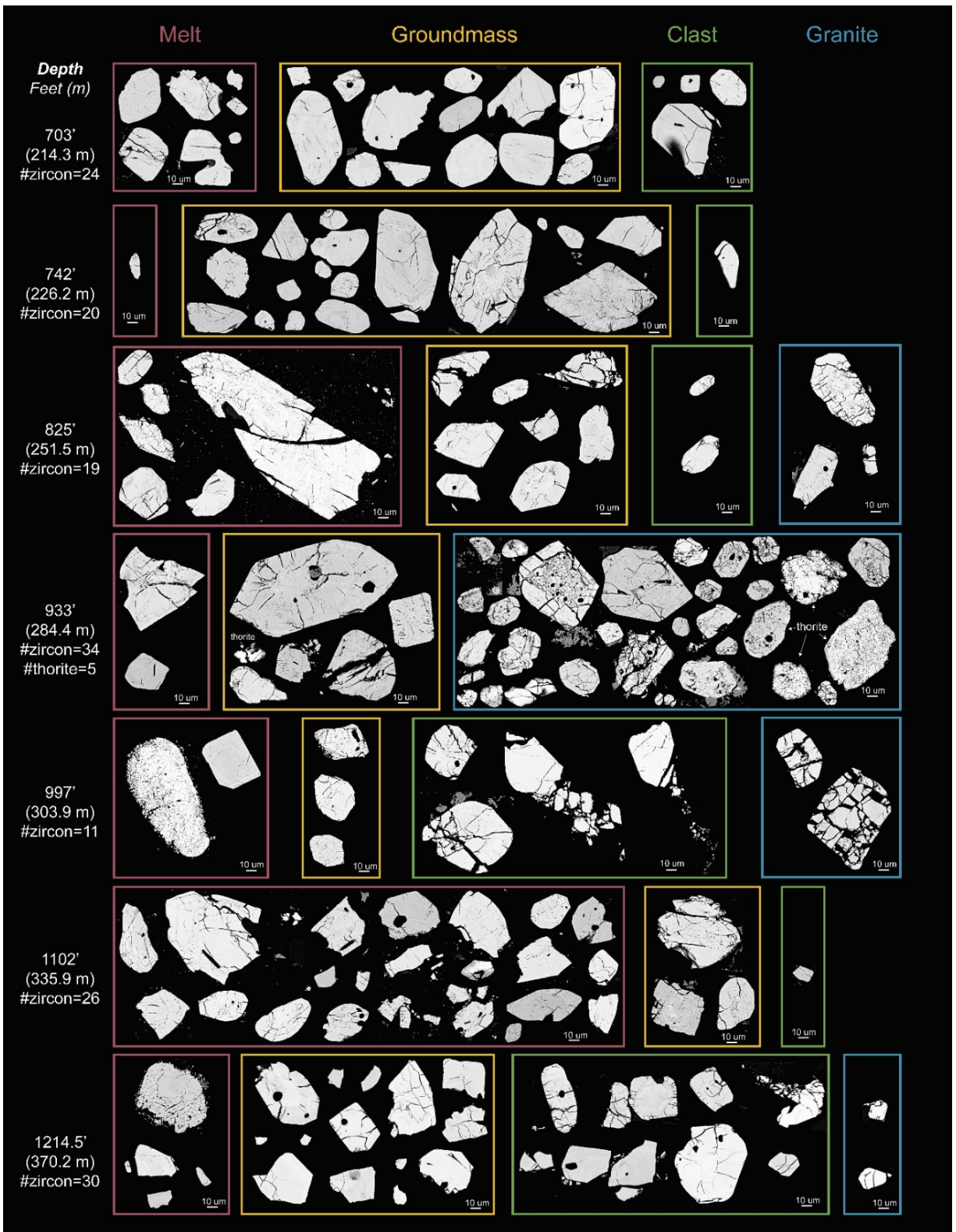
Figure 3. 1. BSE images of in-situ zircon grains from six different depths in core ST003. Scale bar (10 µm) is the same size for each box.
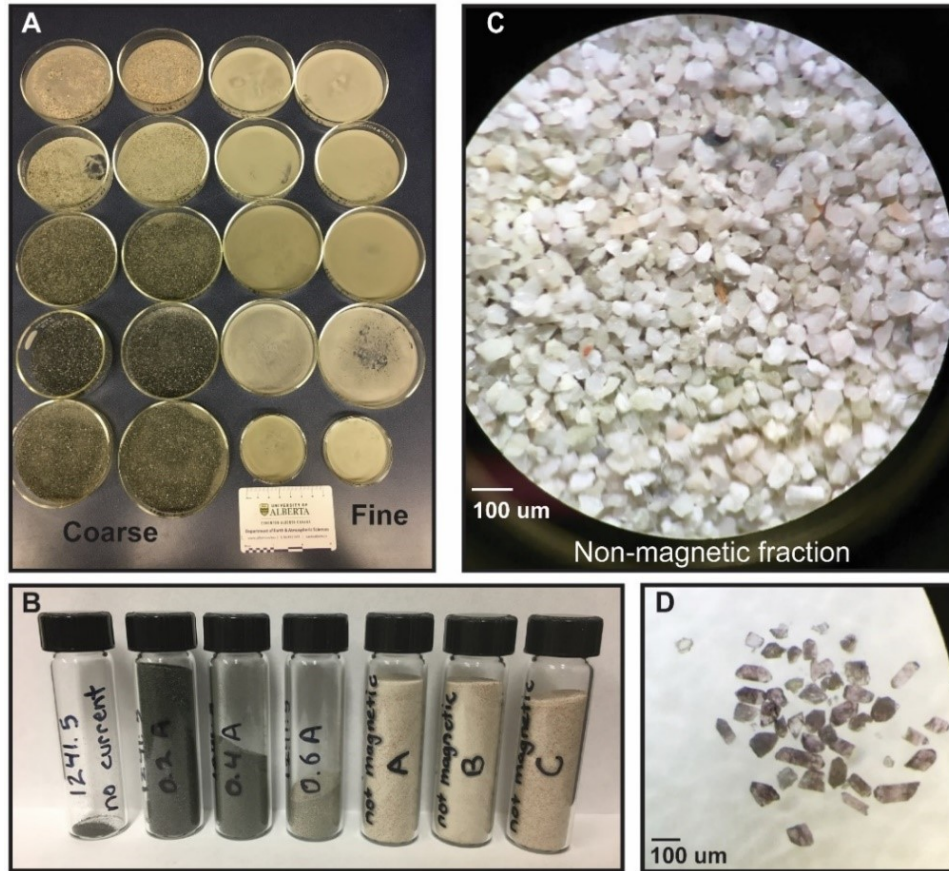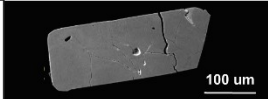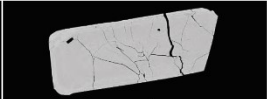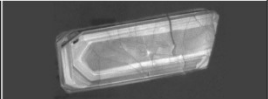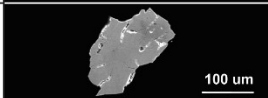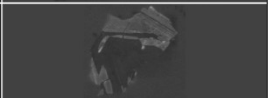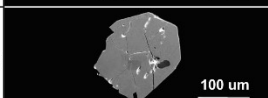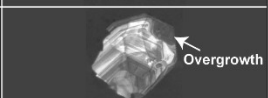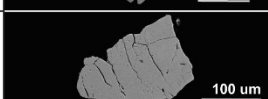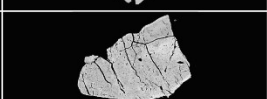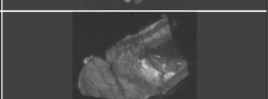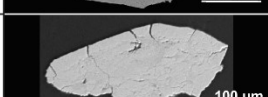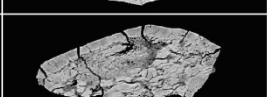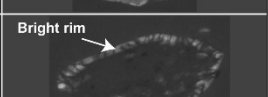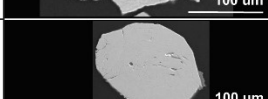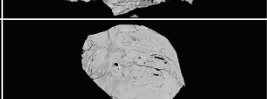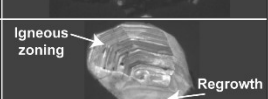
Figure 3. 2. Stages of zircon extraction from SRIS samples. A) Sediments resulting from SelFrag. B) Vials of fine sediment after sieving, heavy liquids separation, and processing with Frantz magnetic separator. C) Magnified image of non-magnetic fraction from B. D) Separated zircons from C.

A dissecting microscope was used to separate the zircon grains from the remaining heavy fraction. Most of the zircons are ≤100 µm in size and have a purple color (Fig. 3.2D). These were mounted in epoxy and polished before imaging and characterization on the SEM. Six zircon groups were defined using textural characteristics only; these are listed and described in Table 3.1. Spots were chosen from each of the zircon groups (Fig. A.4), with a preference for Groups 1 and 2 from the granite and Groups 4 through 6 in the melt samples. These samples were analyzed on a SIMS at the Geological Survey of Canada in Ottawa. The following parameters were used: a primary beam of 10 keV mass-filtered $^{16}O^-$ ions projected onto the sample through a 50 µm aperture to produce a ~10 µm diameter probe spot. The ages were calibrated against 6266 zircon reference material (Table A.4) (Stern and Amelin, 2003). Additional details on the analytical conditions and spot locations can be found in the Appendix.

Table 3. 1. Zircon groups, according to physical appearance. Scale bar applies to all three image types.

Original zircon group (pre-SIMS)	New zircon type (post-SIMS)	Characteristics	Secondary Electron (SE) Image	Backscattered Electron (BSE) Image	Cathodoluminescence (CL) Image
Group 1	Type 1a	Well-preserved igneous zoning	100 um		
Group 2	Type 2	Altered version of Type 1, maintains igneous zoning but is dark in CL	100 um		
Group 3	Type 1b	Possible metamorphic overgrowths; zoning present in the rest of the grain	100 um		Overgrowth
Group 4	Type 3	Structurally disturbed, typically dark in CL, "fuzzy" appearance	100 um		
Group 5	Type 4	Thin rim of new growth that is bright in CL	100 um		Bright rim
Group 6	Type 1b	Smooth, dark regions in CL that cross-cut igneous zoning	100 um		Igneous zoning / Regrowth

After collection of SIMS data, and construction of initial Concordia plots with all collected points, the data were filtered to remove the most inaccurate points. The zirconia monitor peak ($^{196}Zr_2O$), measured in counts·second^{-1}, was normalized to the beam intensity in nA. An acceptable range of values (counts·sec^{-1}·nA^{-1}) was defined based on those of the undisturbed igneous zircons (Type 1a and 1b). For $^{196}Zr_2O$, this range encompassed 1800-2500 counts·sec^{-1}·nA^{-1}. In addition, an acceptable range was defined for the $^{254}UO/^{238}U$ ratio, which measures the accuracy relative to a standard material. This encompassed ratios from 5.8-6.7; any points outside of these defined ranges were not plotted. An additional plot was made that excluded any points with >10% common Pb, although this was found to not significantly alter the intercept values.

3.3 RESULTS

3.3.1 SEM IMAGING

A wide diversity of zircon shapes and sizes exist within the studied grains, displaying a range of robustness from euhedral to heavily fractured or fragmented (Fig. 3.1). Zircons are found in four main locations: entrained in impact melt clasts, as accessory minerals in the groundmass, enclosed within a larger mineral clast, or remaining in a lithic clast of granite parent material.

Grains within clasts of impact melt exhibit the highest degree of fracturing and granularity, although there are examples of zircons entrained within impact melt clasts that are euhedral and maintain distinct igneous zoning. This zoning is characterized by concentric bands of varying composition, namely U abundance, that are parallel to the crystal faces (Table 3.1, Fig. 3.3A). Some melt-hosted grains also show partial to complete smoothing of the igneous zoning. Zircons that were liberated from their igneous parent rock and survived as accessory minerals within the breccia groundmass also display significant fragmentation. Based on physical appearance alone, these grains are difficult to differentiate from impact melt-hosted zircons (Fig. 3.1).

Some zircons remain enclosed within a larger mineral clast (e.g. quartz, feldspar, or biotite); these grains are also highly fractured and fragmented, but do not display the fine, granular textures observed in the impact melt- and groundmass-hosted zircons (Fig. 3.3). The final subset of zircons, located within granitic clasts, display extreme diversity in appearance. A variety of textures are observed, including granular textures, nearly euhedral grains, and both intact and broken and/or sheared grains. Thorite grains display similar textures to the zircons. All localities contain a handful of zircons with microvesicles (Fig. 3.3E, F), which generally follow igneous zoning patterns. Although sub-micron granular textures have been observed in the SRIS zircons, larger neoblasts (>1 μm) have yet to be discovered. Larger neoblasts would be necessary to attain the highest age precision possible. The smallest spot size for SIMS is 5 μm; therefore, the minimum neoblast size for this method is 5 μm.

3.3.2 SIMS ANALYSIS

The data collected from samples and standards can be found in the Appendix (Tables A.3 and A.4). When looking at the raw, unfiltered data, Group 1 zircons, which are the least fractured and preserve clear igneous zoning with minimal defects (Table 3.1), are concordant with a mean $^{207}Pb/^{206}Pb$ age of 1865±16 Ma (Fig. 3.4A). Interestingly, Group 6, although more discordant than those from Group 1, also has an upper intercept around 1.8 Ga (1856±11 Ma) and a lower intercept around 33±99 Ma (Fig. 3.4B). However, there are no points below ~1300 Ma on the Discordia, so the lower intercept is relatively meaningless, as seen in its high standard deviation (±99 Ma).
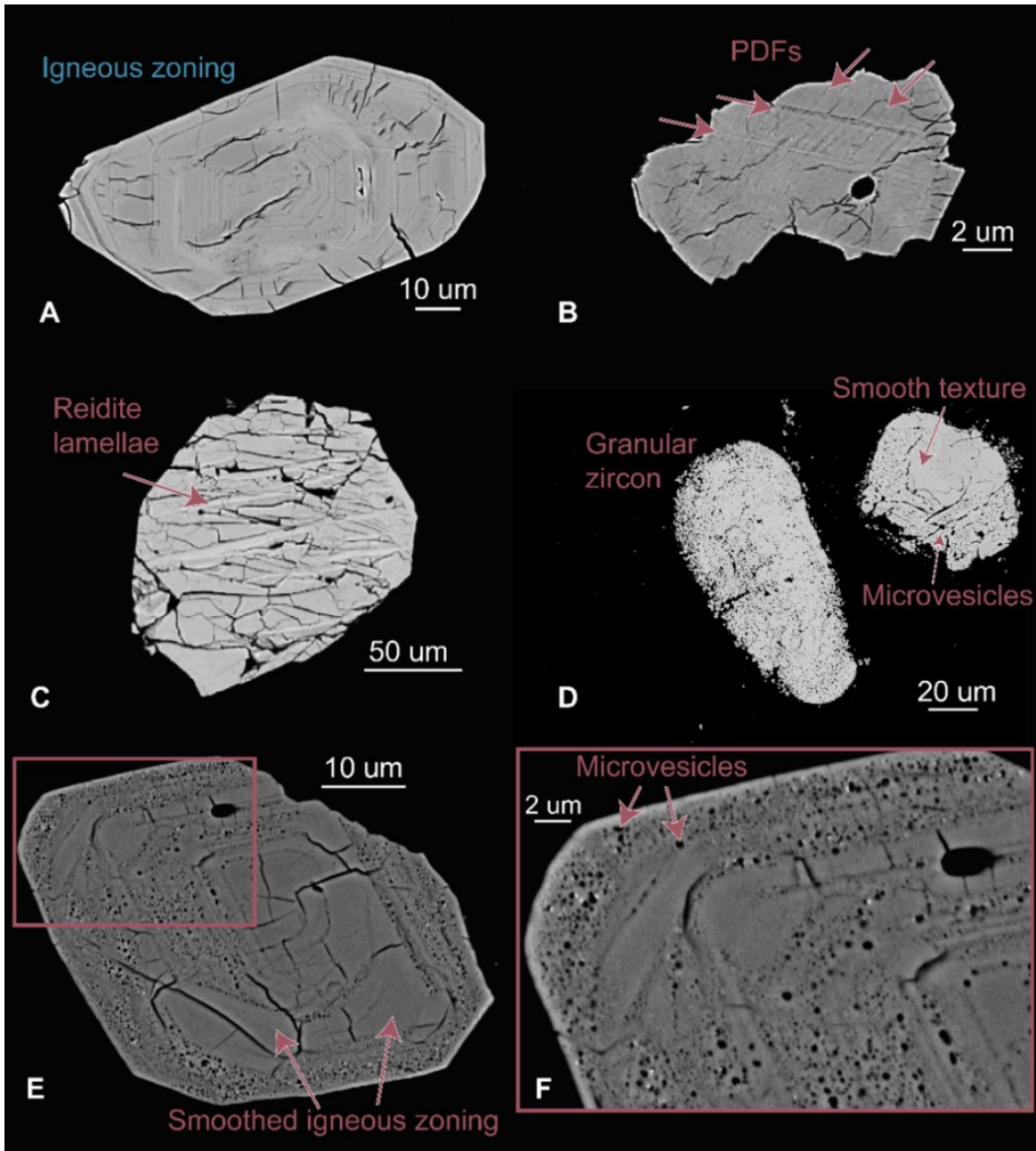
Figure 3. 3. Microstructures in SRIS zircons (in-situ). A) Typical zoning pattern in an igneous zircon. B) Planar deformation features (PDFs) in zircon. Arrows point parallel to two main orientations. C) Reidite lamellae (brighter greyscale) in zircon. D) Granular and smoothing textures, possibly due to recrystallization and/or decomposition in two zircons. E) BSE image of a zircon from 214.3 m depth showing micro-vesicles and smoothed igneous zoning. Red box outlines the location of F on E.
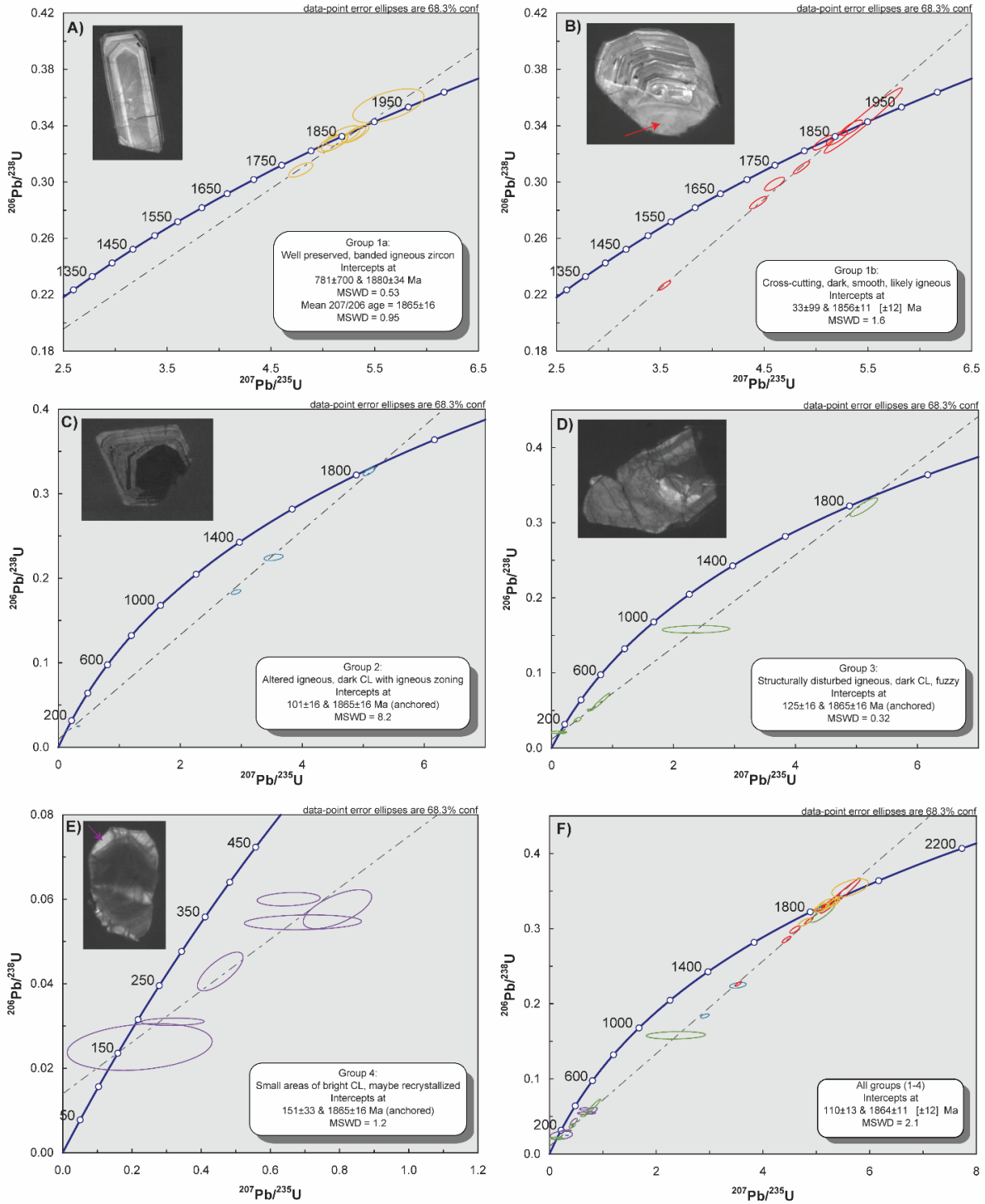
Figure 3. 4. Concordia plots of SRIS zircons; data not filtered for inaccuracies associated with common Pb, extrapolated $^{254}UO^+/^{238}U^+$ ratios, or outlying $^{196}Zr_2O^+$ counts·sec^{-1}·nA^{-1}. A) Group 1a: Zoned igneous zircons. B) Group 1b: Cross-cutting zones on igneous zircons. C) Group 2: Disturbed igneous, dark in CL with relict igneous zoning D) Group 3: Structurally disturbed zircons with "fuzzy" texture, dark in CL. E) Group 4: Small areas of bright CL, typically on grain boundaries. F) All zircon groups. CL=cathodoluminescence, MSWD=mean square weighted deviation.

31

The unexpected age results led to the "Groups" being reclassified into 4 different "Types" (Table 3.1). Group 6 has been reclassified as Type 1b due to its age, and Group 1 is now Type 1a. Group 2 – the disturbed igneous grains with very dark, high U cores – plot closest to the lower intercept. They are reclassified simply as Type 2 zircons, and alone they are highly spread along Discordia. When Types 1a, 1b, and 2 are combined, the Concordia upper intercept is very similar to the igneous mean at 1863±13 Ma, and the lower intercept is better constrained at 101±18 Ma.

The original Group 3, with deformed metamorphic overgrowths (Table 3.1), was grouped in with Type 1b, as it has similar geochemical characteristics. The new Types 3 and 4 (originally Groups 4 and 5) define the lower portion of the Discordia. Type 3 zircons are highly fractured, dark in CL and if any igneous zoning is still visible, it is faint and fuzzy. When anchored at the mean igneous age, the lower intercept is 125±16 Ma (Fig. 3.4D). Type 4 zircons are bright in CL and are often located along grain edges (Table 3.1). They are all young ages with a lower intercept of 151±33 Ma when anchored with the igneous mean (1865±16 Ma; Fig. 3.4E). Combined with Type 3, the intercept is intermediate between the two individual groups at 130±16 Ma.

Four points from Type 3 overlap Concordia near the lower intercept around 121±21 Ma (Fig. 3.5). The weighted mean of these points is 132±1.3 Ma. These four points have very high U and Th concentrations (~1300-5900, and ~550-2300 ppm, respectively). Comparatively, the bright rims on the same grains (Type 4) have much lower U and Th (~200-700, and ~40-400 ppm, respectively), but they plot slightly farther up the Discordia. The bright rims also have higher $^{207}Pb/^{206}Pb$ ages around 1000 Ma. When anchored at the mean igneous age, the lower intercept is 125±16 Ma (Fig. 3.4D). One point from Type 4 overlaps Concordia and the concordant points from Type 3; however, due to its large error ellipse, it was not included in Figure 3.5.

When all unfiltered points from the four zircon types are plotted on Concordia, they form a relatively well-constrained Discordia between 110±13 and 1864±11 Ma (Fig. 3.4F). The upper intercept agrees very closely with the mean igneous age (1865±16 Ma). There is a progression from Type 1a through to Type 4 whereby the points become more discordant (i.e. Types 1a and 1b are near the upper intercept and Type 4 is near the lower).
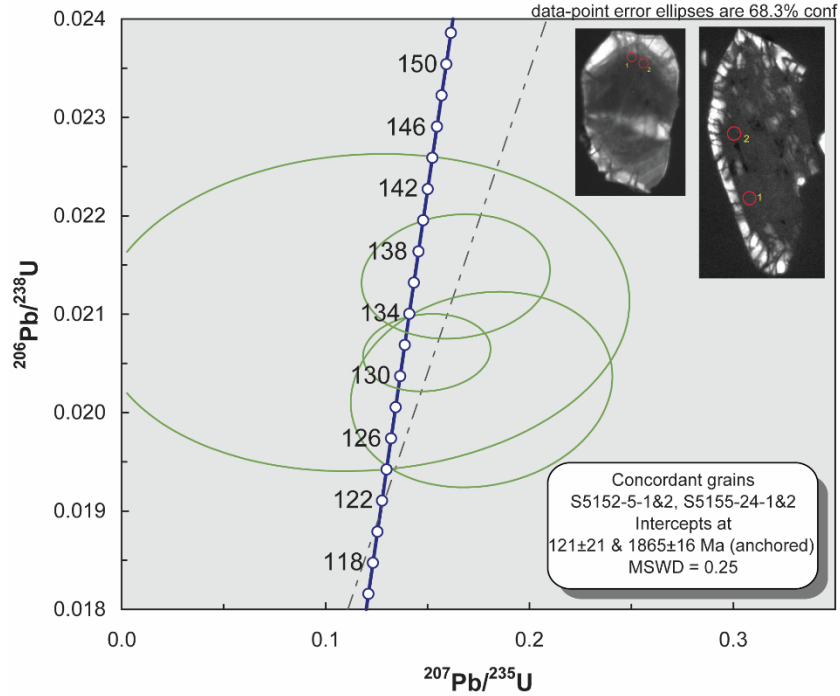
Figure 3. 5. Concordant points at the lower Concordia intercept from Group 3 zircons.

The filtered data, with significant inaccuracies removed, do not differ substantially from the non-filtered data. The lower intercept of all filtered zircons is 123±26 Ma (Fig. 3.6A), with the upper intercept still anchored at the mean igneous age (1865±16 Ma). The igneous and disturbed igneous together (Types 1 and 2), show a Pb-loss trend towards 54±100 Ma (Fig. 3.6B), while the highly disturbed zircons from Types 3 and 4 show an intercept at 134±16 Ma (Fig. 3.6C). Due to the limited number of igneous grains plotting near the lower intercept, these two error envelopes overlap, suggesting that they may share a Pb-loss event.

Trace-elements also vary between the different groups when compared to U concentrations (Fig. 3.7). Th/U ratios are relatively consistent among all the groups, apart from Type 1b which has slightly lower values compared to the other groups. However, the disturbed zircons have higher concentrations of both U and Th than the igneous zircons. The disturbed grains also show a slight enrichment in Yb compared to the igneous grains, while Hf concentrations are relatively consistent (Fig. 3.7). In general, the discrepancies between the igneous and disturbed zircons appear to lie more in the concentration of U than in the other trace elements, with disturbed zircons more enriched in U.
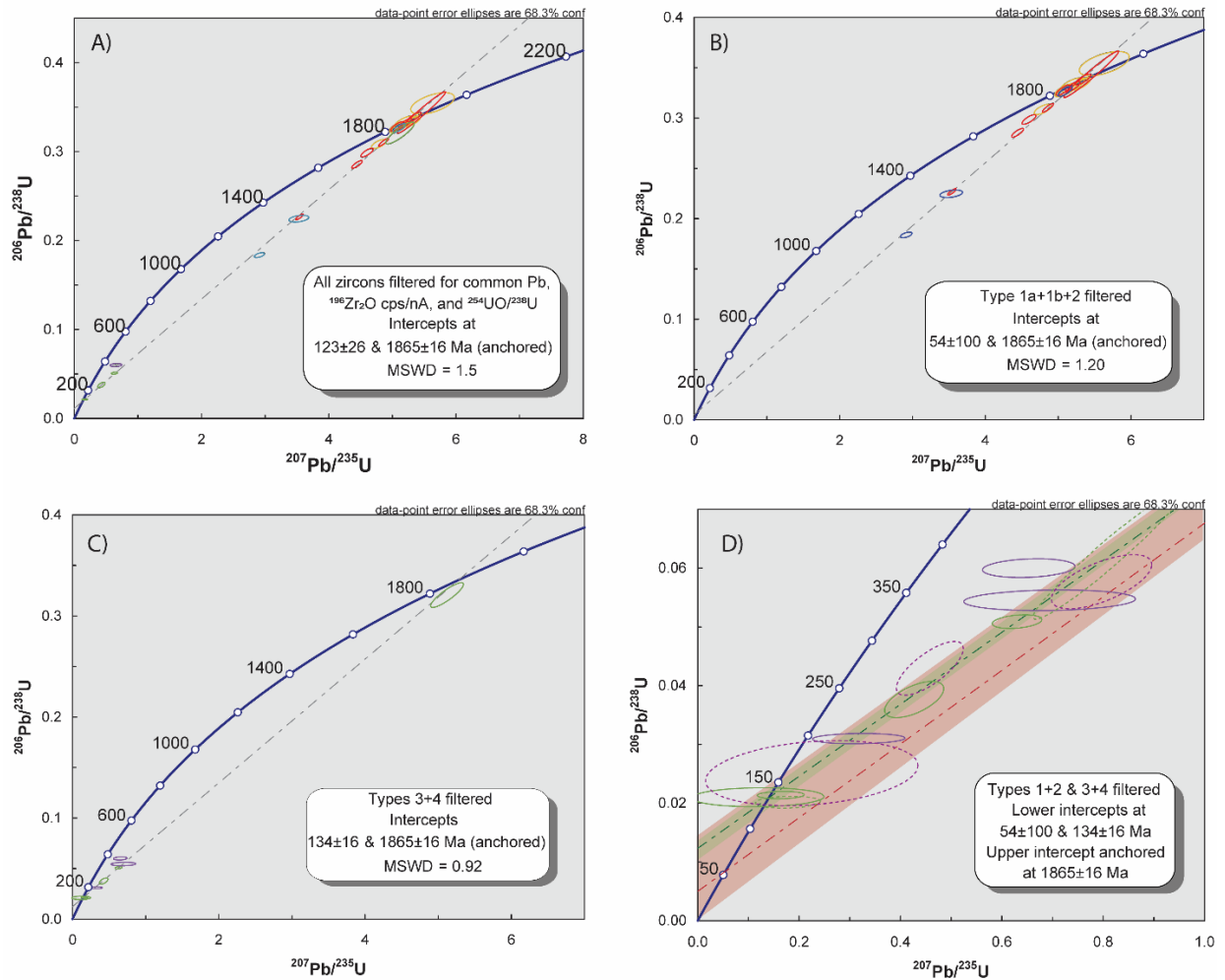
Figure 3. 6. Concordia plots of SRIS zircons once filtered using limits on normalized zirconia peak ($^{196}Zr_2O^+$ counts·second^{-1}·nA^{-1}) and $^{254}UO^+/^{238}U^+$ ratios. A) All zircon points plotted, excluding those filtered out by abnormal $^{196}Zr_2O^+$, $^{254}UO^+/^{238}U^+$ and high common Pb. B) Zircon Types 1a (zoned igneous), 1b (cross-cutting igneous), and 2 (disturbed igneous). C) Zircon Types 3 (dark, fuzzy, disturbed) and 4 (bright rims). D) Magnified portion of A showing the Discordia lines and error envelopes for the metamorphic zircons (Types 3&4, green Discordia) and igneous zircons (Types 1&2, red Discordia); dashed ellipses are removed when inaccuracy filters are applied. MSWD = mean square weighted deviation.
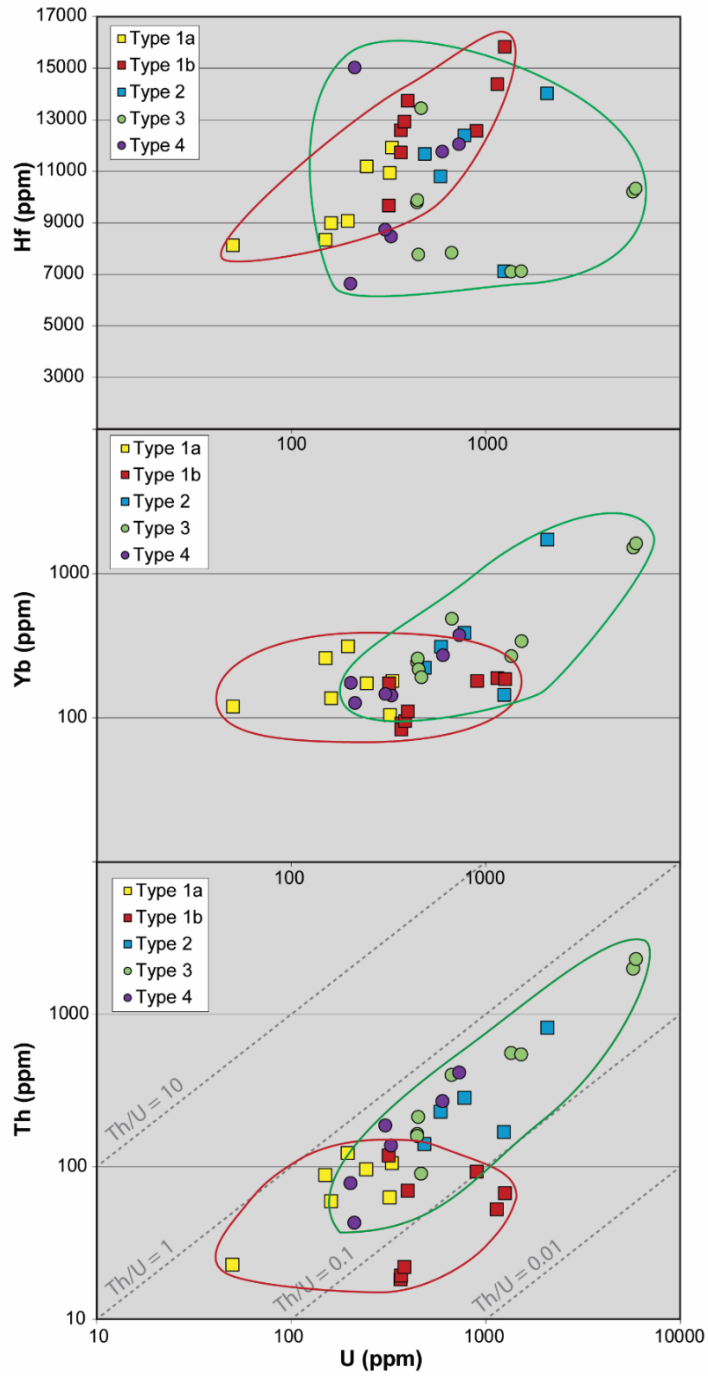
Figure 3. 7. Trace-element plots of Th, Yb, and Hf with respect to U concentration. Red ellipses outline igneous zircons (Types 1a and 1b), while green ellipses outline disturbed zircons (Types 2-4). Squares are igneous (Type 1) and disturbed igneous (Type 2) zircons, while circles are the highly disturbed, possibly reset zircons (Types 3 and 4).

35

3.4 DISCUSSION

3.4.1 ZIRCON TEXTURES

Figure 3.3 provides an overview of textures observed in zircon. The igneous zoning (Fig. 3.3A) is characterized by oscillatory zoning, or growth bands of varying composition (and resulting grey-scale variation in BSE) that form when the zircon crystallizes slowly in the parent magma over periods of changing magma composition. This zoning is useful in discriminating igneous zircons unaffected by shock from those that may have been shock metamorphosed. Granular zircon consists of small grains, only a few microns in size, that together form the rough shape of the original grain (Fig. 3.3D). This texture may form through annealing of previously dissociated zircon (Wittmann et al., 2006), or when reidite reverts back to zircon during cooling (Cavosie et al., 2016) although its exact formation mechanism is still debated. It is most common in zircon grains that were metamict prior to the impact, and therefore contained a high abundance of defects that acted as nucleation sites (Timms et al., 2017). In the SRIS, decomposition textures (>1673°C) typically consist of a bright rim of baddeleyite and silica-glass on a shocked zircon grain (Walton et al., 2018), although it is possible that an entire grain can decompose and then anneal to form a granular texture similar to that in Fig. 3.3D.

Another bright feature in these zircon grains are the reidite lamellae (Fig. 3.3C), which may also form a granular texture (Cavosie et al., 2016; Timms et al., 2017). This high-pressure polymorph of zircon implies that these grains reached pressures greater than ~20-30 GPa (Timms et al., 2017; Erickson et al., 2017; and references therein). The smoothing or erasing of igneous zoning observed in the SRIS zircons (Fig. 3.3D-F) is also seen in zircons from the Haughton impact structure, where it is attributed to near-melting conditions (Singleton et al., 2015). The microvesicles, or microporous textures in these grains suggest that a gas may have been released from the crystal structure as the grain neared its melting temperature (e.g. Wittmann et al., 2006).

3.4.2 ZIRCON GEOCHEMISTRY

Typically, U is higher in younger, newly-formed zircons as it does not have sufficient time to decay to Pb. However, some igneous zircons may be exceptionally rich in U when they initially form due to high concentrations in the parent magma. In general, when combined with Th, U can aid in discerning original, igneous zircons from those affected by metamorphism. The Th/U ratios

tend to be higher in igneous grains (typically >0.5) and lower in metamorphosed grains (Kirkland et al., 2015). Th/U ratios in the SRIS zircons are consistent among all defined groups between 0.1-1; however, within Type 1b zircons, the smooth, cross-cutting areas on otherwise igneous grains show reduced values (<0.1). This suggests that Type 1b may represent a metamorphic event that followed shortly after crystallization of the igneous parent body, as they have a similar age around 1.86 Ga. On the other hand, if these features were originally igneous, then perhaps they were enriched in U or were more susceptible to, and later affected by, Th-loss.

Hf concentrations will be higher in overgrowths that are younger than the parent grain, because radiogenic production of Hf only occurs outside zircons and is later incorporated and "locked in" during recrystallization (Gerdes and Zeh, 2009). In SRIS zircons, Hf is relatively consistent between the four groups with a slight depletion in the disturbed grains. Collection of more points, with greater precision of the Hf concentrations, may clarify any differences between the igneous and disturbed grains – if the values are indeed the same, then they may have formed during the same growth event and if different, then the disturbed grains formed later (Gerdes and Zeh, 2009).

Loss of Pb during an event can result in age-resetting and allow researchers to date the time of resetting. At lower temperatures (< 900ºC; Cherniak and Watson, 2000), Pb-loss may occur by diffusion through mechanisms such as crystal plastic deformation (Reddy et al., 2006). At higher temperatures, especially in metamict zircons damaged by radiation (Cherniak et al., 1991), recrystallization may occur, which favors "pure" zircon ($ZrSiO_4$) and trace elements such as Pb are lost. However, it must be noted that if the high temperatures of the impact environment also induced annealing, then the age obtained from these zircons could represent the time at which annealing prevented further Pb-loss (Schoene, 2014). This could result in a slightly different age from the impact event, but as impact-generated heat may be sustained for thousands of years (Deutsch and Langenhorst, 2007), the annealing would have been a long, slow process during which Pb-loss could have continued (Cherniak et al., 1991). Annealing, or reorganization of the crystal lattice, is thought to occur where highly contrasting U, Th, and trace element abundances between growth zones place strain on the lattice (Schaltegger et al., 1999). Strongly disparate zones of U abundance are observed in the SRIS zircons that are concordant near the lower intercept; therefore, it is possible that they experienced annealing and Pb-loss because of impact-generated

metamorphism. One other source of error that needs to be considered is non-radiogenic, or common lead. If common Pb (^{204}Pb, ^{206}Pb, ^{207}Pb, and/or ^{208}Pb) infiltrates the zircon, it can induce higher errors in the data as opposed to grains that are free of these isotopes. This is monitored by analysis of ^{204}Pb, which is not affected by radiogenic growth; however, there is the assumption that this isotope reflects the total amount of common Pb present.

3.4.3 A VIABLE IMPACT AGE?

3.4.3.1 U-PB GEOCHRONOLOGY

The upper intercept of the data has a mean age of 1865±16 Ma, which falls within the known age range of the underlying Great Bear Magmatic Arc (1875-1840 Ma; Hildebrand et al., 1987). The analyzed granite samples were collected from the bottom of ST003; therefore, the central uplift is comprised of Great Bear rocks. The smooth areas that cross-cut the zoned igneous zircons (Type 1b) are interpreted to form through recrystallization (e.g. Corfu et al., 2003), which differs from annealing because it is a physical change to a new crystallographic phase (Schaltegger et al., 1999). Contrary to initial expectations, these features in the SRIS zircons have an age similar to the zoned, igneous areas (~1.86 Ga). This suggests that they are either primary crystallization features from the parent magma, or the effects of a metamorphic event shortly after crystallization. Their age is nearly indistinguishable from that of the Type 1a igneous zircons, so it is difficult to say exactly what created the cross-cutting features.

Zircons from Types 2-4 that plot closest to the lower intercept have high concentrations of U (>1200 ppm) in their cores, with low U (<800 ppm) rims. Three possible explanations exist for the origin of these grains:

1) Unusually high U in the youngest, concordant grains is relict from disturbed igneous zircons (Type 2) that were originally high in U before the impact but were more susceptible to Pb-loss due to the metamictization and radiation damage (Cherniak et al., 1991). This is supported by the relatively homogeneous grain interiors in Type 3 zircons that lack igneous zoning, often caused by diffusion of Pb (Connelly, 2001). The bright rims (Type 4) are recrystallized zircon, potentially formed during the impact. Recrystallization, especially during high temperature events on metamict zircons, results in Pb-loss from the mineral

structure. It may also result in U and Th loss, and a "purer" zircon, so if the bright rims did experience recrystallization, this could explain the low ppm U observed (Connelly, 2001).

2) Annealing of the zircons following impact was slow enough to result in Pb-loss. The U-rich core and U-poor rim of the grain are relict of igneous zoning, again similar to Type 2 zircons, and this stark difference in U concentrations strained the crystal lattice, making it more susceptible to annealing.

3) Hydrothermal activity altered the edges of the originally igneous zircons. Hydrothermal reaction rims depleted in U and Th have been observed previously in metamict zircon (Geisler et al., 2002). If this is the case, then U, Th, and Pb were mobilized by hydrothermal activity and post-impact heated fluids, which would give an age slightly younger than the impact event. Evidence for the hydrothermal system at the SRIS is discussed in Chapter 2.

Therefore, two main possibilities may explain the data as a whole: 1) the impact did not affect the U-Pb system and simply resulted in annealing of some grains; in this case, the Pb-loss is secondary and may be hydrothermal or caused by another process. Or 2) the impact did have a significant effect on the U-Pb system and is the main cause of the Pb-loss event. The filtered Discordia given by the igneous (Types 1a,b) and disturbed igneous grains (Type 2) has a lower intercept of 54±100 Ma (Fig. 3.6B). This may be showing a later Pb-loss event than the actual impact, although even when filtered for inaccuracies, it overlaps within error with the Discordia from the Type 3 and 4 zircons, which intercept Concordia at 134±16 Ma (Fig. 3.6D).

The textures observed in this study are similar to those described from other impact structures (e.g. Wittmann et al., 2006). For example, the presence of microvesicles (Fig. 3.3), nearly identical to microvesicles observed in zircons from Popigai and Chicxulub, suggests that a gas may have been released during partial melting or amorphization of the zircon grains (Wittmann et al., 2006). Therefore, the impact affected SRIS zircons to varying degrees and it could be expected that Pb-loss would have occurred as a result. However, the data from this study show the opposite from this expectation – the grains that are the most concordant (lower intercept) have the highest common Pb.

Walton et al. (2017) observe decomposition textures in zircon and calculate an average deposition temperature for the SRIS impactites to be 796ºC. Decomposition textures are observed as rims of sub-micron baddeleyite and silica on zircon grains entrained within clasts of impact melt

in the impact breccia. The melted material would have experienced much higher initial temperatures than the surrounding groundmass, which explains the presence of these highly shocked textures in melt-entrained zircon. Both recrystallization and decomposition textures are observed in the SRIS zircons, which indicate pressures >50 GPa and temperatures of >1100ºC and 1673ºC, respectively. As mentioned above, recrystallized zircon is a good candidate for dating impact structures. Perhaps the limited sample size and precision of the SIMS analyses restrict the effectiveness of dating these features. Due to the sub-micron size of the zircon granules, the ion beam is not small enough to encompass individual granules; therefore, measurements of these grains will include both the zircon and surrounding amorphous phase, which is Si-rich and may contain common Pb.
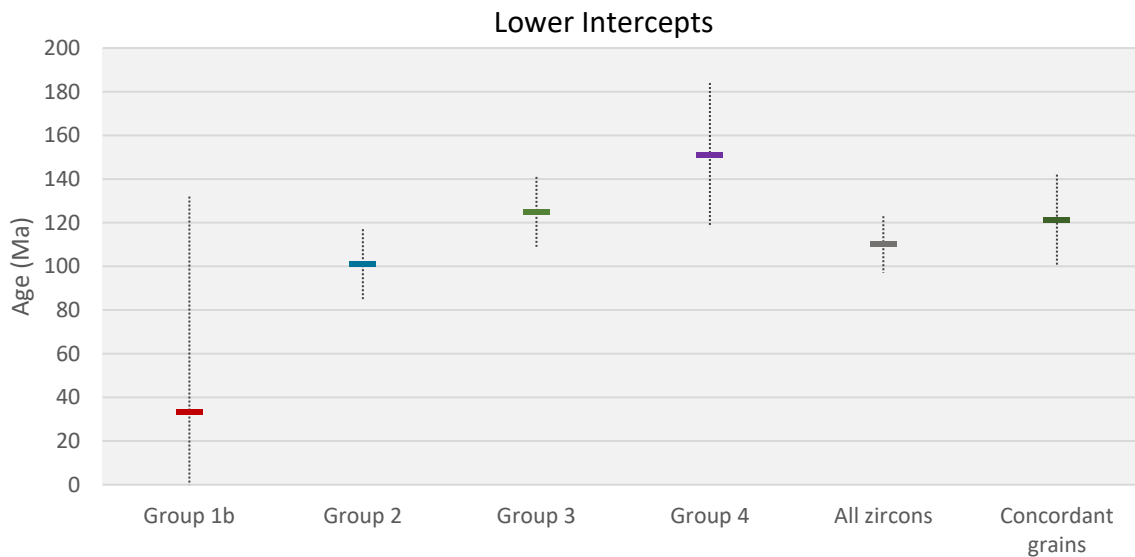
Figure 3. 8. Plot of mean lower intercept ages with error bars from each of the zircon groups. Thick bar plots at the mean of each group and dashed lines show associated error.

These results may show the effects of both scenarios, whereby the impact caused some resetting and the following hydrothermal activity, discussed in detail in Chapter 2, caused further Pb-loss. In this case, the impact would be represented by the Type 3 concordant points and the hydrothermal resetting, or some other event (i.e. Cordillera/Rocky Mountain building) occurred <100 Ma as represented by Types 1b and 2. Due to the overlap of these errors, it cannot be definitively concluded that the lower intercept age represents the time of the impact; instead, it may provide an approximation of the age or act as a guideline for further, more detailed studies.

In summary, 4 main zircon groups can be defined, each with distinct characteristics and ages; however, the lower intercepts of each overlap around 120 Ma (Fig. 3.8). In addition, the 4 concordant points, when anchored by the igneous upper intercept, have a lower intercept of 121±21 Ma and a mean age of 132±1.3 Ma. As discussed in the following section, this also falls within the stratigraphic age constraints, and therefore it likely represents the best inferred age for the structure from these data.

3.4.3.2 STRATIGRAPHIC CONSTRAINTS

Additional constraints on the timing of the SRIS event can be obtained from stratigraphic considerations. As noted above, the surrounding stratigraphy associated with the SRIS is at odds with the current published impact age. The only prior geochronology applied to SRIS impactites was collected using K-Ar dating on a plutonic igneous rock, which found an age of ~560 Ma; the same method, along with Rb-Sr dating, on a whole-rock pyroclastic sample gave an age of ~95 Ma (Carrigy and Short, 1968). The errors are not included in the original study, but Grieve (2006) recalculated the age of the SRIS to be 91±7 Ma, using the decay constants of Steiger and Jager (1977). Since then, minimal work has been done to constrain an age for the SRIS; however, studying the surrounding stratigraphy shows this age to be erroneous.

The upper Loon River formation, which sits more than 100 m above the SRIS crater-fill material, has been dated using U-Pb, $^{40}Ar/^{39}Ar$, and foraminifera to be ~108 Ma (Hathway et al., 2013). In addition, Molak et al. (2001) logged the Shaftesbury Formation as overlying the SRIS. This Formation contains a distinct Fish Scale Unit (Alberta Geological Survey, 2015), which has been dated at 101 Ma. These overlying stratigraphic ages imply that the SRIS is older than currently suggested by at least 17 Ma, and suggest that the published age from Carrigy and Short (1968) might be dating post-impact hydrothermal activity that is unrelated to the impact event.

A constraint on the maximum age for the structure comes from the Bullhead Group, which consists of the Cadomin and Gething Formations. The well-known and distinct conglomerate of the Cadomin, dated as forming sometime in the Berriasian-Aptian between ~145 and ~113 Ma (Wrote and Leckie, 1999), forms the base of the Bullhead Group. In NW Alberta, it is overlain by sandstones of the Lower Cretaceous Gething and Bluesky Formations. These formations have a Hauterivian-Albian age of ~108-133 Ma (Stott, 1971; Alberta Geological Survey, 2015; Currie et al., 1991; Gibson, 1985). Beneath the Cretaceous units in the WCSB, there is a sub-Cretaceous

41

unconformity that is overlain by the Cadomin, Gething, Bluesky, Ellerslie, or McMurray Formations, depending on location (Hubbard et al., 1999; Hayes et al., 1994). This unconformity is sometimes referred to as the Sub-Mannville unconformity and it represents a period of decreased deposition and elevated erosion rates. The unconformity sub-crops on units ranging from the Cambrian through to the Jurassic; though at the locality of the SRIS, it overlies Devonian sediments (Hayes et al., 1994).

Molak et al. (2001) logged the shale and minor sandstone that overly the SRIS impact breccia to be the Loon River and Bluesky Formations, respectively. Therefore, the impact event must be older than 108 Ma. In addition, neither the Gething, nor the distinct conglomerate of the Cadomin Formation has not been logged as overlying the SRIS in any of the cores; therefore, if these Formations are present at the locality of the SRIS, then the impact must be younger than ~145-113 Ma. This constraint is supported by results from the U-Pb analysis (~132±1.3 Ma). If the Bullhead was erroneously logged in this area, then the maximum stratigraphic age constraint is the Devonian Wabamun Group (~370-360 Ma).

3.5 CONCLUSIONS

This geochemical and geochronological study of zircons from the SRIS aimed to provide tighter constraints on this age to better correlate it with the surrounding stratigraphy and paleoecology. When filtered for inaccuracies, isolated zircons fall along a Discordia stretching between 123±26 Ma and a mean, anchored igneous age of 1865±16 Ma. Most of the grains have clearly experienced Pb-loss, although the exact cause cannot be confirmed without further data and higher-precision analyses. Based on stratigraphic age constraints, the structure is older than the currently published age of 91±7 Ma (Carrigy and Short, 1968) and falls between 108-145 Ma. The most likely age from the U-Pb data is that of concordant points near the lower Discordia intercept, which falls within the acceptable stratigraphic range at 132±1.3 Ma.

CHAPTER 4:
CONCLUSIONS

4.1 THESIS SUMMARY

These two thesis projects are part of a broader effort to understand the Steen River impact structure (SRIS). Located in NW Alberta, Canada, the SRIS is a buried complex crater that contains a central uplift, overlain by ~150 m of polymict impact breccia. Until 2015, the only published literature on the SRIS consisted of two papers (Carrigy and Short, 1968; Winzer, 1972), along with a handful of industry reports. As a result, our studies have contributed greatly to characterization of the structure and its associated impactites. Impact breccia with a similar appearance to that at the SRIS has been described at numerous other craters; however, the emplacement mechanism is still a topic of debate in the literature. Additionally, the age of the SRIS is uncertain, as the currently published age is from a whole-rock sample, using an isotopic system that is easily reset. This age also contradicts the surrounding stratigraphy. As such, the two main thesis objectives were to 1) use hyperspectral imaging to create detailed mineral maps of three drill cores and strengthen the model of breccia formation at the SRIS, and 2) constrain the age of the impact event through U-Pb geochronology of zircons.

4.1.1 CHAPTER 2 – HYPERSPECTRAL SCANNING

Three cores from the SRIS that penetrate the impact breccia were imaged using three separate wavelength regions, from visible to thermal infrared. Cores ST001 and ST002 are located in the annular trough of the structure, while core ST003 penetrates the side of the central uplift – together, these cores provide a representative cross-section through the upper-most portion of the SRIS crater-fill. The resulting hyperspectral images highlight the presence of hydrothermal mineralization in the three cores and identify new ammoniated species that have not been previously observed in the SRIS or other impact structures. The mineral maps also enhance previous descriptions of large-scale layering present in the impact breccias. This suggests that the breccia did not experience significant post-depositional disruption, such as explosive interaction between hot melt and cool meteoric water (Artemieva et al., 2013). Instead, the results emphasize the role that sedimentary volatiles likely played early in breccia formation as the propagating shockwave caused heating and pore-collapse.

4.1.2 CHAPTER 3 – CONSTRAINING AN AGE

The only published age for the SRIS is a K-Ar whole-rock analysis of pyroclastic material from Carrigy and Short (1968) that places the impact event at 91±7 Ma. However, not only have dating methods improved in the last five decades, but the K-Ar system is susceptible to hydrothermal resetting – evidence of hydrothermal activity is described in Chapter 2. In addition, the overlying stratigraphy has been dated at >100 Ma, implying that the published age is incorrect and the SRIS is older than previously thought. Zircon grains were separated from impact melt and granite clasts and their U-Pb concentrations were measured using secondary ion mass spectrometry (SIMS). Based on textural and geochemical characteristics, four zircon types were defined. Type 1 represents igneous grains and associated overgrowths that have an age within error of the known Proterozoic basement rocks underlying the SRIS. Types 2-4 consist of progressively higher disturbance in the zircons, forming a Discordia that stretches from an upper, Proterozoic intercept (1865±16 Ma) down to a lower intercept of 123±26 Ma. Four grains overlap with Concordia at the lower intercept, defining a ^{238}U-^{206}Pb weighted mean age of 132±1.3 Ma. It is possible that this age is associated with the impact event, although due to the small sample size and lack of recrystallization features large enough to date using the SIMS technique, this age overlaps with modern Pb-loss from the same parent zircons.

4.2 FUTURE RESEARCH

The hyperspectral mineral maps could be improved by higher resolution or targeted spot scans to improve the resolution of the endmember spectra. Due to the fine grain size of the impact breccia groundmass (<0.5 mm), many of the extracted endmembers were mixtures of more than one mineral (e.g. feldspars, clay minerals, and pyroxene). Based on the maps made in this project, and visual inspection of the core, areas of the core with mixtures or pure endmembers could be targeted with higher resolution scans or hand-held spectrometers. This may reduce the heterogeneity and noise in individual spectra and improve mineral classification. Furthermore, hyperspectral scanning can, and should, be applied to other cores from impact structures for rapid classification to aid further, more detailed studies. Impact studies tend to focus on individual clasts, minerals, or samples within impact breccia cores, or resort to hand-logging the core. By utilizing hyperspectral scanning, logging of the core could become more efficient and cores from different craters could be more easily compared.

With respect to constraining an age for the SRIS, additional cores from the Western Canadian Sedimentary Basin (WCSB) in the locality of the structure may contain evidence of an ejecta blanket, which could provide additional stratigraphic constraints on the age. If preserved within the surrounding stratigraphy, ejecta would appear similar to a volcanic tuff or ash deposit but can be distinguished by the presence of shock features in constituent minerals, distinct geochemistry, or spherules (French, 1998). Indeed, Carrigy and Short (1968) note the presence of, what they describe as, "tuff" layers in well I.O.E. Steen 16-19, although whether these are volcanic, or related to the SRIS-forming impact event, is not clear and would require detailed petrographic and/or geochemical observations. Another possible correlation may be an abrupt change in, or local destruction of, flora and fauna which would be recorded as a fossil bed around the time of the impact. No such evidence has yet been reported; though, to our knowledge, no such studies have been conducted in the WCSB that examine a link between impact and extinction events.

To strengthen the absolute age of the SRIS, thermal ionization mass spectrometry (TIMS) could be used to target specific features on zircons. The smooth features that cross-cut igneous zoning give Proterozoic igneous or metamorphic ages, suggesting that further points from these areas would not be useful in constraining the impact age. Instead, if more points could be collected from the metamict igneous grains with dark CL cores, it may aid it strengthening the Discordia. Additional spots from other zircons with the "fuzzy" texture, or larger granules (>1-5 µm) of recrystallized zircon would provide better constraints on the lower intercept. The metamict igneous grains appear to be precursors to the "fuzzy" igneous grains that give a lower intercept age, due to their susceptibility for Pb-loss. TIMS has higher precision relative to SIMS and laser ablation inductively coupled plasma mass spectrometry (LA-ICPMS) (Schoene, 2014); therefore, if known shock features can be extracted using a micromill, and then analyzed individually, it would likely improve and expand upon the SIMS results from the current study.

REFERENCES

Aberg, G., and Bollmark, B., 1985, Retention of U and Pb in zircons from shocked granite in the Siljan impact structure, Sweden. Earth and Planetary Science Letters, v. 74, p. 347–349, doi: 10.1016/S0012-821X(85)80006-6.

Alberta Geological Survey, 2015, Alberta Table of Formations. Alberta Energy Regulator, https://www.aer.ca/documents/catalog/TOF.pdf. (accessed April 2016).

Alwmark, C., Bleeker, W., LeCheminant, A., Page, L., and Scherstén, A., 2017, An Early Ordovician 40Ar-39Ar age for the ~50 km Carswell impact structure, Canada. GSA Bulletin, v. 129, p. 1442–1449, doi: 10.1130/B31666.1.

Artemieva, N.A., Wünnemann, K., Krien, F., Reimold, W.U., and Stöffler, D., 2013, Ries crater and suevite revisited-Observations and modeling Part II: Modeling. Meteoritics and Planetary Science, v. 48, p. 590–627, doi: 10.1111/maps.12085.

Asphaug, E., 2014, Impact Origin of the Moon? Annual Review of Earth and Planetary Sciences, v. 42, p. 551–578, doi: 10.1146/annurev-earth-050212-124057.

Baldridge, A.M., Hook, S.J., Grove, C.I., and Rivera, G., 2009, The ASTER spectral library version 2.0: Remote Sensing of Environment, v. 113, p. 711–715, doi: 10.1016/J.RSE.2008.11.007.

Barringer, D.M., 1905, Coon Mountain and Its Crater. Proceedings of the Academy of Natural Sciences of Philadelphia, v. 57, p. 861–886, doi: 10.2307/4063062.

Baugh, W.M., Kruse, F.A., and Atkinson, W.W., 1998, Quantitative Geochemical Mapping of Ammonium Minerals in the Southern Cedar Mountains, Nevada, Using the Airborne Visible/Infrared Imaging Spectrometer (AVIRIS). Remote Sensing of Environment, v. 65, p. 292–308, doi: 10.1016/S0034-4257(98)00039-X.

Berg, B.L., Cloutis, E.A., Beck, P., Vernazza, P., Bishop, J.L., Takir, D., Reddy, V., Applin, D., and Mann, P., 2016, Reflectance spectroscopy (0.35–8 μm) of ammonium-bearing minerals and qualitative comparison to Ceres-like asteroids. Icarus, v. 265, p. 218–237, doi: 10.1016/J.ICARUS.2015.10.028.

Bird Geophysical, 1999, Report: Aeromagnetic Modeling Interpretation over the Steen River Structure, Northwest Alberta. Alberta Energy and Utilities Board, Industrial and Metallic Mineral Assessment Report 19990022.

Bischoff, A., and Stöffler, D., 1992, Shock metamorphism as a fundamental process in the evolution of planetary bodies: Information from meteorites. European journal of mineralogy, v. 4, p. 707–755.

Bishop, J.., Banin, A., Mancinelli, R.., and Klovstad, M.., 2002, Detection of soluble and fixed NH4+ in clay minerals by DTA and IR reflectance spectroscopy: a potential tool for planetary surface exploration. Planetary and Space Science, v. 50, p. 11–19, doi: 10.1016/S0032-0633(01)00077-0.

Boamah, D., and Koeberl, C., 2006, Petrographic studies of "fallout" suevite from outside the Bosumtwi impact structure, Ghana. Meteoritics & Planetary Science, v. 41, p. 1761–1774, doi: 10.1111/j.1945-5100.2006.tb00450.x.

Bottomley, R., Grieve, R.A.F., York, D., and Masaitis, V., 1997, The age of the Popigai impact event and its relation to events at the Eocene/Oligocene boundary. Nature, v. 388, p. 365–368, doi: 10.1038/41073.

Brown, J.M.L., 1994, Report on Stream Sediment Geochemical Exploration - Steen River Alberta.

Brusatte, S.L., Butler, R.J., Barrett, P.M., Carrano, M.T., Evans, D.C., Lloyd, G.T., Mannion, P.D., Norell, M.A., Peppe, D.J., Upchurch, P., and Williamson, T.E., 2015, The extinction of the dinosaurs. Biological Reviews, v. 90, p. 628–642, doi: 10.1111/brv.12128.

Cameron, A.G.W., and Ward, W.R., 1976, The Origin of the Moon: Lunar and Planetary Science Conference. Vol. 7.

Carrigy, M.A., and Short, N.M., 1968, Evidence of shock metamorphism in rocks from the Steen River Structure, Alberta, *in* French, B.M. and Short, N.M. eds., Shock Metamorphism of Natural Materials, Baltimore, MD,

Mono Book Corp., p. 367–378.

Cavosie, A.J., Erickson, T.M., Timms, N.E., Reddy, S.M., Talavera, C., Montalvo, S.D., Pincus, M.R., Gibbon, R.J., and Moser, D., 2015, A terrestrial perspective on using ex situ shocked zircons to date lunar impacts. Geology, v. 43, p. 999–1002, doi: 10.1130/G37059.1.

Cavosie, A.J., Timms, N.E., Erickson, T.M., Hagerty, J.J., and Hörz, F., 2016, Transformations to granular zircon revealed: Twinning, reidite, and ZrO_2 in shocked zircon from Meteor Crater (Arizona, USA). Geology, v. 44, p. 703–706, doi: 10.1130/G38043.1.

Cherniak, D.J., Lanford, W.A., and Ryerson, F.J., 1991, Lead diffusion in apatite and zircon using ion implantation and Rutherford Backscattering techniques. Geochimica et Cosmochimica Acta, v. 55, p. 1663–1673, doi: 10.1016/0016-7037(91)90137-T.

Cherniak, D.J., and Watson, E.B., 2000, Pb diffusion in zircon. Chemical Geology, v. 172, p. 5–24, doi: 10.1016/S0009-2541(00)00233-3.

Claeys, P., Heuschkel, S., Lounejeva-Baturina, E., Sanchez-Rubio, G., and Stöffler, D., 2003, The suevite of drill hole Yucatàn 6 in the Chicxulub impact crater. Meteoritics & Planetary Science, v. 38, p. 1299–1317, doi: 10.1111/j.1945-5100.2003.tb00315.x.

Clark, R.N., Swayze, G.A., Wise, R., Livo, K.E., Kokaly, R.F., and Sutley, S.J., 2007, USGS digital spectral library splib06a: U.S. Geological Survery, Digital Data Series 231, doi: 10.1029/2002JE001847.

Cockell, C.S., and Lee, P., 2002, The biology of impact craters – a review. Biological Reviews of the Cambridge Philosophical Society, v. 77, p. 279–310, doi: 10.1017/S146479310100584X.

Connelly, J.N., 2001, Degree of preservation of igneous zonation in zircon as a signpost for concordancy in U/Pb geochronology. Chemical Geology, v. 172, p. 25–39, doi: 10.1016/S0009-2541(00)00234-5.

Corfu, F., Hanchar, J.M., Hoskin, P.W.O., and Kinny, P., 2003, Atlas of Zircon Textures. Reviews in Mineralogy and Geochemistry, v. 53, p. 469–500, doi: 10.2113/0530469.

Currie, P.J., Nadon, G.C., and Lockley, M.G., 1991, Dinosaur footprints with skin impressions from the Cretaceous of Alberta and Colorado. Canadian Journal of Earth Sciences, v. 28, p. 102–115, doi: 10.1139/e91-009.

Dence, M.R., 1973, Dimensional Analysis of Impact Structures. Meteoritics, v. 8, p. 343–344.

Dence, M.R., 1971, Impact Melts. Journal of Geophysical Research, v. 76, p. 5552–5565.

Deutsch, A., Grieve, R.A.F., Avermann, M., Bischoff, L., Brockmeyer, P., Buhl, D., Lakomy, R., Müller-Mohr, V., Ostermann, M., and Stöffler, D., 1995, The Sudbury Structure (Ontario, Canada): a tectonically deformed multi-ring impact basin. Geologische Rundschau, v. 84, p. 697–709, doi: 10.1007/BF00240561.

Deutsch, A., and Langenhorst, F., 2007, On the fate of carbonates and anhydrite in impact processes – evidence from the Chicxulub event. GFF, v. 129, p. 155–160, doi: 10.1080/11035890701292155.

von Engelhardt, W., and Graup, G., 1984, Suevite of the ries crater, Germany: Source rocks and implications for cratering mechanics. Geologische Rundschau, v. 73, p. 447–481, doi: 10.1007/BF01824968.

Erickson, T.M., Pearce, M.A., Reddy, S.M., Timms, N.E., Cavosie, A.J., Bourdet, J., Rickard, W.D.A., and Nemchin, A.A., 2017, Microstructural constraints on the mechanisms of the transformation to reidite in naturally shocked zircon. Contributions to Mineralogy and Petrology, v. 172, p. 1–26, doi: 10.1007/s00410-016-1322-0.

Ferrière, L., and Osinski, G.R., 2013, Shock Metamorphism, *in* Impact Cratering, Chichester, UK, John Wiley & Sons, Ltd, p. 106–124, doi: 10.1002/9781118447307.ch8.

French, B.M., 1998, Traces of Catastrophe: A Handbook of Shock-Metamorphic Effects in Terrestrial Meteorite Impact Structures. Houston, Lunar and Planetary Institute, 120 p.

Geisler, T., Pidgeon, R.T., van Bronswijk, W., and Kurtz, R., 2002, Transport of uranium, thorium, and lead in metamict zircon under low-temperature hydrothermal conditions. Chemical Geology, v. 191, p. 141–154, doi:

10.1016/S0009-2541(02)00153-5.

Gerdes, A., and Zeh, A., 2009, Zircon formation versus zircon alteration — New insights from combined U–Pb and Lu–Hf in-situ LA-ICP-MS analyses, and consequences for the interpretation of Archean zircon from the Central Zone of the Limpopo Belt. Chemical Geology, v. 261, p. 230–243, doi: 10.1016/J.chemgeo.2008.03.005.

Germundson, R.K., and Fischer, P.A., 1978, Steen River Diamond Drill Program, Alberta, NTS 84N; Alberta Energy and Utilities Board, Industrial and Metallic Mineral Assessment Report 19780015.

Gibson, D.W., 1985, Stratigraphy and sedimentology of the lower Cretaceous Gething formation, Carbon Creek coal basin, northeastern British Columbia: Ottawa, Canada, Geological Survey of Canada, 29 p.

Gibson, R.L., Armstrong, R.A., and Reimold, W.U., 1997, The age and thermal evolution of the Vredefort impact structure: A single-grain U-Pb zircon study. Geochimica et Cosmochimica Acta, v. 61, p. 1531–1540, doi: 10.1016/S0016-7037(97)00013-6.

Glass, B.P., and Liu, S., 2001, Discovery of high-pressure ZrSiO4 polymorph in naturally occurring shock-metamorphosed zircons. Geology, v. 29, p. 371–373, doi: 10.1130/0091-7613(2001)029<0371:DOHPZP>2.0.CO;2.

Gomes, R., Levison, H.F., Tsiganis, K., and Morbidelli, A., 2005, Origin of the cataclysmic Late Heavy Bombardment period of the terrestrial planets. Nature, v. 435, p. 466–9, doi: 10.1038/nature03676.

El Goresy, A., 1965, Baddeleyite and its significance in impact glasses. Journal of Geophysical Research, v. 70, p. 3453–3456, doi: 10.1029/JZ070i014p03453.

Greenberger, R.N., Mustard, J.F., Ehlmann, B.L., Blaney, D.L., Cloutis, E.A., Wilson, J.H., Green, R.O., and Fraeman, A.A., 2015, Imaging spectroscopy of geological samples and outcrops: Novel insights from microns to meters. GSA Today, doi: 10.1130/GSATG252A.1.

Grieve, R.A.F., 2006, Impact Structures in Canada. Geological Association of Canada, 210 p.

Grieve, R.A.F., 1975, Petrology and chemistry of the impact melt at Mistastin Lake crater, Labrador. Geological Society of America Bulletin, v. 86, p. 1617–1629.

Grieve, R.A.F., 1978, The melt rocks at Brent Crater, Ontario, Canada. Proceedings Lunar and Planetary Science Conference 9th, p. 2579–2608.

Grieve, R.A.F., Dence, M.R., and Robertson, P.B., 1977, Cratering processes: As interpreted from the occurrence of impact melts*, *in* Roddy, D.J., Pepin, R.O., and Merrill, R.B. eds., Impact and Explosion Cratering, New York, Pergamon Press, p. 791–814.

Grieve, R.A.F., Robertson, P.B., and Dence, M.R., 1981, Constraints on the formation of ring impact structures, based on terrestrial data*, *in* Schultz, P.H. and Merrill, R.B. eds., Multi-ring Basins: Formation and Evolution; Proceedings of the Lunar and Planetary Science Conference, Houston, Pergamon Press, Inc., p. 37–57.

Gruninger, J.H., Ratkowski, A.J., and Hoke, M.L., 2004, The sequential maximum angle convex cone (SMACC) endmember model, *in* Shen, S.S. and Lewis, P.E. eds., Algorithms and Technologies for Multispectral, Hyperspectral, and Ultraspectral Imagery X, International Society for Optics and Photonics, v. Proc. SPIE 5425, doi: 10.1117/12.543794.

Gucsik, A., 2007, Micro-Raman spectroscopy of reidite as an impact-induced high pressure polymorph of zircon: Experimental investigation and attempt to application. Acta Mineralogica Petrographica, v. 47, p. 17–24.

Hart, R.J., Andreoli, M.A.G., Tredoux, M., Moser, D., Ashwal, L.D., Eide, E.A., Webb, S.J., and Brandt, D., 1997, Late Jurassic age for the Morokweng impact structure, southern Africa. Earth and Planetary Science Letters, v. 147, p. 25–35, doi: 10.1016/S0012-821X(97)00006-X.

Hathway, B., Dolby, G., McNeil, D.H., Kamo, S.L., Heizler, M.T., Joyce, N., and Plint, G., 2013, Revised stratigraphy, regional correlations and new bentonite radiometric ages for the Albian Loon River Formation, Fort St. John Group, northwestern Alberta. Bulletin of Canadian Petroleum Geology, v. 61, p. 331–358.

Hayes, B.J.R., Christopher, J.E., Rosenthal, L., Los, G., McKercher, B., Minken, D., Tremblay, Y.M., Fennell, J., and Smith, D.G., 1994, Chapter 19 - Cretaceous Mannville Group of the Western Canada Sedimentary Basin. Geological Atlas of the Western Canada Sedimentary Basin, G.D. Mossop and I. Shetsen (comp.), http://ags.aer.ca/publications/chapter-19-cretaceous-mannville-group (accessed July 2018).

Hecht, L., Wittmann, A., Schmitt, R.-T., and Stoeffler, D., 2004, Composition of impact melt particles and the effects of post-impact alteration in suevitic rocks at the Yaxcopoil-1 drill core, Chicxulub Crater, Mexico. Meteoritics & Planetary Science, v. 39, p. 1169–1186, doi: 10.1111/j.1945-5100.2004.tb01135.x.

Hildebrand, R.S., Hoffman, P.F., and Bowring, S.A., 1987, Tectono-magmatic evolution of the 1.9-Ga great bear magmatic zone, Wopmay orogen, northwestern Canada. Journal of Volcanology and Geothermal Research, v. 32, p. 99–118, doi: 10.1016/0377-0273(87)90039-4.

Hodych, J.P., and Dunning, G.R., 1992, Did the Manicouagan impact trigger end-of-Triassic mass extinction? Geology, v. 20, p. 51–54, doi: 10.1130/0091-7613(1992)020<0051:DTMITE>2.3.CO;2.

Hubbard, S.M., Pemberton, S.G., and Howard, E.A., 1999, Regional geology and sedimentology of the basal Cretaceous Peace River Oil Sands deposit, north-central Alberta. Bulletin of Canadian Petroleum Geology, v. 47, p. 270–297.

Hunt, G.R., 1977, Spectral signatures of particulate minerals in the visible and near infrared. Geophysics, v. 42, p. 501–513, doi: 10.1190/1.1440721.

Jourdan, F., Reimold, W.U., and Deutsch, A., 2012, Dating Terrestrial Impact Structures. Elements, v. 8, p. 49–53.

Jourdan, F., Renne, P.R., and Reimold, W.U., 2009, An appraisal of the ages of terrestrial impact structures. Earth and Planetary Science Letters, v. 286, p. 1–13, doi: 10.1016/j.epsl.2009.07.009.

Kaiser, A., Lobert, M., and Telle, R., 2008, Thermal stability of zircon (ZrSiO4). Journal of the European Ceramic Society, v. 28, p. 2199–2211, doi: 10.1016/j.jeurceramsoc.2007.12.040.

Kalleson, E., Corfu, F., and Dypvik, H., 2009, U-Pb systematics of zircon and titanite from the Gardnos impact structure, Norway: Evidence for impact at 546Ma? Geochimica et Cosmochimica Acta, v. 73, p. 3077–3092, doi: 10.1016/j.gca.2009.02.020.

Kamo, S.L., Reimold, W.U., Krogh, T.E., and Colliston, W.P., 1996, A 2.023 Ga age for the Vredefort impact event and a first report of shock metamorphosed zircons in pseudotachylitic breccias and Granophyre. Earth and Planetary Science Letters, v. 144, p. 369–387, doi: 10.1016/S0012-821X(96)00180-X.

Kenkmann, T., Poelchau, M.H., and Wulf, G., 2014, Structural geology of impact craters. Journal of Structural Geology, v. 62, p. 156–182, doi: 10.1016/J.JSG.2014.01.015.

Kenny, G.G., Morales, L.F., Whitehouse, M.J., Petrus, J.A., and Kamber, B.S., 2017, The formation of large neoblasts in shocked zircon and their utility in dating impacts. Geology, v. 45, p. 1003–1006, doi: 10.1130/G39328.1.

Kirkland, C. L., Smithies, R. H., Taylor, R. J. M., Evans, N., and McDonald, B. 2015. Zircon Th/U ratios in magmatic environs. Lithos, v. 212-215, p. 397-414, doi: https://doi.org/10.1016/j.lithos.2014.11.021.

Kirsimäe, K., and Osinski, G.R., 2012, Impact-Induced Hydrothermal Activity, in Osinski, G.R. and Pierazzo, E. eds., Impact Cratering, John Wiley & Sons, Ltd, p. 76–89, doi: 10.1002/9781118447307.ch6.

Krogh, T.E., McNutt, R.H., and Davis, G.L., 1982, Two high precision U–Pb zircon ages for the Sudbury Nickel Irruptive. Canadian Journal of Earth Sciences, v. 19, p. 723–728, doi: 10.1139/e82-061.

Krohn, M.D., Kendall, C., Evans, J.R., and Fries, T.L., 1993, Relations of ammonium minerals at several hydrothermal systems in the western U.S.. Journal of Volcanology and Geothermal Research, v. 56, p. 401–413, doi: 10.1016/0377-0273(93)90005-C.

Kruijer, T.S., and Kleine, T., 2017, Tungsten isotopes and the origin of the Moon. Earth and Planetary Science Letters, v. 475, p. 15–24, doi: 10.1016/J.EPSL.2017.07.021.

Kruse, F.A., 1996, Identification and mapping of minerals in drill core using hyperspectral image analysis of infrared reflectance spectra. International Journal of Remote Sensing, v. 17, p. 1623–1632, doi: 10.1080/01431169608948728.

Kukkonen, I.T., Kivekas, L., and Paananen, M., 1992, Physical properties of karnaite (impact melt), suevite and impact breccia in the Lappajarvi meteorite crater, Finland. Tectonophysics, v. 216, p. 111–122.

MacLagan, E.A., Walton, E.L., Herd, C.D.K., and Dence, M., 2018, Investigation of impact melt in allochthonous crater-fill deposits of the Steen River impact structure, Alberta, Canada. Meteoritics & Planetary Science, doi: 10.1111/maps.13122.

McCleary, J., 1997, Metallic and industrial mineral assessment report on the Steen River impact crater. Alberta Energy Resources Conservation Board, Metallic and Industrial Mineral Assessment Report, 19970004.

van der Meer, F.D., van der Werff, H.M.A., van Ruitenbeek, F.J.A., Hecker, C.A., Bakker, W.H., Noomen, M.F., van der Meijde, M., Carranza, E.J.M., Smeth, J.B. de, and Woldai, T., 2012, Multi- and hyperspectral geologic remote sensing: A review: International Journal of Applied Earth Observation and Geoinformation, v. 14, p. 112–128, doi: 10.1016/J.JAG.2011.08.002.

Meijer Drees, N.C., 1994, Chapter 10 - Devonian Elk Point Group of the Western Canada Sedimentary Basin, *in* Mossop, G.D. and Shetsen, I. eds., Geological Atlas of the Western Canada Sedimentary Basin, Canadian Society of Petroleum Geologists and Alberta Research Council, p. 129–147.

Melosh, H.J., 2017, Impact geologists, beware! Geophysical Research Letters, v. 44, p. 8873–8874, doi: 10.1002/2017GL074840.

Molak, B., Balzer, S.A., Olson, R.A., and Waters, E.J., 2001, Petrographic, mineralogical and lithogeochemical study of core from three drillholes into the Steen River structure, Northern Alberta. Alberta Energy and Utilities Board, Alberta Geological Survey, Earth Sciences Report 2001-04, p. 1–91.

Morgan, J.V., Warner, M.R., Collins, G.S., Melosh, H.J., and Christeson, G.L., 2000, Peak-ring formation in large impact craters: geophysical constraints from Chicxulub. Earth and Planetary Science Letters, v. 183, p. 347–354, doi: 10.1016/S0012-821X(00)00307-1.

Moser, D.E., 1997, Dating the shock wave and thermal imprint of the giant Vredefort impact, South Africa. Geology, v. 25, p. 7–10, doi: 10.1130/0091-7613(1997)025<0007:DTSWAT>2.3.CO;2.

Moser, D.E., Cupelli, C.L., Barker, I.R., Flowers, R.M., Bowman, J.R., Wooden, J., and Hart, J.R., 2011, New zircon shock phenomena and their use for dating and reconstruction of large impact structures revealed by electron nanobeam (EBSD, CL, EDS) and isotopic U–Pb and (U–Th)/He analysis of the Vredefort dome. Canadian Journal of Earth Sciences, v. 48, p. 117–139, doi: 10.1139/E11-011.

Mougel, B., Moynier, F., and Göpel, C., 2018, Chromium isotopic homogeneity between the Moon, the Earth, and enstatite chondrites. Earth and Planetary Science Letters, v. 481, p. 1–8, doi: 10.1016/J.EPSL.2017.10.018.

Naumov, M. V., 2005, Principal features of impact-generated hydrothermal circulation systems: mineralogical and geochemical evidence. Geofluids, v. 5, p. 165–184, doi: 10.1111/j.1468-8123.2005.00092.x.

Okulitch, A. V, 2006, Bedrock geology, Peace River, Alberta:, doi: 10.4095/222164.

Osinski, G.R., 2004, Impact melt rocks from the Ries structure, Germany: An origin as impact melt flows? Earth and Planetary Science Letters, v. 226, p. 529–543, doi: 10.1016/j.epsl.2004.08.012.

Osinski, G.R., 2006, The geological record of meteorite impacts. 1st International Conference on Impact Cratering in the Solar System, v. SP-612, p. 1–12.

Osinski, G.R., Grieve, R.A.F., Chanou, A., and Sapers, H.M., 2016, The "suevite" conundrum, Part 1: The Ries suevite and Sudbury Onaping Formation compared. Meteoritics & Planetary Science, v. 18, p. 1–18, doi: 10.1111/maps.12728.

Osinski, G.R., Spray, J.G., and Lee, P., 2005, Impactites of the Haughton impact structure, Devon Island, Canadian

High Arctic. Meteoritics & Planetary Science, v. 40, p. 1813–1834, doi: 10.1111/j.1945-5100.2005.tb00148.x.

Osinski, G.R., Tornabene, L.L., Banerjee, N.R., Cockell, C.S., Flemming, R., Izawa, M.R.M., McCutcheon, J., Parnell, J., Preston, L.J., Pickersgill, A.E., Pontefract, A., Sapers, H.M., and Southam, G., 2013, Impact-generated hydrothermal systems on Earth and Mars. Icarus, v. 224, p. 347–363, doi: 10.1016/j.icarus.2012.08.030.

Otsuka, R., 1986, Recent studies on the decomposition of the dolomite group by thermal analysis. Thermochimica Acta, v. 100, p. 69–80, doi: 10.1016/0040-6031(86)87051-4.

Pike, R.J., 1980, Control of crater morphology by gravity and target type: Mars, Earth, Moon. Proceedings of the 11th Lunar and Planetary Science Conference , p. 2159–2189.

Reddy, S.M., Johnson, T.E., Fischer, S., Rickard, W.D.A., and Taylor, R.J.M., 2015, Precambrian reidite discovered in shocked zircon from the Stac Fada impactite, Scotland. Geology, v. 43, p. 899–902, doi: 10.1130/G37066.1.

Reddy, S.M., Timms, N.E., Trimby, P., Kinny, P.D., Buchan, C., and Blake, K., 2006, Crystal-plastic deformation of zircon: A defect in the assumption of chemical robustness. Geology, v. 34, p. 257–260, doi: 10.1130/G22110.1.

Reimold, W.U., Koeberl, C., and Brandt, D., 1997, Suevite at the Roter Kamm impact crater, Namibia. Meteoritics & Planetary Science, v. 32, p. 431–437.

Reimold, W.U., Koeberl, C., Gibson, R.L., and Dressler, B.O., 2005, Economic Mineral Deposits in Impact Structures: A Review, in Impact Tectonics, Berlin/Heidelberg, Springer-Verlag, p. 479–552, doi: 10.1007/3-540-27548-7_20.

Robbins, S.J., and Hynek, B.M., 2012, A new global database of Mars impact craters ≥1 km: 2. Global crater properties and regional variations of the simple-to-complex transition diameter. Journal of Geophysical Research: Planets, v. 117, p. n/a-n/a, doi: 10.1029/2011JE003967.

Robertson, G.A., 1997, The Steen River Structure, Alberta Canada: Subsurface identification and hydrocarbon occurrences, in Oklahoma Geological Survey Circular 100, Calgary, Alberta, p. 385–390.

Rogge, D.M., Rivard, B., Zhang, J., Sanchez, A., Harris, J., and Feng, J., 2007, Integration of spatial–spectral information for the improved extraction of endmembers. Remote Sensing of Environment, v. 110, p. 287–303, doi: 10.1016/J.RSE.2007.02.019.

Schaltegger, U., Fanning, C.M., Guè, D., Maurin, J.C., Schulmann, K., and Gebauer, D., 1999, Growth, annealing and recrystallization of zircon and preservation of monazite in high-grade metamorphism: conventional and in-situ U-Pb isotope, cathodoluminescence and microchemical evidence. Contributions to Mineralogy and Petrology, v. 134, p. 186–201.

Scharer, U., and Deutsch, A., 1990, Isotope systematics and shock-wave metamorphism: II. U-Pb and Rb-Sr in naturally shocked rocks; the Haughton Impact Structure, Canada. Geochimica et Cosmcchimica Acta, v. 54, p. 3435–3447.

Schmieder, M., Tohver, E., Jourdan, F., Denyszyn, S.W., and Haines, P.W., 2015, Zircons from the Acraman impact melt rock (South Australia): Shock metamorphism, U–Pb and 40Ar/39Ar systematics, and implications for the isotopic dating of impact events. Geochimica et Cosmochimica Acta, v. 161, p. 71–100, doi: 10.1016/J.GCA.2015.04.021.

Schoene, B., 2014, 4.10 – U–Th–Pb Geochronology, in Treatise on Geochemistry, Princeton, NJ, USA, Elsevier, p. 341–378, doi: 10.1016/B978-0-08-095975-7.00310-7.

Singleton, A.C., Osinski, G.R., Mccausland, P.J.A., and Moser, D.E., 2011, Shock-induced changes in density and porosity in shock-metamorphosed crystalline rocks, Haughton impact structure, Canada. Meteoritics and Planetary Science, v. 46, p. 1774–1786, doi: 10.1111/j.1945-5100.2011.01290.x.

Singleton, A.C., Osinski, G.R., and Shieh, S.R., 2015, Microscopic effects of shock metamorphism in zircons from the Haughton impact structure, Canada, in Geological Society of America Special Papers, Geological Society of America, v. 518, p. 135–148, doi: 10.1130/2015.2518(09).

51

Spray, J.G., 2018, Earth Impact Database: Planetary and Space Science Centre, University of New Brunswick, http://www.passc.net/EarthImpactDatabase/ (accessed April 2018).

Spray, J.G., Butler, H.R., and Thompson, L.M., 2004, Tectonic influences on the morphometry of the Sudbury impact structure: Implications for terrestrial cratering and modeling. Meteoritics & Planetary Science, v. 39, p. 287–301, doi: 10.1111/j.1945-5100.2004.tb00341.x.

Steiger, R.H., and Jager, E., 1977, Subcommission on Geochronology; convention on the use of decay constants in geochronology and cosmochronology; Contributions to the geologic time scale. Studies in Geology (Tulsa), v. 36, p. 67–71.

Stern, R.A., and Amelin, Y., 2003, Assessment of errors in SIMS zircon U–Pb geochronology using a natural zircon standard and NIST SRM 610 glass. Chemical Geology, v. 197, p. 111–146, doi: 10.1016/S0009-2541(02)00320-0.

Stöffler, D., 1971, Progressive metamorphism and classification of shocked and brecciated crystalline rocks at impact craters. Journal of Geophysical Research, v. 76, p. 5541–5551, doi: 10.1029/JB076i023p05541.

Stöffler, D., 1977, Research drilling Nördlingen 1973: Polymict breccias, crater basement, and cratering model of the Ries impact structure. Geological Bavarica, v. 75, p. 443–458.

Stöffler, D., Artemieva, N.A., Wünnemann, K., Reimold, W.U., Jacob, J., Hansen, B.K., and Summerson, I.A.T., 2013, Ries crater and suevite revisited-Observations and modeling Part I: Observations. Meteoritics & Planetary Science, v. 48, p. 515–589, doi: 10.1111/maps.12086.

Stöffler, D., and Grieve, R.A.F., 2007, Impactites, in Fettes, D. and Desmons, J. eds., Metamorphic Rocks: A Classification and Glossary of Terms, Recommendations of the International Union of Geological Sciences, Cambridge, Cambridge University Press, p. 82–92, 111- 125 and 126-242.

Stöffler, D., Hamann, C., and Metzler, K., 2018, Shock metamorphism of planetary silicate rocks and sediments: Proposal for an updated classification system. Meteoritics & Planetary Science, v. 53, p. 5–49, doi: 10.1111/maps.12912.

Stöffler, D., and Langenhorst, F., 1994, Shock metamorphism of quartz in nature and experiment: I. Basic observation and theory*. Meteoritics, v. 29, p. 155–181, doi: 10.1111/j.1945-5100.1994.tb00670.x.

Stott, D.F., 1971, Lower Cretaceous Bullhead Group between Bullmoose Mountain and Tetsa River, Rocky Mountain Foothills, northeastern British Columbia. Geological Survey of Canada: Department of Energy, Mines and Resources Canada, p. 393, doi: 10.4095/100349.

Therriault, A.M., Grieve, R.A.F., and Reimold, W.U., 1997, Original size of the Vredefort Structure: Implications for the geological evolution of the Witwatersrand Basin. Meteoritics & Planetary Science, v. 32, p. 71–77, doi: 10.1111/j.1945-5100.1997.tb01242.x.

Timms, N.E., Erickson, T.M., Pearce, M.A., Cavosie, A.J., Schmieder, M., Tohver, E., Reddy, S.M., Zanetti, M.R., Nemchin, A.A., and Wittmann, A., 2017, A pressure-temperature phase diagram for zircon at extreme conditions. Earth-Science Reviews, v. 165, p. 185–202, doi: 10.1016/j.earscirev.2016.12.008.

Tohver, E., Lana, C., Cawood, P.A., Fletcher, I.R., Jourdan, F., Sherlock, S., Rasmussen, B., Trindade, R.I.F., Yokoyama, E., Souza Filho, C.R., and Marangoni, Y., 2012, Geochronological constraints on the age of a Permo–Triassic impact event: U–Pb and 40Ar/39Ar results for the 40 km Araguainha structure of central Brazil. Geochimica et Cosmochimica Acta, v. 86, p. 214–227, doi: 10.1016/J.GCA.2012.03.005.

Underhill, J.C., 1964, Report on Iron Prospecting Permit No. 28 - Russet Creek Area.. Imperial Oil Limited: Geological Department. Alberta Minerals Assessment Reporting System. MAR 19640007. p. 1-14.

Walton, E., Hughes, A., MacLagan, E., Herd, C.D.K., and Dence, M., 2017, A previously unrecognized high-temperature impactite from the Steen River impact structure, Alberta, Canada. Geology, v. 45, p. 291–294, doi: 10.1130/G38556.1.

Walton, E., Sharp, T.G., and Hu, J., 2016, Frictional melting processes and the generation of shock veins in terrestrial

impact structures: Evidence from the Steen River impact structure, Alberta, Canada. Geochimica et Cosmochimica Acta, v. 180, p. 256–270, doi: 10.1016/j.gca.2016.02.024.

Walton, E.L., Sharp, T.G., Hu, J., and Tschauner, O., 2018, Investigating the response of biotite to impact metamorphism: Examples from the Steen River impact structure, Canada. Meteoritics & Planetary Science, v. 53, p. 75–92, doi: 10.1111/maps.13011.

Walton, E.L., Timms, N.E., Hauck, T.E., MacLagan, E.A., and Herd, C.D.K., 2018, Evidence of impact melting and decomposition of sedimentary target rocks from the Steen River impact structure, Alberta, Canada. Earth and Planetary Science Letters, Accepted.

Wang, K., and Jacobsen, S.B., 2016, Potassium isotopic evidence for a high-energy giant impact origin of the Moon. Nature, v. 538, p. 487–490, doi: 10.1038/nature19341.

Wetherill, G.W., 1975, Late heavy bombardment of the moon and terrestrial planets. Proceedings of the Lunar and Planetary Science Conference, p. 1539–1561.

Williams, L.B., Ferrell, R.E., Chinn, E.W., and Sassen, R., 1989, Fixed-ammonium in clays associated with crude oils. Applied Geochemistry, v. 4, p. 605–616, doi: 10.1016/0883-2927(89)90070-X.

Wilson, J., Langenberg, W., Jeffries, L., Tooth, J., Grieve, R.A.F., and Berkes, Z., 1989, Proposal for scientific drilling on the Steen River structure, Northwestern Alberta.. Alberta Research Council, Alberta Geological Survey, Open File Report 1989-04.

Winzer, S.R., 1972, The Steen River Asttobleme, Alberta, Canada, *in* 24th International Geological Congress, Montreal, Canada, p. 148–156.

Wittmann, A., Kenkmann, T., Schmitt, R.T., and Stoffler, D., 2006, Shock-metamorphosed zircon in terrestrial impact craters. Meteoritics & Planetary Science, v. 41, p. 433–454, doi: 10.1111/j.1945-5100.2006.tb00472.x.

Wrote, J.M., and Leckie, D.A., 1999, Palynological age constraints on the Cadomin and Dalhousie formations in SW Alberta. Bulletin of Canadian Petroleum Geology, v. 47, p. 199–222.

Young, E.D., Kohl, I.E., Warren, P.H., Rubie, D.C., Jacobson, S.A., and Morbidelli, A., 2016, Oxygen isotopic evidence for vigorous mixing during the Moon-forming giant impact: Science (New York, N.Y.), v. 351, p. 493–6, doi: 10.1126/science.aad0525.

APPENDIX

A.1 SUMMARY OF ANALYTICAL METHODS

A.1.1 HYPERSPECTRAL SCANNING

Six representative boxes were selected from core ST003 as a preliminary test on the feasibility of using hyperspectral scanning for characterization of the SRIS impact breccias. These boxes included approximate depth ranges of 217-219 m, 229-231 m, 272-274 m, 298-300 m, 329-331 m, and 367-369 m. The TIR data was not used due to excessive noise. A spatial subset was applied to each box from the VNIR and SWIR data sets to remove the cardboard box and table surface, then the images were mosaicked together using a pixel-based method. The top 4 (2511-2530 nm) and bottom 10 (928-985 nm) SWIR bands were removed due to excessive noise and the spectra were smoothed using a 3x3 kernel-size, low-pass convolution. An automated spatial-spectral endmember extraction (SSEE) (Rogge et al., 2007) resulted in 107 spectral endmembers which were grouped manually based on similarities in spectral features. The spectra within each of the resulting 22 groups were averaged using spectral math to produce 22 endmember spectra.

The averaged spectrum from each group was analyzed using a spectral angle mapper (SAM) on all remaining bands (991.38-2505.21 nm) to approximate the corresponding mineral for each from one of the ENVI default libraries: U. S. Geological Survey (USGS) (Clark et al., 2007), the NASA Jet Propulsion Laboratory (JPL), or Johns Hopkins University (JHU) (Baldridge et al., 2009). Further analysis of the spectral groups enabled a reduction to 13 endmembers from the original 22. SAM was then used to allocate each pixel in the scanned image to one of the 13 spectral groups, and thereby assign it a mappable color. Multiple spectral angles were used, ranging from 0.025 to 0.100 radians. Using both Tactical Hyperspectral Operations Resource (THOR) material identification and the maps produced from SAM, the mineral identifications of the 13 groups were refined and the new maps were used to select samples of purest endmembers for XRD analysis. Based on the success with these preliminary scans, we proceeded to scan the entire breccia unit in all three cores (ST001, ST002, ST003).

TIR data was cleaner during the full scanning process; however, only bands 69-100 (7361-12020 nm) were kept due to excessive noise in the other bands. Similar to the method described

above, a smoothing filter was applied and a sequential maximum angle convex cone (SMACC) endmember extraction (Gruninger et al., 2004) was run on the new TIR and SWIR data from all three cores. This collected ~70-80 TIR endmembers and ~90-110 SWIR endmembers from each of the three cores, which were grouped based on similar spectral features. The groups were averaged individually, then compared between cores ST001, ST002, and ST003 and combined if similar, resulting in 8 TIR endmembers and 15 SWIR endmembers. Some SWIR endmembers were removed as they mapped shaded areas or were featureless spectra. The SAM results from the averaged TIR endmembers excluded a significant proportion of the matrix unless the spectral angle was set at a high value. The larger the spectral angle, the more difference exists between the mapped endmember and the individual pixel spectra. To fix this issue, additional spectra were collected manually from unmapped areas; these were also grouped and averaged. The manually collected endmembers were from the groundmass, granite clasts, and shale. The final 11 TIR endmembers and 13 SWIR endmembers were mapped on the core images using SAM (Fig. A.2). The mineral profiles in Figure A.2 were made in Adobe Illustrator to highlight mineral abundance with respect to depth. Minerals that constitute only a minor proportion (present in only small areas), were labeled with a dashed line, while major constituents are highlighted with solid lines.

A.1.2 XRD ANALYSES

Samples were crushed with an automated agate mortar and pestle for six minutes each. The mortar and pestle were cleaned with pure quartz between each sample. Powdered samples (~1 g of each) were analyzed at the University of Alberta using a Rigaku Geigerflex Powder Diffractometer with a cobalt tube, a graphite monochromator, and a scintillation detector. Data processing and peak matching were done using JADE software.

A.1.3 SIMS ANALYSES

A 25 mm diameter mount (CCIM #M1501, GSC IP919) was prepared at the Canadian Centre for Isotopic Microanalysis (CCIM) comprising sectioned unknown zircons and U-Pb reference materials, including 6266 zircon ($^{206}Pb/^{238}U$ = 559.0 Ma; Stern and Amelin, 2003). The mount was cleaned with alkaline soap, deionized water, and weak HCl prior to Au coating. A Zeiss EVO MA15 scanning electron microscope (SEM) fitted with a broadband cathodoluminescence (CL) detector (ETP Semra, Pty. Ltd., Sydney, Australia) and semiconductor backscattered electron

detector (BSE) was employed for characterizing internal grain zonation. Typical beam conditions were 15 kV or 20 kV potential, with a 3 – 5 nA current.

Secondary ion mass spectrometer (SIMS) analyses of U-Pb isotopes, plus Yb and Hf, were carried out using the SHRIMP II instrument at the J.C. Roddick Ion Probe Laboratory of the Geological Survey of Canada, Ottawa following analytical procedures modified from those described by Stern (1997). The primary beam comprised 10 keV mass-filtered $^{16}O^{-}$ ions (~1.8 nA), projected onto the sample surface using Kohler imaging (50 μm aperture), to produce a probe of ~10 μm diameter. Positive secondary ions were measured by peak hopping at a nominal mass resolution of 5000 (1% peak height definition) using a single electron multiplier. Eleven secondary ions (count times in seconds) were collected over 6 scans: $^{174}Yb^{16}O^{+}$(1), $^{180}Hf^{16}O^{+}$(1), $^{90}Zr_2^{16}O^{+}$ (1), $^{204}Pb^{+}$(15), $^{204.05}$background^{+}(15), $^{206}Pb^{+}$(20), $^{207}Pb^{+}$(30), $^{208}Pb^{+}$(2), $^{238}U^{+}$(8), $^{232}Th^{16}O^{+}$(1), $^{238}U^{16}O^{+}$(3), with data processing using SQUID 2.50.11.10.15 (rev. 15 Oct 2011; Ludwig, 2009). Count rates were corrected for a deadtime of 20 ns.

The $^{206}Pb/^{238}U$ ages were calibrated against 6266 zircon, using a calibration constant ('a') determined from the relationship $^{206}Pb^{+}/^{238}U^{+} = a \cdot (^{254}UO^{+}/^{238}U^{+})^{m}$, where the m was 1.83 for the session. The 1σ external errors of $^{206}Pb/^{238}U$ ratios reported incorporate the error in calibrating the standard in addition to counting uncertainties. Common Pb correction utilized the Pb composition of the surface blank (Stern, 1997). The Th/U ratios and Th abundances were determined from $^{248}ThO^{+}/^{254}UO^{+}$ using measured $^{232}Th/^{238}U$ discrimination factors for the session (~1.0). Concentration data for U, Yb, and Hf were calculated using $^{196}Zr_2O^{+}$-normalized sensitivity factors derived from standard 6222 with values of 903 ppm, 229 ppm, and 8200 ppm (g/g) respectively. A secondary internal reference zircon (1242) was analyzed to monitor accuracy of the measured $^{207}Pb/^{206}Pb$ ratios and correct for any instrumental mass bias, however no mass bias was applied to the data. Isoplot v. 3.75 (Ludwig, 2012) was used to generate Concordia plots and calculate regression ages and weighted means. The error ellipses on the Concordia diagrams and the weighted mean errors are reported at 95% confidence intervals. Uranium decay constants are those of Jaffey et al. (1971).

The data table includes the measured $^{254}UO^{+}/^{238}U^{+}$ and $^{196}Zr_2O^{+}$ count rates, which aid in evaluating which Pb/U analyses could be biased due to a matrix mismatch with the 6266 reference

material and the well-preserved unknown zircons. Such zircon tends to be that which is dark in CL and has relatively low backscattered electron response, indicative of strong secondary alteration. We suggest that analyses having $^{254}UO^+/^{238}U^+$ between 5.8 and 6.7 will be reasonably well calibrated, compared to 'good' zircon with a range of 6.0 – 6.5. Similarly, primary beam normalized $^{196}Zr_2O^+$ count rates falling in the range 1800 – 2500 cps/nA are considered acceptable. Pb-U analyses that meet both of these criteria are considered well-calibrated. The remaining analyses may or may not have accurate Pb/U ratios, and therefore their interpretive value on Concordia plots is diminished. However, for completeness, some of the Concordia plots include all data so that the reader can visualize the whole data set, even though only the screened data are ultimately utilized in age interpretations.

A.2 REFERENCES CITED IN APPENDIX

Baldridge, A.M., Hook, S.J., Grove, C.I., Rivera, G., 2009. The ASTER spectral library version 2.0. Remote Sensing of Environment 113, 711–715. https://doi.org/10.1016/J.RSE.2008.11.007

Clark, R.N., Swayze, G.A., Wise, R., Livo, K.E., Kokaly, R.F., Sutley, S.J., 2007. USGS digital spectral library splib06a. U.S. Geological Survery, Digital Data Series 231. https://doi.org/10.1029/2002JE001847

Gruninger, J.H., Ratkowski, A.J., Hoke, M.L., 2004. The sequential maximum angle convex cone (SMACC) endmember model. In: Shen, S.S., Lewis, P.E. (Eds.), Algorithms and Technologies for Multispectral, Hyperspectral, and Ultraspectral Imagery X. International Society for Optics and Photonics. https://doi.org/10.1117/12.543794

Jaffey, A.H., Flynn, K.F., Glendenin, L.E., Bentley, W.C., Essling, A.M., 1971. Precision Measurement of Half-Lives and Specific Activities of ^{235}U and ^{238}U. Physical Review C: Nuclear Physics 4, 1889–1906. https://doi.org/10.1103/PhysRevC.4.1889

Ludwig, K.R., 2012. Isoplot 3.75: A Geochronological Toolkit for Microsoft Excel. Berkeley Geochronology Center Special Publication 5, 75.

Ludwig, K.R., 2009. SQUID2: A User's Manual, rev. 12 Apr, 2009. Berkeley Geochronology Center Special Publication 5, 110.

Rogge, D.M., Rivard, B., Zhang, J., Sanchez, A., Harris, J., Feng, J., 2007. Integration of spatial–spectral information for the improved extraction of endmembers. Remote Sensing of Environment 110, 287–303. https://doi.org/10.1016/J.RSE.2007.02.019

Stern, R.A., 1997. The GSC Sensitive High Resolution Ion Microprobe (SHRIMP): analytical techniques of zircon U-Th-Pb age determinations and performance evaluation, Radiogenic Age and Isotopic Studies: Report 10, Geological Survey of Canada. https://doi.org/10.4095/209089

Stern, R.A., Amelin, Y., 2003. Assessment of errors in SIMS zircon U–Pb geochronology using a natural zircon standard and NIST SRM 610 glass. Chemical Geology 197, 111–146. https://doi.org/10.1016/S0009-2541(02)00320-0

Table A. 1. XRD results

Sample	Depth (ft)	Minerals
E2a	716.5	Anorthite, sanidine, quartz, aerinite, lizardite, kaolinite
E2b	1213	Microcline, muscovite, albite, quartz, nontronite
E3-4-5	1062.5	Stellerite, enstatite, quartz
E5	715	Anorthite, quartz, muscovite, orthoclase, kaolinite, montmorillonite, calcite, sodalite, pyrite
E6	715.5	Orthoclase, quartz, albite, calcite, pyrite, montmorillonite, phlogopite
E7a	1082	Albite, diopside, melanite, lizardite, montmorillonite, quartz
E7b	1085	Diopside-ferrian, melanite, oligoclase, fluorohectorite, phlogopite, quartz, lizardite
E8	720	Calcite, vermiculite
E9a	1209	Albite, actinolite, quartz, orthoclase, phlogopite, clinochlore
E9b	1211.5	Potassic-chloro-hastingsite, orthoclase, quartz, vermiculite, albite, phlogopite
E10	896	Sanidine, albite, quartz, fluor-phlogopite, montmorillonite, magnesioferrite
E11	1211	Albite, quartz, clinochlore, actinolite, orthoclase, phlogopite
E12	764.5	Sanidine, vermiculite, quartz, hematite
E13	1211.5	Actinolite, quartz, albite, vermiculite, sanidine, phlogopite

Table A. 2. Endmember minerals / rocks and their corresponding formulas from hyperspectral maps

SWIR	Formula
Calcite	$CaCO_3$
Buddingtonite	$NH_4AlSi_3O_8$
Ammonio-smectite	$(NH4)_{0.33}(Al,Mg)_2Si_4O_{10}(OH)_2 \bullet nH_2O$
Analcime	$NaAlSi_2O_6 \bullet H_2O$
Nontronite	$Na_{0.3}Fe_2(Si,Al)_4O_{10}(OH)_2 \bullet nH_2O$
Buddingtonite+calcite	$NH_4AlSi_3O_8 + CaCO_3$
Gypsum	$CaSO_4 \bullet 2H_2O$
Montmorillonite	$(Na,Ca)_{0.3}(Al,Mg)_2Si_4O_{10}(OH)_2 \bullet n(H2O)$
Illite and/or muscovite	$(K,H_3O)(Al,Mg,Fe)_2(Si,Al)_4O_{10}[(OH)_2,(H2O)]$ and / or $KAl_2(Si_3Al)O_{10}(OH,F)_2$
Epidote and/or clinochlore	$Ca_2(Al,Fe)_2(SiO_4)_3(OH)$ and/or $(Mg,Fe)_3(Si,Al)_4O_{10}(OH)_2 \cdot (Mg,Fe)_3(OH)_6$
Albite and/or sanidine*	$NaAlSi_3O_8$ and / or $(K,Na)AlSi_3O_8$
Wollastonite	$CaSiO_3$
Granite-derived melt	$\sim(K,Na)AlSi_3O_8 + SiO_2 \pm Fe,Mg$

TIR	Formula
Marble	$\sim CaCO_3$
Analcime	$NaAlSi_2O_6 \bullet H_2O$
Nontronite	$Na_{0.3}Fe_2(Si,Al)_4O_{10}(OH)_2 \bullet nH_2O$
Gypsum and/or barite	$CaSO_4 \bullet 2H_2O$ and/or $BaSO_4$
Alkali feldspar	$KAlSi_3O_8 - NaAlSi_3O_8$
Alkali granite	$\sim(K,Na)AlSi_3O_8 + SiO_2$
Calcareous shale	Clay minerals + calcite
Biotite and/or saponite	$K(Mg,Fe)_3AlSi_3O_{10}(F,OH)_2$ and/or $Ca_{0.25}(Mg,Fe)_3((Si,Al)_4O_{10})(OH)_2 \bullet nH_2O)$
Hornblende	$(Ca,Na)_{2-3}(Mg,Fe,Al)_5(Al,Si)_8O_{22}(OH,F)_2$
Anorthite+calcite	$CaAl_2Si_2O_8 + CaCO_3$
Siltstone / shale	$\sim$Clay minerals

*The SWIR "feldspar" endmember represents a mixed spectral signature from fine-grained feldspar, pyroxene, and clay minerals in the groundmass that are smaller than the scan resolution. See Chapter 2 for details.
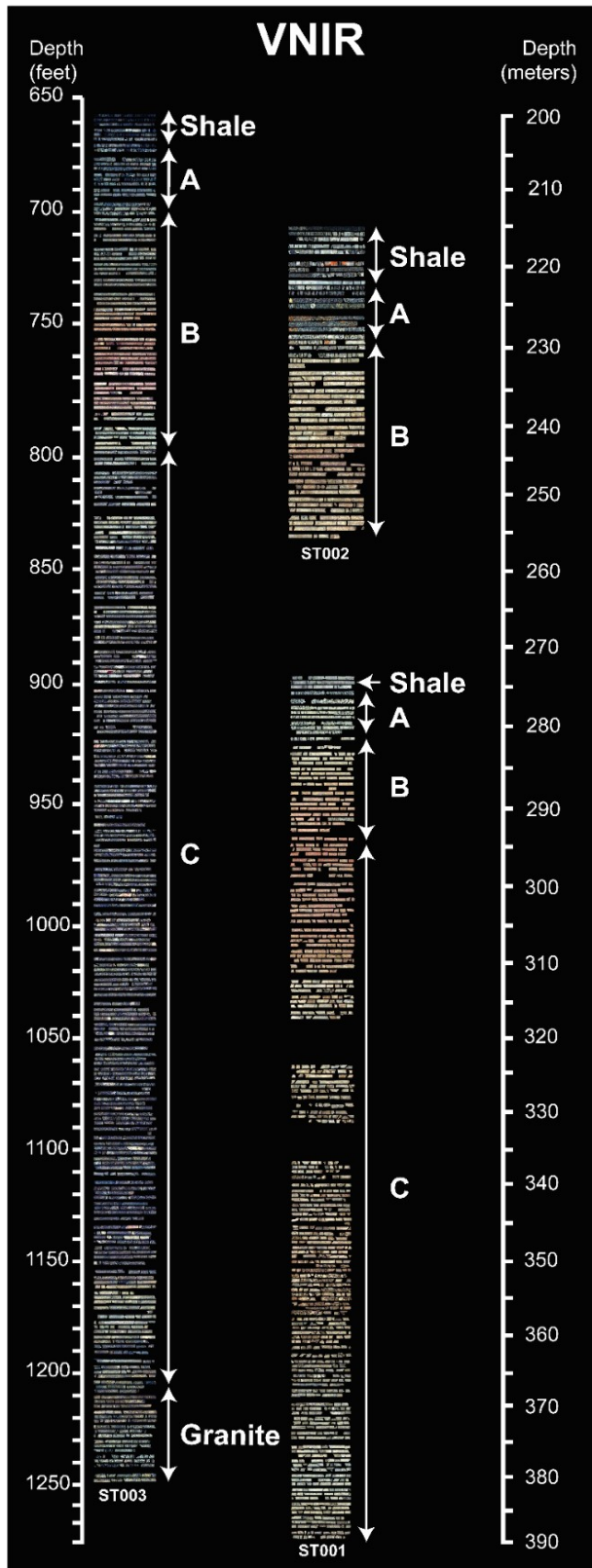
Figure A. 1. VNIR scans of cores ST001, ST002, and ST003.
Channels used are R:702.13, G:548.67, B:470.34 nm.
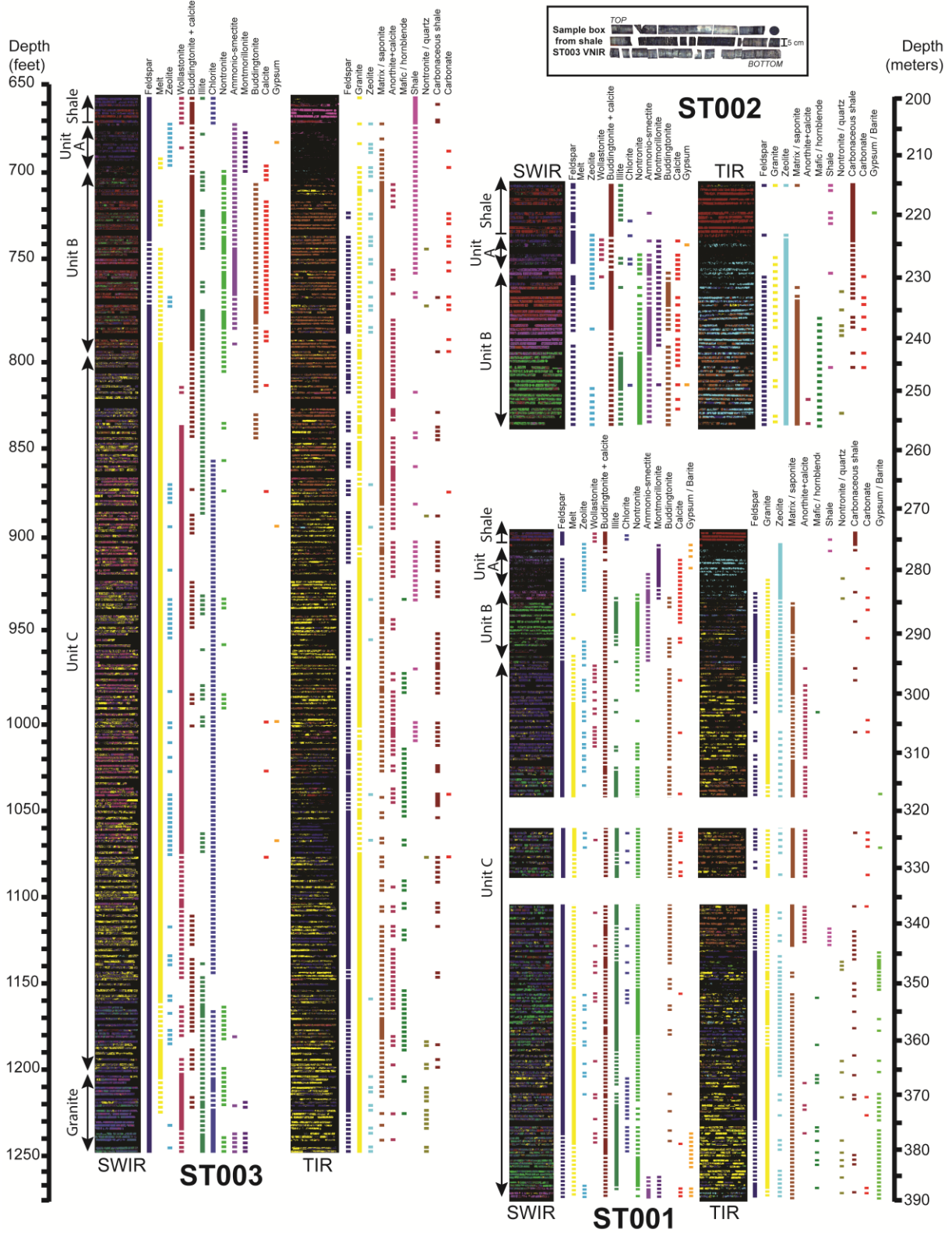
Figure A. 2. SWIR and TIR minerals maps of ST001, ST002, and ST003. The SWIR "feldspar" endmember (dark blue) represents a mixed spectral signature from fine-grained feldspar, pyroxene, and clay minerals in the groundmass that are smaller than the scan resolution.
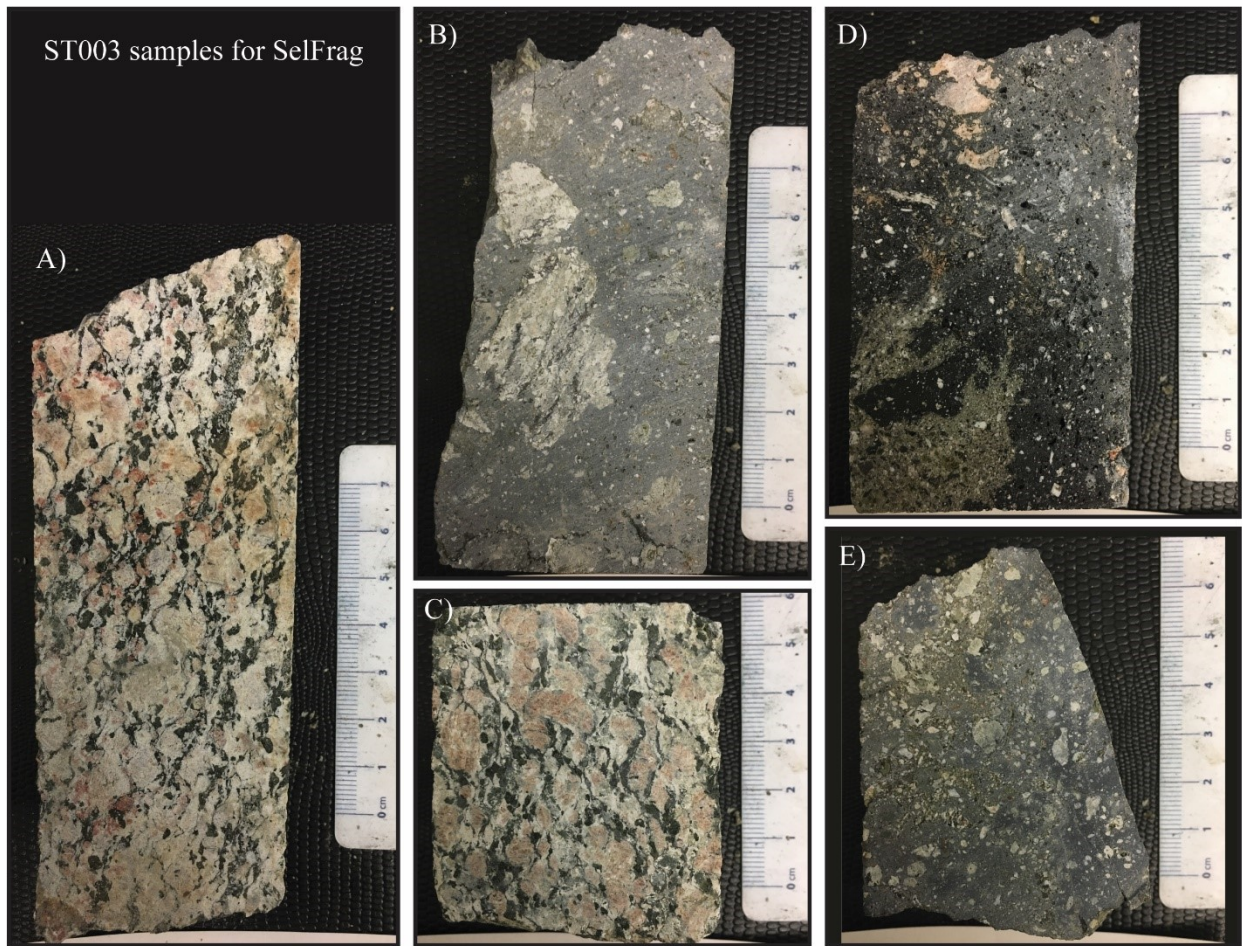
Figure A. 3. Samples from ST003 selected for SelFrag processing. A) Granite from 1241.5' (378.4 m) depth. B) Melt from 1181' ((360 m) depth. C) Granite from 1129' (344.1 m) depth. D) Melt from 956' (291.4 m) depth. E) Melt from 1210' (368.8 m) depth.
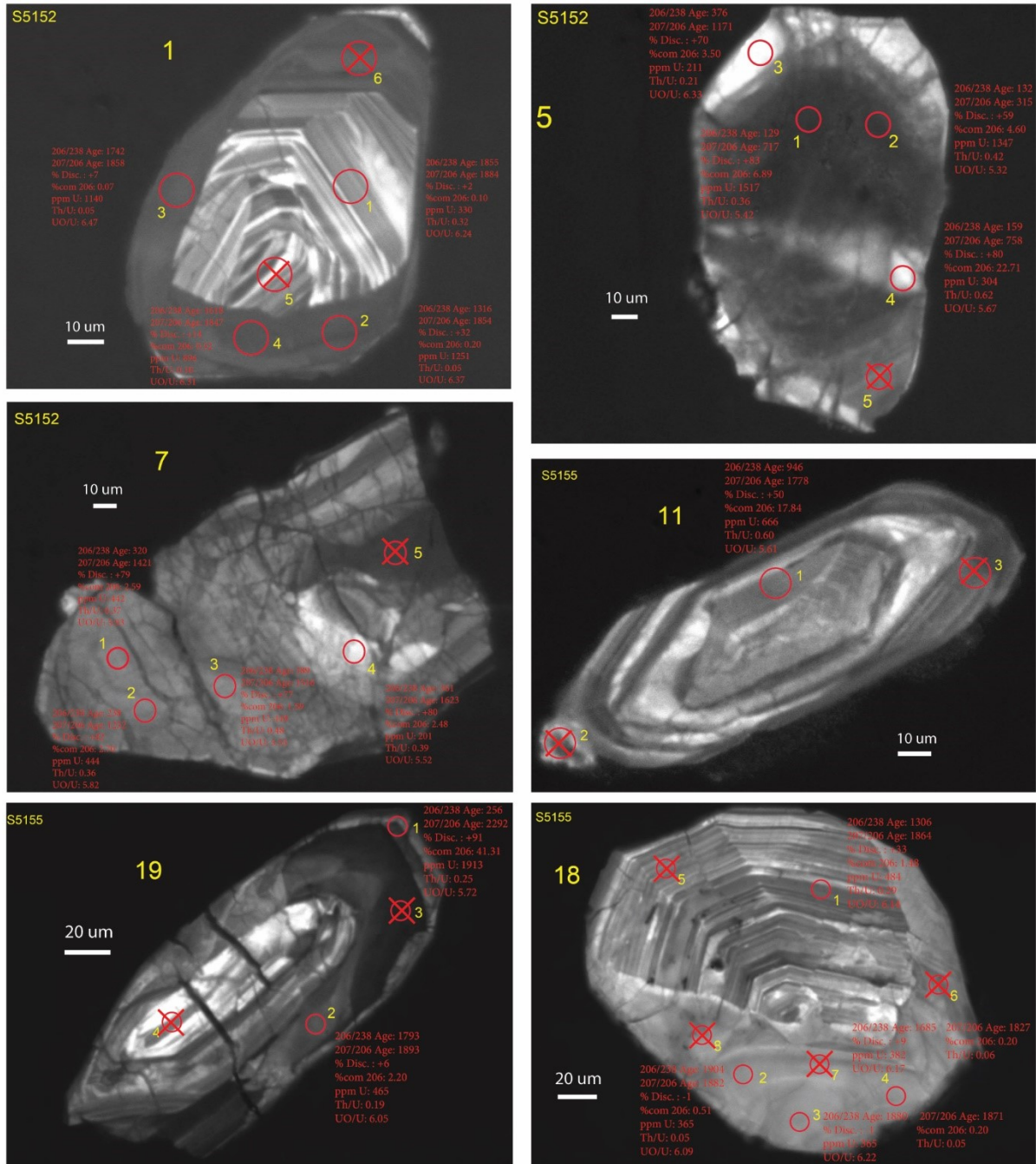
Figure A. 4. Locations of SIMS spots on analyzed zircon grains. Sample numbers correspond to Table A.3 and are listed with an "S" code (e.g. S5152). Large yellow numbers are grain numbers, and small yellow numbers associated with spots are spot numbers. Spots with an X were not analyzed.

S5155

24

206/238 Age: 197
207/206 Age: 1051
% Disc. : +83
%com 206: 15.62
ppm U: 727
Th/U: 0.57
UO/U: 5.96

206/238 Age: 134
207/206 Age: 284
% Disc. : +49
%com 206: 13.74
ppm U: 5898
Th/U: 0.39
UO/U: 5.90

206/238 Age: 136
207/206 Age: 436
% Disc. : +69
%com 206: 8.84
ppm U: 5705
Th/U: 0.35
UO/U: 5.90

206/238 Age: 342
207/206 Age: 1475
% Disc. : +79
%com 206: 10.64
ppm U: 598
Th/U: 0.45
UO/U: 5.88

10 um

S5154

206/238 Age: 1829
207/206 Age: 1834
% Disc. : +0
%com 206: 0.08
ppm U: 316
Th/U: 0.38
UO/U: 5.98

20 um

206/238 Age: 1734
207/206 Age: 1841
% Disc. : +7
%com 206: 0.07
ppm U: 320
Th/U: 0.20
UO/U: 5.97

S5156

32

206/238 Age: 1828
207/206 Age: 1855
% Disc. : +2
%com 206: 0.31
ppm U: 585
Th/U: 0.39
UO/U: 6.08

100 um

S5156

30

206/238 Age: 1858
207/206 Age: 1885
% Disc. : +2
%com 206: -0.07
ppm U: 194
Th/U: 0.64
UO/U: 6.12

100 um

S5154

2

206/238 Age: 271
207/206 Age: 1121
% Disc. : +77
%com 206: 2.66
ppm U: 326
Th/U: 0.43
UO/U: 5.76

20 um

206/238 Age: 126
207/206 Age: 380
% Disc. : +67
%com 206: 1.67
ppm U: 1238
Th/U: 0.14
UO/U: 5.33

4

206/238 Age: 1954
207/206 Age: 1885
% Disc. : -4
%com 206: 0.88
ppm U: 50
Th/U: 0.46
UO/U: 6.09

5

11

12

13

206/238 Age: 196
207/206 Age: 1742
% Disc. : +91
%com 206: 6.46
ppm U: 2063
Th/U: 0.40
UO/U: 7.13

S5156

19

206/238 Age: 1853
207/206 Age: 1851
% Disc. : -0
%com 206: 0.37
ppm U: 149
Th/U: 0.59
UO/U: 6.27

20

206/238 Age: 1827
207/206 Age: 1845
% Disc. : +1
%com 206: 0.24
ppm U: 159
Th/U: 0.38
UO/U: 6.15

21

206/238 Age: 1845
207/206 Age: 1861
% Disc. : +1
%com 206: 0.07
ppm U: 396
Th/U: 0.18
UO/U: 6.18

206/238 Age: 1802
207/206 Age: 1889
% Disc. : +4
%com 206: 0.28
ppm U: 775
Th/U: 0.37
UO/U: 6.59

29

206/238 Age: 1829
207/206 Age: 1850
% Disc. : +1
%com 206: 0.40
ppm U: 243
Th/U: 0.40
UO/U: 6.15

27

28

20 um

Figure A. 4. continued. Locations of SIMS spots on analyzed zircon grains. Sample numbers correspond to Table A.3 and are listed with an "S" code (e.g. S5152). Large yellow numbers are grain numbers, and small yellow numbers associated with spots are spot numbers. Spots with an X were not analyzed.

Table A. 3. Results from SIMS analysis

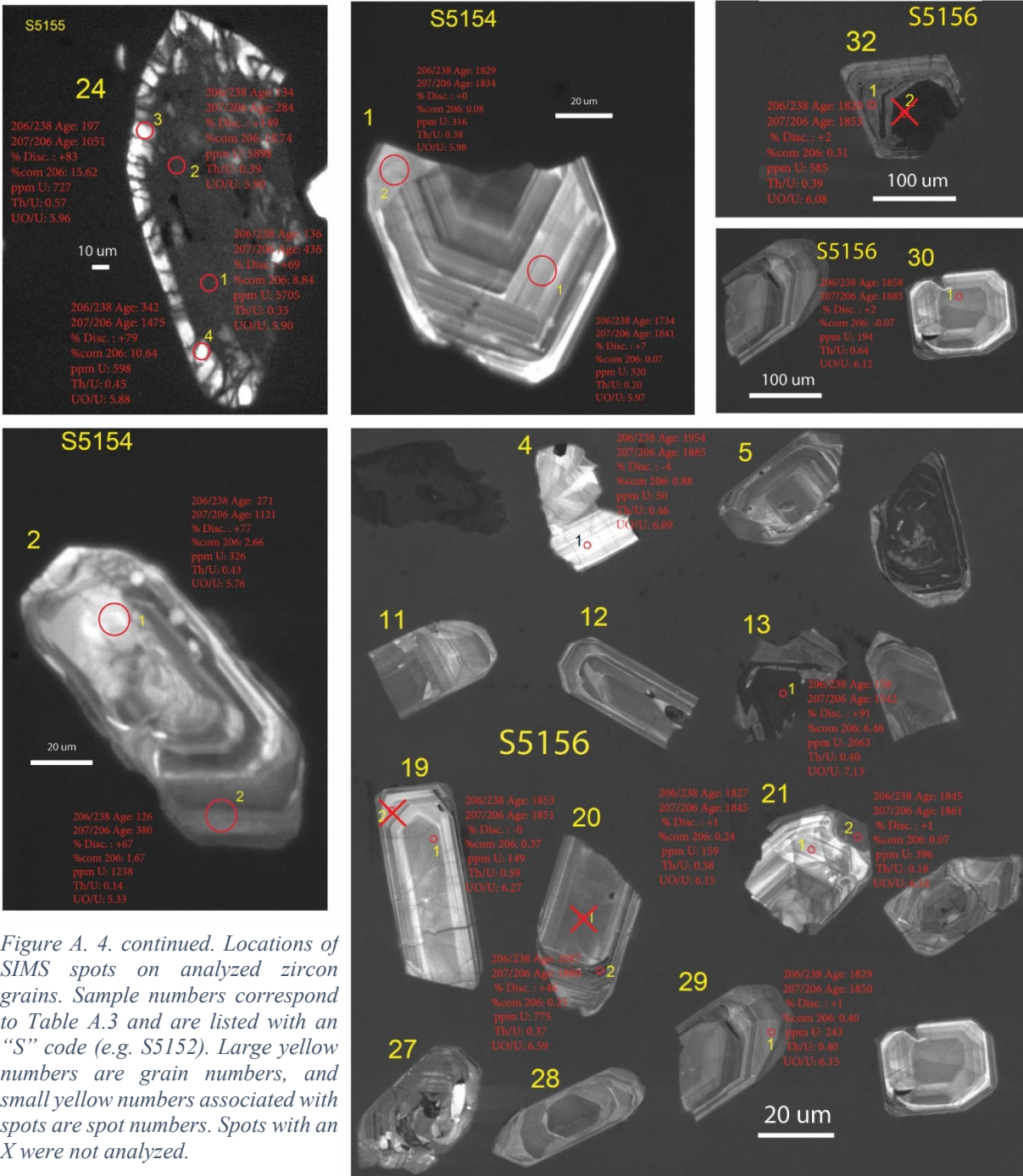| Sample (host rock)	Grain #	Spot #	Zircon type	Description
S5156 (granite)	4	1	1a	bright CL, thin igneous zoning, grain is a fragment of a once-larger grain
S5156 (granite)	19	1	1a	dull CL, homogeneous core of grain, lightly fractured, good igneous zoning
S5156 (granite)	21	1	1a	bright in CL, igneous zoning near core of grain
S5156 (granite)	30	1	1a	dull CL, near core of grain, fractured, broad igneous zoning
S5156 (granite)	29	1	1a	dull in CL, igneous zoning, characteristic zircon shape is broken in half
S5154 (melt)	1	1	1a	fine igneous zoning, moderately bright in CL
S5152 (melt)	1	1	1a	fine igneous zoning near centre of grain, dull to bright zones in CL
S5154 (melt)	1	2	1b	dull CL, fractured, no visible igneous zoning in the area with the spot
S5155 (melt)	18	3	1b	dull CL, no visible igneous zoning, minimal fractures
S5155 (melt)	18	2	1b	dull CL, no visible igneous zoning, minimal fractures
S5155 (melt)	18	4	1b	dull CL, no visible igneous zoning, minimal fractures
S5156 (granite)	21	2	1b	dark CL, embayment on edge of grain
S5152 (melt)	1	4	1b	smooth, dark in CL, regrowth, cross-cuts bright igneous zoning
S5152 (melt)	1	3	1b	smooth, dark in CL, no zoning, dark area cross-cuts bright igneous zoning
S5152 (melt)	1	2	1b	smooth, dark in CL, regrowth, cross-cuts bright igneous zoning
S5155 (melt)	18	1	2	fine igneous zoning, looks disturbed, dull in CL
S5156 (granite)	32	1	2	dull in CL, igneous zoning, grain has very dark core and is highly fractured
S5156 (granite)	20	2	2	very dark CL zones, fine igneous zoning
S5154 (melt)	2	2	2	dull CL, broad igneous zoning, near edge of grain
S5156 (granite)	13	1	2	very dark CL, near center of grain
S5152 (melt)	7	1	3	dull CL, fractured, no visible igneous zoning
S5152 (melt)	7	2	3	dull CL, fractured, no visible igneous zoning
S5152 (melt)	7	3	3	dull CL, fractured, no visible igneous zoning
S5155 (melt)	19	2	3	dull CL, smooth in SE image, no visible zoning
S5155 (melt)	11	1	3	fuzzy texture in BSE, dull CL
S5152 (melt)	5	2	3	dark in CL, near centre of grain, fractured, no igneous zoning
S5152 (melt)	5	1	3	dark in CL, near centre of grain, fractured, no igneous zoning
S5155 (melt)	24	1	3	dark CL, near center of grain, fractured, no visible igneous zoning
S5155 (melt)	24	2	3	dark CL, near center of grain, fractured, no visible igneous zoning
S5152 (melt)	7	4	4	bright CL, fractured, no visible igneous zoning, near center of grain
S5154 (melt)	2	1	4	bright CL, fractured, no visible igneous zoning, near center of grain
S5152 (melt)	5	3	4	bright in CL, top edge of grain, fractured, no igneous zoning
S5152 (melt)	5	4	4	moderately bright in CL, fractured, near edge of grain, no igneous zoning
S5155 (melt)	24	4	4	bright CL, right on edge of grain, fractured
S5155 (melt)	24	3	4	bright CL, right on edge of grain, fractured
S5155 (melt)[2]	*19*	*1*	*~5*	*dull CL, near edge of grain, fractured*

[2] Excluded from plots due to high common Pb

Sample # (host rock)	Grain #	Spot #	Zircon type	U (ppm)	Th (ppm)	Th/U	Yb (ppm)	Hf (ppm)	Zr$_2$O (counts·sec^{-1})	^{254}UO/ ^{238}U
S5156 (granite)	4	1	1a	50	23	0.46	120	8139	3285	6.09
S5156 (granite)	19	1	1a	149	88	0.59	261	8353	3420	6.27
S5156 (granite)	21	1	1a	159	60	0.38	138	8993	3941	6.15
S5156 (granite)	30	1	1a	194	124	0.64	316	9084	3816	6.12
S5156 (granite)	29	1	1a	243	96	0.40	175	11189	3895	6.15
S5154 (melt)	1	1	1a	320	63	0.20	105	10941	5373	5.97
S5152 (melt)	1	1	1a	330	106	0.32	182	11934	3758	6.24
S5154 (melt)	1	2	1b	316	119	0.38	175	9676	5475	5.98
S5155 (melt)	18	3	1b	365	18	0.05	92	12581	4643	6.22
S5155 (melt)	18	2	1b	365	19	0.05	84	11730	4544	6.09
S5155 (melt)	18	4	1b	382	22	0.06	95	12929	4001	6.17
S5156 (granite)	21	2	1b	396	70	0.18	111	13737	3788	6.14
S5152 (melt)	1	4	1b	896	93	0.10	182	12567	4164	6.31
S5152 (melt)	1	3	1b	1140	53	0.05	190	14377	3374	6.47
S5152 (melt)	1	2	1b	1251	68	0.05	186	15824	3552	6.37
S5155 (melt)	18	1	2	484	142	0.29	223	11674	3886	6.14
S5156 (granite)	32	1	2	585	230	0.39	314	10792	4014	6.08
S5156 (granite)	20	2	2	775	284	0.37	392	12392	3678	6.59
S5154 (melt)	2	2	2	1238	170	0.14	145	7126	7804	5.33
S5156 (granite)	13	1	2	2063	820	0.40	1729	14016	2594	7.13
S5152 (melt)	7	1	3	442	165	0.37	245	9801	4322	5.93
S5152 (melt)	7	2	3	444	161	0.36	260	9883	4412	5.82
S5152 (melt)	7	3	3	449	214	0.48	219	7771	6518	5.55
S5155 (melt)	19	2	3	465	90	0.19	192	13458	4104	6.05
S5155 (melt)	11	1	3	666	402	0.60	489	7852	6539	5.61
S5152 (melt)	5	2	3	1347	562	0.42	270	7110	5676	5.32
S5152 (melt)	5	1	3	1517	547	0.36	341	7119	5573	5.42
S5155 (melt)	24	1	3	5705	1999	0.35	1529	10209	3475	5.90
S5155 (melt)	24	2	3	5898	2303	0.39	1634	10338	3645	5.90
S5152 (melt)	7	4	4	201	79	0.39	176	6644	7130	5.52
S5154 (melt)	2	1	4	326	139	0.43	144	8475	6009	5.76
S5152 (melt)	5	3	4	211	43	0.21	127	15017	3387	6.33
S5152 (melt)	5	4	4	304	188	0.62	147	8740	5248	5.67
S5155 (melt)	24	4	4	598	270	0.45	274	11764	3757	5.88
S5155 (melt)	24	3	4	727	416	0.57	376	12046	4025	5.96
S5155 (melt)[2]	*19*	*1*	*~5*	*1913*	*483*	*0.25*	*576*	*10545*	*4410*	*5.72*

[2] Excluded from plots due to high common Pb

Sample # (host rock)	Grain #	Spot #	Zircon type	%comm. ^{206}Pb	^{204}Pb/ ^{206}Pb	^{207}Pb*/ ^{235}U	^{206}Pb*/ ^{238}U	^{207}Pb*/ ^{206}Pb*	^{206}Pb*/^{238}U Age (Ma)	Age abs. err.[1]	^{207}Pb*/^{206}Pb* Age (Ma)	Age abs. err. [1]	% Disc.
S5156 (granite)	4	1	1a	0.88	0.00051	5.632	0.3541	0.1153	1954	38	1885	60	-4
S5156 (granite)	19	1	1a	0.37	0.00021	5.195	0.3330	0.1132	1853	23	1851	28	-0
S5156 (granite)	21	1	1a	0.24	0.00014	5.096	0.3277	0.1128	1827	21	1845	24	+1
S5156 (granite)	30	1	1a	-0.07	-0.00004	5.313	0.3341	0.1153	1858	20	1885	19	+2
S5156 (granite)	29	1	1a	0.40	0.00023	5.115	0.3280	0.1131	1829	19	1850	21	+1
S5154 (melt)	1	1	1a	0.07	0.00004	4.788	0.3086	0.1125	1734	17	1841	21	+7
S5152 (melt)	1	1	1a	0.10	0.00006	5.302	0.3335	0.1153	1855	18	1884	15	+2
S5154 (melt)	1	2	1b	0.08	0.00005	5.071	0.3280	0.1121	1829	17	1834	14	+0
S5155 (melt)	18	3	1b	0.20	0.00011	5.343	0.3386	0.1144	1880	17	1871	14	-1
S5155 (melt)	18	2	1b	0.51	0.00029	5.455	0.3437	0.1151	1904	74	1882	17	-1
S5155 (melt)	18	4	1b	0.20	0.00011	4.600	0.2986	0.1117	1685	16	1827	16	+9
S5156 (granite)	21	2	1b	0.07	0.00004	5.201	0.3314	0.1138	1845	17	1861	14	+1
S5152 (melt)	1	4	1b	0.52	0.00029	4.442	0.2854	0.1129	1618	14	1847	13	+14
S5152 (melt)	1	3	1b	0.07	0.00004	4.860	0.3103	0.1136	1742	14	1858	8	+7
S5152 (melt)	1	2	1b	0.20	0.00011	3.540	0.2266	0.1133	1316	11	1854	10	+32
S5155 (melt)	18	1	2	1.48	0.00083	3.530	0.2246	0.1140	1306	13	1864	49	+33
S5156 (granite)	32	1	2	0.31	0.00018	5.096	0.3262	0.1133	1820	16	1853	14	+2
S5156 (granite)	20	2	2	0.25	0.00014	2.912	0.1837	0.1150	1087	10	1880	27	+46
S5154 (melt)	2	2	2	1.67	0.00094	0.147	0.0197	0.0542	126	1	380	122	+67
S5156 (granite)	13	1	2	6.46	0.00373	0.328	0.0249	0.0957	158	2	1542	96	+91
S5152 (melt)	7	1	3	2.59	0.00145	0.630	0.0509	0.0898	320	5	1421	94	+79
S5152 (melt)	7	2	3	2.70	0.00152	0.427	0.0376	0.0823	238	13	1252	141	+82
S5152 (melt)	7	3	3	1.59	0.00089	0.809	0.0621	0.0944	389	44	1516	58	+77
S5155 (melt)	19	2	3	2.20	0.00127	5.121	0.3207	0.1158	1793	40	1893	25	+6
S5155 (melt)	11	1	3	17.84	0.01001	2.369	0.1581	0.1087	946	18	1778	280	+50
S5152 (melt)	5	2	3	4.60	0.00258	0.150	0.0206	0.0527	132	2	315	312	+59
S5152 (melt)	5	1	3	6.89	0.00387	0.176	0.0202	0.0633	129	4	717	505	+83
S5155 (melt)	24	1	3	8.84	0.00510	0.164	0.0214	0.0556	136	3	436	412	+69
S5155 (melt)	24	2	3	18.74	0.01081	0.119	0.0210	0.0411	134	7	-284	1834	+149
S5152 (melt)	7	4	4	2.48	0.00139	0.794	0.0576	0.0999	361	19	1623	118	+80
S5154 (melt)	2	1	4	2.66	0.00149	0.455	0.0429	0.0770	271	19	1121	129	+77
S5152 (melt)	5	3	4	3.50	0.00196	0.653	0.0600	0.0789	376	6	1171	179	+70
S5152 (melt)	5	4	4	22.71	0.01275	0.222	0.0250	0.0645	159	23	758	1275	+80
S5155 (melt)	24	4	4	10.64	0.00614	0.694	0.0545	0.0924	342	7	1475	303	+79
S5155 (melt)	24	3	4	15.62	0.00901	0.318	0.0310	0.0744	197	4	1051	380	+83
S5155 (melt)[2]	*19*	*1*	*~5*	*41.31*	*0.02383*	*0.811*	*0.0405*	*0.1454*	*256*	*5*	*2292*	*373*	*+91*

*indicates a ^{204}Pb corrected value; [1] 1-sigma error; [2] Excluded from plots due to high common Pb

Table A. 4. Reference data from SIMS analysis

Name	Primary Standard ID	Ratio	Ratio Type	Value	2 sigma Error	95% confidence Error	Number of data (N)	MSWD	Probability of Fit (PoF)	Absolute or %	Min. Prob.
6266	Primary	^{204}Pb-corrected-^{207}Pb/^{206}Pb age	^{207}Pb/^{206}Pb age	556.8	19.7	24.9	15	1.40	0.14	Absolute	0.05
6266	Primary	^{254}UO/^{238}U	UO/U	6.25	0.01	0.05	15	17.25	0.00	Percentage	0.05
10493	Secondary	^{204}Pb-corrected-^{206}Pb/^{238}U age	^{206}Pb/^{238}U age	417.0	3.6	4.5	13	1.30	0.21	Absolute	0.05
10493	Secondary	^{207}Pb-corrected-^{206}Pb/^{238}U age	^{207}Pb corr. ^{206}Pb/^{238}U age	418.4	3.5	5.0	13	1.68	0.07	Absolute	0.05
10493	Secondary	^{204}Pb-corrected-^{207}Pb/^{206}Pb age	^{207}Pb/^{206}Pb age	366.9	100.8	98.8	13	0.97	0.48	Absolute	0.05
10493	Secondary	^{254}UO/^{238}U	UO/U	6.18	0.03	0.06	13	4.42	0.00	Percentage	0.05
11513	Secondary	^{204}Pb-corrected-^{207}Pb/^{206}Pb age	^{207}Pb/^{206}Pb age	3467.8	5.7	5.6	8	0.80	0.59	Absolute	0.05
11513	Secondary	^{254}UO/^{238}U	UO/U	6.18	0.04	0.06	8	2.07	0.04	Percentage	0.05
11513	Secondary	^{204}Pb-corrected-^{206}Pb/^{238}U age	^{206}Pb/^{238}U age	3406.1	23.5	45.5	8	2.69	0.01	Absolute	0.05